

A Review of Functionalising Diamond Surfaces for Thermionic Emission Applications

Raveena Kaur Bhogal



School of Chemistry

2024/25

University of Bristol, Cantock's Close, Bristol, BS8 1TS, United Kingdom

A thesis submitted in partial fulfilment of the requirements for the Honours Degree of MSci Chemistry at the University of Bristol.

Supervisor: Professor Paul W. May

Second Assessor: Professor Neil A. Fox

Physical and Theoretical Chemistry

Abstract

Diamond surfaces can be functionalised in order to manipulate their electronic properties. Negative electron affinity occurs due to electrons in the conduction band emitting from the surface and into vacuum. This process is enhanced because the barrier for emission has been removed and the vacuum level is below the conduction band minimum, resulting in thermionic emission. Functionalising the surface of diamond with small and highly charged metals such as scandium enhances the effectiveness of this.

The technique used for growth was microwave plasma chemical vapour deposition to produce high quality diamond thin film. Sample characterisation analysis was performed via laser Raman spectroscopy, scanning electron microscopy and x-ray photoelectron spectroscopy. Techniques for sample preparation included manual abrasion, Pt/Pd coating, acid wash and laser etching. For analysis of the electronic properties of the sample, thermionic testing as well as UV photoelectron spectroscopy were performed.

Laser Raman spectroscopy characterisation for nitrogen doped diamond observed peaks at 1332 cm^{-1} for diamond, 1595 cm^{-1} and 1365 cm^{-1} for sp^2 hybridisation and surface graphitisation, and 1480 cm^{-1} and 1145 cm^{-1} which were indicative of the *trans*-polyacetylene structures. Thermionic testing produced a maximum thermionic emission current for hydrogen terminated nitrogen doped diamond at $8.35 \times 10^{-7}\text{ mA}$.

This report aimed to assess the thermionic emission, negative electron affinity and work function of an optimised scandium oxide functionalised nitrogen doped diamond surface grown on a molybdenum substrate. X-ray photon spectroscopy peaks characterised the surface with peaks at 285.68 eV for sp^3 hybridized carbon, a downshifted binding energy of 530.9 eV for oxygen, alongside spectrum peaks at binding energies of 401.876 and 406.176 eV from the scandium $2p^{3/2}$ and $2p^{1/2}$ electrons, respectively. This worked together to characterise the scandium-oxygen termination. Ultraviolet photoelectron spectroscopy results showed a negative electron affinity value of -1.545 eV and a work function calculated as 3.6 eV . The thermionic emission data were limited as a result of unoptimized grating patterns for the plasmonic heating effect. However, unstable maximum emission current peaks were exhibited at 3.06×10^{-7} and $6.00 \times 10^{-7}\text{ mA}$.

Acknowledgements

I would like to express my gratitude to Dr. Ramiz Zulkharnay for his counsel and encouragement throughout the duration of my project. His guidance and feedback were essential for shaping the progression and direction through my research, assisting me by pointing me in the right direction and pushing me to overcome set-backs.

I also would like to thank my supervisor, Professor Paul W. May for the helpful advice and feedback. Particularly throughout my report writing and presentation process. The supportive advice that Professor May provided allowed me to build my confidence and develop valuable skills.

I am grateful to the entirety of the Bristol University Diamond Group (BUDGies) for the warm, comfortable and welcoming environment that I experienced over the course of my project. Namely, Professor Neil A. Fox, Dr James Smith, Mr Liam Cullingford, Mr James Pittard, Ms Mengai (Kisty) Mao and Ms Catherine Monk. Not only did they provide valuable advice and encouragement but also a positive community and work environment alongside the other Master's and Bachelor's students.

I would like to thank my Mum and Dad for supporting me throughout my degree and listening to all my fears and hopes for the future and my sister and brothers for always making me laugh. Finally, I would like to thank my Uncle, Sarbjit Singh for being an inspiration to work hard and be kind.

Author's Declaration

I declare that this dissertation was carried out in accordance with the requirements of the University of Bristol's Regulations and Code of Practice for Research Degree Programmes and that it has not been submitted for any other academic award. Except where indicated by specific reference in text, the work is the candidate's own work. Work done in collaboration with, or with the assistance of others, is indicated as such. Any views expressed in the dissertation are those of the author.

SIGNED:  DATE: 07/04/25

Symbols and Acronyms

Symbols

E_A	Activation Energy
Φ	Work Function
δ	Partial Charge
K	Kelvin
eV	Electron Volts
V	Volts
χ	Electron Affinity
E_{vac}	Vacuum Level
E_{CBM}	Conduction Band Minimum
$h\nu$	UV Excitation Energy
E_{VMB}	Valence Band Minimum
E_F	Fermi Level
J	Emission Current Density
A_R	Richardson Constant
k	Boltzmann Constant
T	Absolute Temperature
T_{hot}	Emitter
T_{cold}	Collector
η_{carnot}	Carnot Efficiency
E_G	Band Gap
E_V	Valence Band Maximum
C_d	Carbon Atom on a Diamond Surface
M	Metal
$^{\circ}C$	Degrees Celsius
\AA	Angstroms
sccm	Standard Cubic Centimetres per Minute
λ	Wavelength
ρ	Density

Acronyms

CVD	Chemical Vapour Deposition
SCD.....	Single Crystal Diamond
PDC	Polycrystalline Diamond
NDD.....	Nitrogen Doped Diamond
NEA.....	Negative Electron Affinity
PEA.....	Positive Electron Affinity
SEM	Scanning Electron Microscopy
CBM.....	Conduction Band Minimum
VBM.....	Valence Band Minimum
EN.....	Electronegativity
NCD.....	Nanocrystalline Diamond
MWCVD.....	Microwave-plasma Chemical Vapour Deposition
ASTEX.....	Applied Science and Technology Microwave Reactor
NIRIM.....	National Institute for Research in Inorganic Material Microwave Reactor
HFCVD.....	Hot Filament Chemical Vapour Deposition
SEM.....	Scanning Electron Microscopy
MW.....	Microwave Power
BEN.....	Bias-enhanced Nucleation
NCD.....	Nanocrystalline Diamond
SD.....	Seed Density
IR.....	Infrared
BG.....	Band Gap
CB.....	Conduction Band
VB.....	Valence Band
TEC.....	Thermionic Energy Converter
UHV.....	Ultra-high Vacuum
DFT.....	Density Functional Theory
ML.....	Monolayer

NV.....Nitrogen Vacancy
UPS.....Ultraviolet Photoelectron Spectroscopy
SPP.....Surface Plasmon Polaritons
TECsim.....Thermionic Energy Converter Simulator
PID.....Proportional Integral Derivative
KE.....Kinetic Energy
BE.....Binding Energy
RT.....Room Temperature
HNDD.....High Nitrogen Doped Diamond
LNDD.....Low Nitrogen Doped Diamond
MCD.....Microcrystalline Diamond
XPS.....X-ray Photon Spectroscopy
PV.....Photovoltaic
FEE.....Field Electron Emission
SDD.....Sulfur Doped Diamond

Contents

Abstract.....	2
Acknowledgements.....	3
Author's Declaration.....	4
Symbols and Acronyms.....	5
Contents.....	8
1 Introduction.....	10
1.1 Structure and Properties of Diamond.....	10
1.2 Surface Diamond.....	11
1.3 Chemical Vapour Deposition of Diamond.....	14
1.31 MWCVD.....	16
1.32 Nucleation.....	17
1.33 Nucleation via Seeding.....	17
1.34 Nucleation via Abrasion.....	18
1.35 CVD Surface Chemistry.....	18
1.4 Negative Electron Affinity.....	20
1.5 Problems and Solutions for CVD Surface Chemistry.....	22
1.51 The Effect of Grain Boundaries on the Electronic Performance of Diamond Thin Films.....	22
1.52 Thermionic Emission.....	23
1.53 Lowering the Work Function.....	25
1.6 Surface Terminations.....	27
1.61 Hydrogen Terminations.....	28
1.62 Metal-oxygen Terminations.....	29
1.63 Group I and II Oxygen Terminations.....	30
1.64 Aluminium Oxygen Termination.....	31
1.65 Transition Metal Terminations.....	31
1.66 Metal Terminations.....	32
1.67 Positive Electron Affinity Surface Terminations.....	32
1.7 The Thermal Expansion Coefficient.....	32
1.8 Thermionic Emissions from NDD vs PDD and Molybdenum as a Substrate and Electrode.....	33
1.9 Project Aims.....	34
2 Methods.....	36
2.1 Sample Preparation.....	36
2.2 Pt/Pd Coating.....	37
2.21 Scanning Electron Microscopy (SEM).....	37
2.22 Acid Wash.....	38
2.3 Laser Raman Spectroscopy.....	39
2.4 Hydrogen Termination.....	39

2.5	Laser Etching.....	40
2.6	Thermionic Testing	42
2.7	Oxygen Termination.....	43
2.8	NanoESCA.....	44
2.81	Preparation Chamber.....	45
2.82	X-ray Photoelectron Spectroscopy (XPS).....	45
2.83	Deposition Chamber.....	45
2.84	UV Photoelectron Spectroscopy (UPS).....	46
3	Results and Discussion.....	47
3.1	Characterisation of Seeded Molybdenum	47
3.2	Scanning Electron Microscopy (SEM).....	48
3.22	Raman Spectroscopy Characterisation.....	51
3.3	Thermionic Emission Data of a Hydrogen Terminated Surface	53
3.31	Thermionic Emission Data from a ScO-terminated Surface.....	54
3.4	X-ray Photon Spectroscopy (XPS) Characterisation	56
3.5	Ultraviolet Photoelectron Spectroscopy (UPS) Characterisation	59
3.6	Failures and Scientific Limitations.....	62
3.61	Incompatible Grating of Molybdenum	62
3.62	Delamination of Diamond Thin Film	64
4	Conclusion	66
5	Future Work	67
5.1	Optimizing Grating Patterns for the Plasmonic Heating Effect	67
5.2	Co-doping	68
6	Appendix	72
7	References	75

1.1 Structure and Properties of Diamond

Diamond is commonly considered as the hardest material known to man.¹ This consideration arises as structurally diamond is formed by a crystal lattice that possesses an sp^3 hybridised structure and an exact hardness of 10^4 kg/mm, see figure 1.² ^{12}C and ^{13}C are the two more stable isotopes of carbon that are found in a natural abundance of 98.9% and 1.1% and with nuclear spin states of 0 and $\frac{1}{2}$, respectively.³ Other prominent properties of diamond that allow it to be chemically inert, tough, resistant to the effects of temperature and pressure, highly thermally conductive and electrically adaptable are detailed in table 1 of the appendix.⁴ Consequently, it is no wonder that for generations, diamond has been under constant scrutiny by the scientific community for its expansive range of potential applications, particularly the interest surrounding electro-chemical technology.

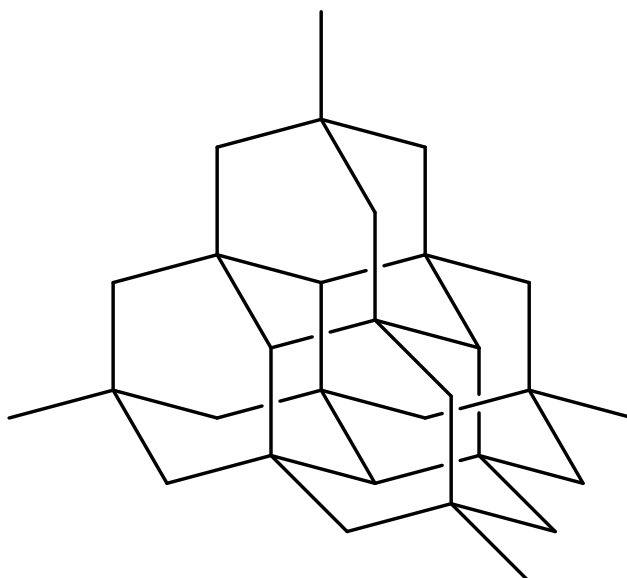


Figure 1 Structure of diamond.

Geometrically, there are 4 strong covalent bonds that make up the sp^3 hybridisation of diamond in its face-centred cubic Bravais lattice arrangement. Each carbon atom contributes a $1s^2 2s^2 sp^2$ electronic configuration to the tetrahedral lattice, making diamond chemically stable.¹ The 4 carbon-to-carbon bonds have an experimentally calculated length of 1.54 \AA and that lattice constant is 3.57 \AA , see figure 2 representing the unit cell of diamond, made up of 8 carbon atoms.⁵ As a result of this bonding, diamond has a very high thermal conductivity value of $2000 \text{ W m}^{-1} \text{ K}^{-1}$ at 300 K. This is comparable to silicon (Si) which also has the ability to form a giant crystal lattice through covalent

bonding in a cubic faced structure. However, its thermal conductivity at room temperature is 15 times lower than that of diamond.⁶

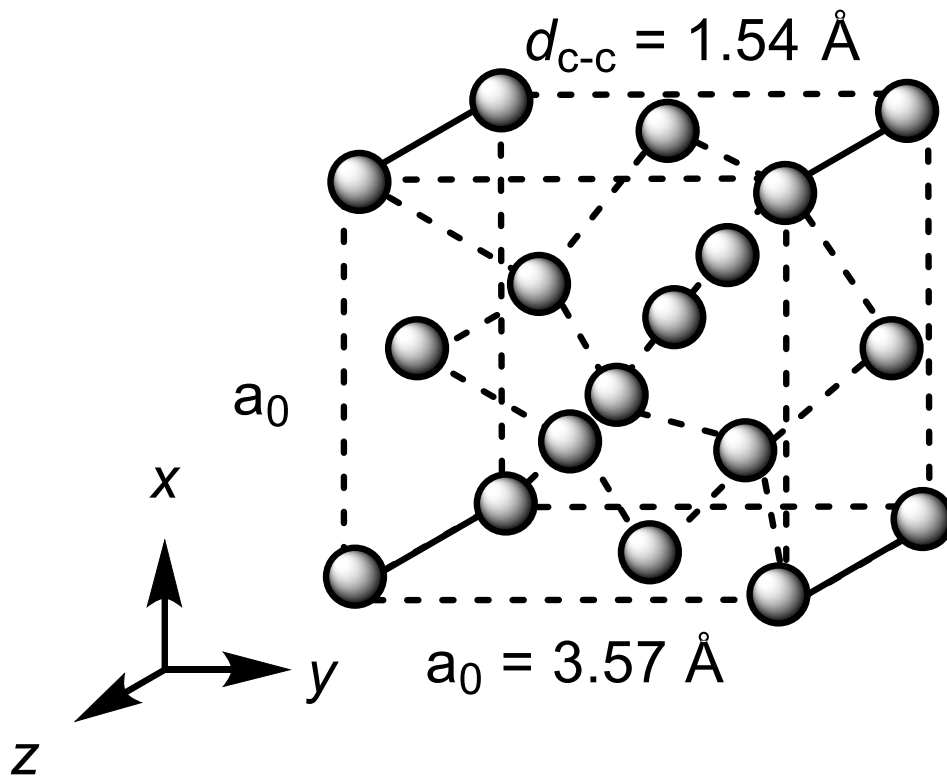


Figure 2 Unit cell structure of diamond.

Consequently, this bonding arrangement results in diamond having a high mass and atomic density of 3516 kg/m^3 and $1.76 \times 10^{23} \text{ cm}^{-3}$, respectively. The dense medium allows for the movement of phonons that are transmitters of heat energy through the lattice, leading to its high thermal conductivity.⁷

1.2 Surface Diamond

As depicted in figure 2, the cubic crystal faces are often presented by an x, y, z coordinate system. This represents single crystal diamond (SCD) morphology that is dependent on gas phase adsorption. The three most common adsorption coordinated systems are depicted in table 2 of the appendix.⁸ The morphology of these single crystal surfaces can be calculated by the α -parameter which is defined by equation [1]:

$$\alpha = \sqrt{3} \left(\frac{V_{100}}{V_{111}} \right) \quad [1]$$

where v_{100} and v_{111} are parameters that define the velocity of growth in the (100) and (111) direction. For the purpose of this report, nanocrystalline diamond (NCD) is the focus; however, polycrystalline diamond (PCD) and SCD films must also be considered. For SCD, if its α -parameter correlates to a square (100) surface, this results in a smooth textured surface. The α parameter links to the thermal expansion coefficient of the diamond lattice as it represents the linear expansion as a function of temperature. As temperature increases, kinetic energy increases which in turn leads to an increase in vibrations. The vibrations of diamond are anharmonic which results in a monotonic increase in the a_0 length and can be parametrised via equation 2, when temperature is at 500 K.³

$$\alpha = 1.08 \times 10^{-11} T^2 \quad [2]$$

For a SCD (100) lattice, due to the sp^3 hybridization, there are 'dangling bonds' that give rise to a high energy surface. As diamond is metastable, its surface must be stabilized by termination in order to prevent cross-linkages which result in the formation of graphite, and this process can dissipate energy through the formation of mutual bonds.⁷ Each carbon atom contributes two dangling bonds to the surface composition; therefore, a (2×1) reconstruction is necessary, see table 4 in the appendix, detailing the different surface states of diamond and their corresponding reconstructions. For example, a termination by hydrogen would result in a C(100)-(2×1):H structure forming, as depicted in figure 3.

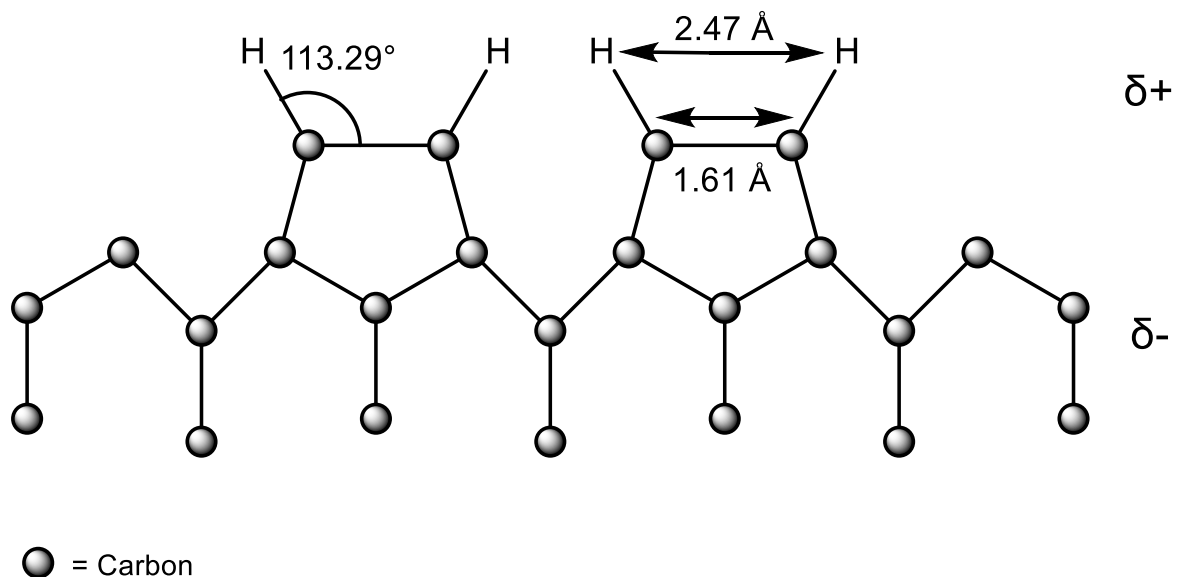


Figure 3 Surface structure of H-terminated diamond, including its parameters.

As depicted in figure 3, this asymmetric distribution of atoms and electrons on the surface has the potential to produce a surface dipole, which is an important consideration for

technological applications surrounding this field of study. This dipole is facing inwards into the surface and has the ability to lower the surface barrier potential and in turn the work function (ϕ) and activation energy (E_A). In bulk diamond, the partially negative charge generated by the electrons is attracted by the partially positive charges of the hydrogens attached to its surface.⁹ Diamond crystal structure has a space group of O_h ⁷ and this has 48 symmetry operations associated with it, where the two most significant surfaces are (100) and (111) diamond. The surface dipole induces a difference in electrostatic potential which has particular impacts on these surfaces. However, the (100) surface is often considered more valuable as opposed to the (111) surface as its homoepitaxial growth is less vulnerable to stacking faults and distortion, see figure 4.¹⁰

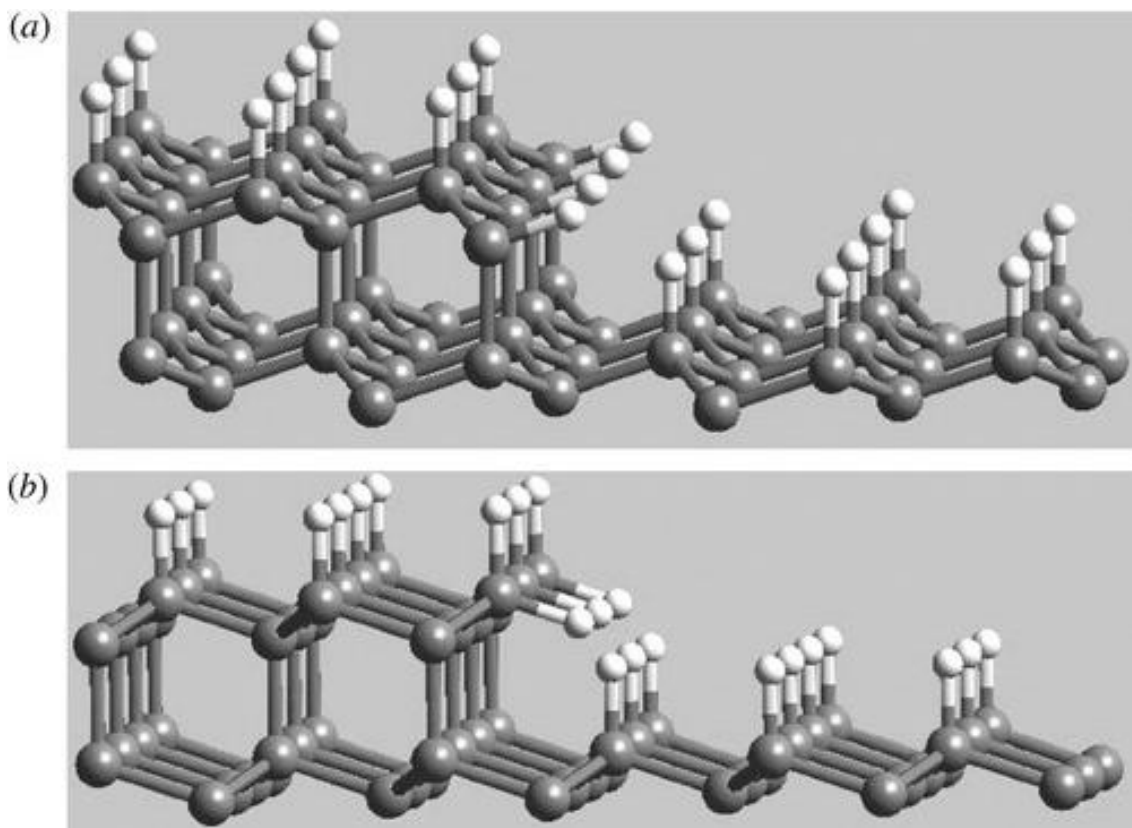


Figure 4 A ball-and-stick model of H-terminated diamond (111) surfaces with (a) step-edged growth of diamond (110) surfaces, requiring the addition of two atoms and (b) a step-edged growth of diamond (100) surfaces, requiring the addition of one atom.¹¹

1.3 Chemical Vapour Deposition of Diamond

Although naturally, diamond is an insulating material, with a wide bandgap of 5.47 eV, via doping, its electronic properties can be manipulated. Therefore, a semi- or superconducting material can be produced via the synthetic procedure, chemical vapour deposition (CVD).¹¹ CVD involves the deposition of diamond to form a thin film surface via a chemical reaction pathway. Originally, the CVD process is thought to have been first proposed by J.M Blocher in Houston in 1960 for the Electrochemical Society.¹² Blocher detailed the requirement for gaseous precursors on a heated surface, which for the purpose of his review included silicon, tungsten and pyrolytic carbon. At this point in time, despite the knowledge that CVD had the potential of producing a wide range of crystal structures in needle-like, epitaxial crystal films, there was little understanding as to its applications.¹³

However, as comprehension and time went on, use of CVD for applications in the medicinal and technological field expanded significantly. For example, in 2014, due to the biocompatible and stable properties of diamond, it was discovered that this synthetic process could be used to produce biomolecular products with hydrophilic properties that had the ability to form covalent bonds *in vivo*.¹⁴ More recently, the reality of utilising CVD diamond in electrochemistry for water splitting applications, as well as for quantum sensors via shallow nitrogen vacancy (NV) centres for the detection of electric and magnetic fields, has become apparent.¹⁵

The simplified overview of steps for CVD begins with the activation of a mixture of gaseous precursor which is passed through a hot filament (or plasma). This provides energy to the molecules and causes them to fragment into reactive species such as radicals, atoms, ions and electrons. Upon activation, the free radical mixture generates thermal energy up to 1000 K. Beyond the diffusion layer, processes such as adsorption, desorption and diffusion at the substrate surface occur in a cycling flow state. Diamond will grow in optimised conditions as a result of these chemical reactions and this is depicted in figure 5, where the gas inlet allows for the gaseous precursor to enter the system. A typical precursor gas is made up of a mixture of methane (CH₄) which has been diluted in an excess of hydrogen (H₂).⁸ The radical species are produced via the hydrogen abstraction of CH₄ to produce CH₃, CH₂ and CH, which in turn perform hydrogen abstraction reactions in a cyclic reaction flow to form C₂- species such as C₂H₅, C₂H₆, etc.¹⁶

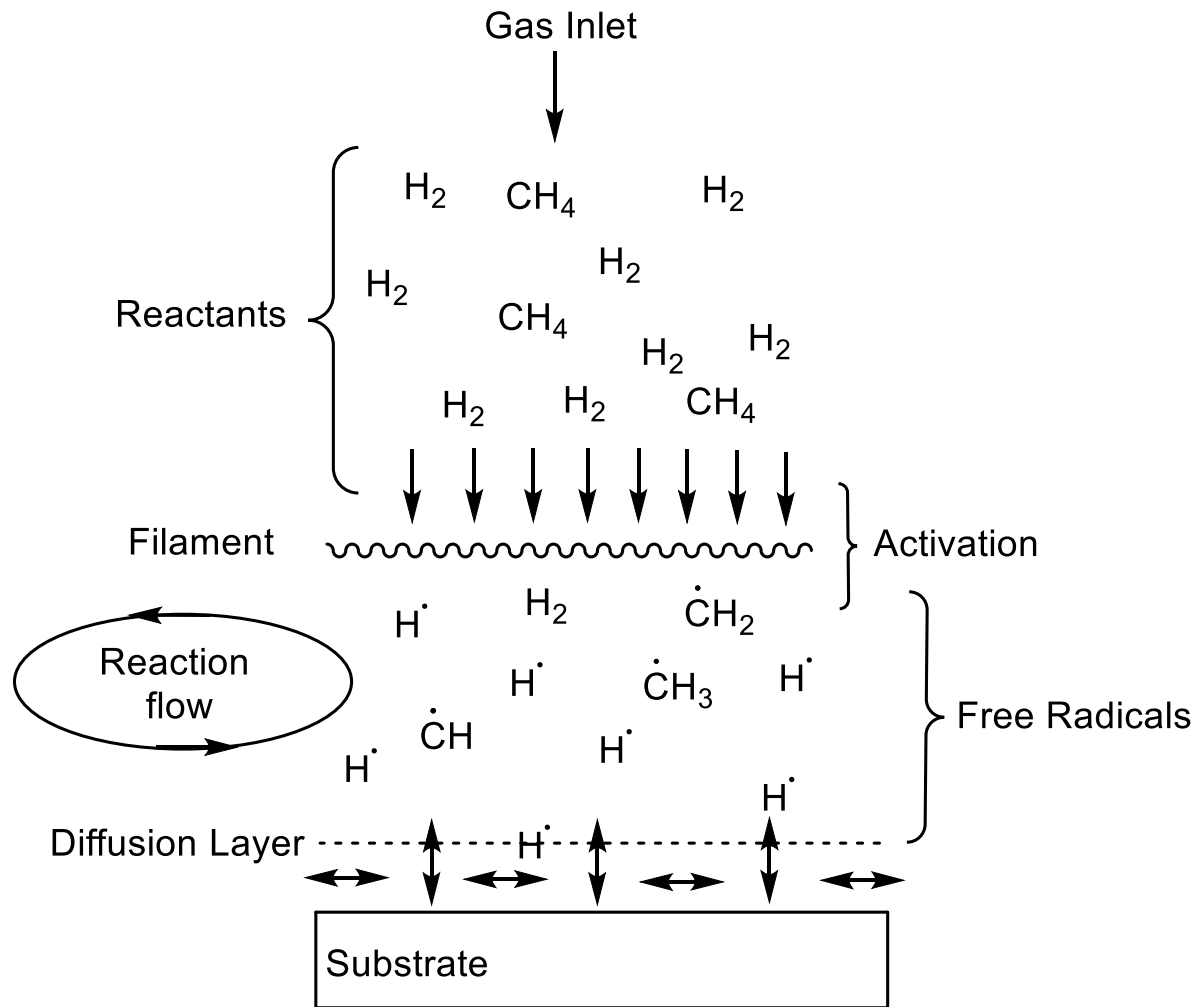


Figure 5 A diagram representing the chemical and physical processes involved in the hot filament CVD of diamond.⁸

There are different methods by which CVD can occur. This can be via hot filament CVD (HFCVD) in figure 5, to produce PCD thin films of medium quality. This method has a relatively low operating cost and a straightforward operating procedure. Other methods include 'ASTEX-type' and 'NIRIM-type' microwave plasma reactors (MWCVD) and DC arc jet plasma torches. DC arc jet torches are advantageous as they have a high growth rate, yet this is counteracted by impurity contamination leading to low quality diamond formation. For the purpose of this report, the focus is on MWCVD reactors as it is the most effective method for producing refined diamond thin films.¹⁶

Prominent characterisation techniques for CVD diamond growth include scanning electron microscopy (SEM) and Raman spectroscopy. SEM provides insight into the morphology of a diamond surface and its grain size. Raman spectroscopy is useful in

understanding the hybridisation of a surface. It has the ability to differentiate between a clean diamond surface and growth of a surface that has resulted in graphitisation.¹⁷

1.31 MWCVD

In MWCVD, once the precursor gas mixture is introduced into the chamber, microwave power (MW) is generated and administered through a dielectric window into the system. A plasma is formed above the sample, as seen in figure 6. Inside the plasma, an electromagnetic field is present which accelerates electrons, causing them to collide with the gas molecules. This results in an energy transfer and the formation of activated free radical species. The 'ASTEX' system is preferred due to its high growth rate of high quality diamond thin films, although its main limitation is its high cost.¹⁶



Figure 6 The front MWCVD reactor growing nitrogen doped diamond (NND) on a molybdenum substrate at the University of Bristol Diamond Laboratory.

1.32 Nucleation

CVD diamond growth works homoepitaxially, this means that at high pressure and temperature, crystal growth follows the same orientation of a tetrahedral template already present at the surface.³ Therefore, the formation of a diamond lattice occurs as a result of carbon atoms nucleating to a surface and building upon the initial tetrahedral structure. Important considerations for homoepitaxial growth include: stability, carbon-substrate binding, carbide formation, crystal lattice geometry and quality. Non-diamond lattice formations perform heteroepitaxial growth as there is no carbon prototype to build upon. Etching occurs and the carbon deposits on a substrate surface cycle back into the gas phase and react with hydrogen free radicals in the chamber, see figure 5.⁸

For MWCVD, ion bombardment nucleation (or bias-enhanced nucleation, BEN) is the preferred technique when growing SCD. A threshold voltage is applied to the smooth-surfaced sample in the chamber. Once this voltage has been applied, a mixture of hydrogen in methane is applied where the concentration is varied between 1 to 40% of the methane concentration depending on the level of doping that is required. For example, for a nucleation density of $1 \times 10^{10} \text{ cm}^{-2}$, 5% of methane, as well as a threshold voltage of -70 V would be the optimal conditions for this growth.³ There are two standard methods to encourage nucleation of diamond onto non-diamond substrates and these are through abrasion or seeding.

1.33 Nucleation via Seeding

Seeding involves the attachment of diamond particles on a substrate surface. This can be done electrostatically in order to achieve nanocrystalline diamond (NCD) thin films. Nanodiamond is coated onto a substrate surface prior to diamond growth under MWCVD conditions which instigates diamond crystal lattice formation. Substrates can be coated through being immersed in a seeding solution, electrospray ionisation, as well as spin coating. The seed density (SD) can be calculated via equation [3]:

$$SD = \frac{2}{\sqrt{3}d^2} \quad [3]$$

, where d is the diameter of a sphere in nanometres (nm). Assumptions are made that each seed is a perfect sphere and of the same size and a perfect monolayer (ML) is formed. By joining the centre of each sphere, a hexagon forms which gives rise to equation [3], see figure 7. Theoretical seed diameter is of the range of 1-10 nm.¹⁸

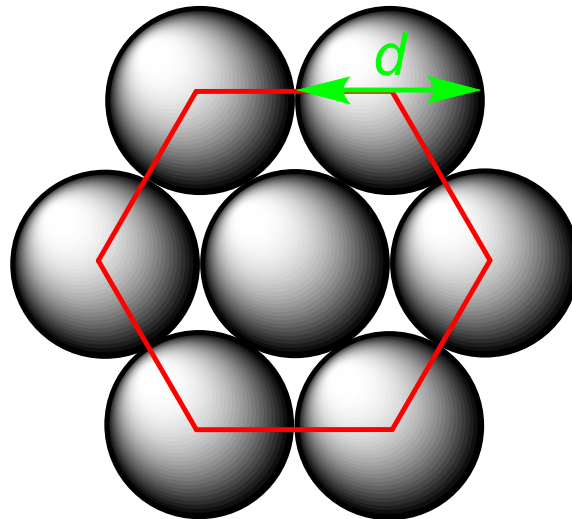


Figure 7 A visual reference for calculating the theoretical seed diameter in the area of a hexagon where d is the diameter of a sphere in nm.¹⁸

1.34 Nucleation via Abrasion

Treatment of substrate material with abrasive powder (nanodiamond) scratches the surface and manipulates its topography in order to leave behind powdered residue. The topography changes from being relatively smooth to having sharp nanostructures that are ideal structures for nucleation onto a surface. These protrusions lead to the presence of a greater number of 'dangling bonds' that act as a site with increased surface area for homoepitaxial growth.¹⁹

1.35 CVD Surface Chemistry

The process of CVD to form diamond thin films must allow for termination in a specific way in order to prevent cross-linking and surface graphitization. This is an important consideration as the formation of a graphitic crystal lattice, which is sp^2 hybridised and has a lower total energy, is favoured, as opposed to a metastable, homoepitaxial diamond surface which is sp^3 hybridised.¹⁷ The most common forms of surface termination to prevent graphitisation include hydrogen (H-), Oxygen (O-), Hydroxyl (HO-) and Amino (H₂N-) terminations, see figure 8 for a comparison of a clean surface with H- and O-terminated surfaces.²⁰

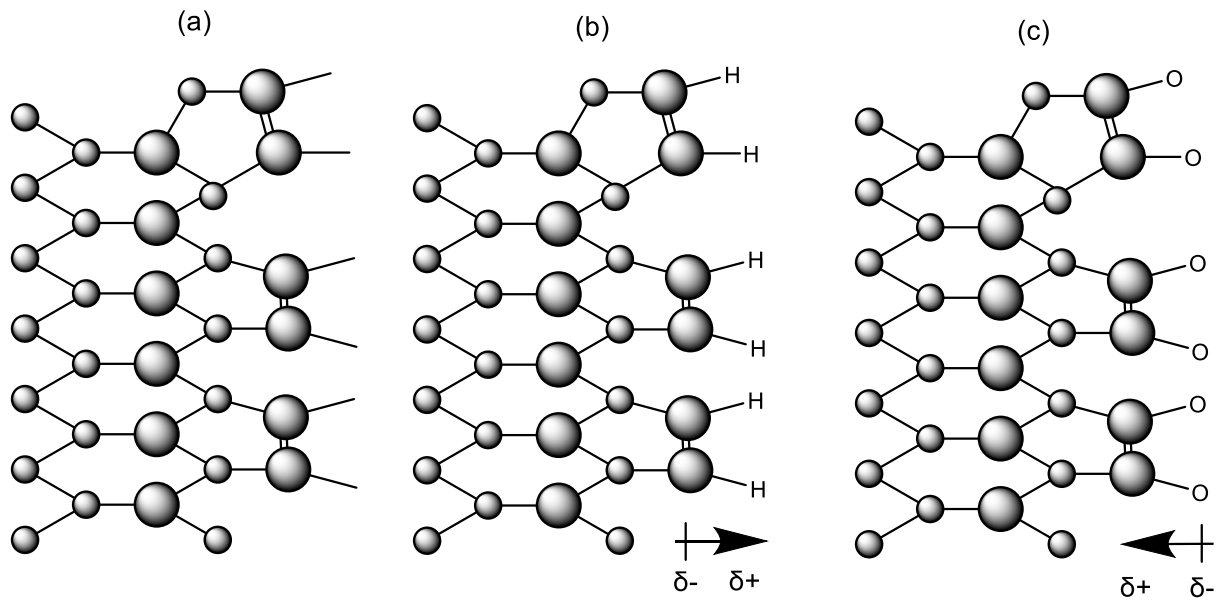


Figure 8 Comparing (a) a clean diamond surface, (b) a H-terminated diamond surface and its respective dipole orientation and (c) an O-terminated diamond surface and its respective dipole orientation.

For a molecule to bind to the surface electrostatically, which is indicated in figure 8 by the formation of partial charges resulting in dipoles, the adhesion energy is taken into account. The surface adhesion energy can be calculated by the equation 4:

$$\Delta E_{\text{adhesion}} = E_{\text{surface+adlayer}} - E_{\text{surface}} - E_{\text{adlayer}} \quad [4]$$

, which provides information about the type of bonding at the surface of diamond as a result of total energy of adhesion ($\Delta E_{\text{adhesion}}$) at the interface. This allows for the differentiation between C(100)-(2×1):H and C(100)-(2×1):O termination of diamond (100) surfaces. Hydrogen attaches to the surface via chemisorption, which can be characterised by infrared (IR) stretching frequencies to distinguish between different diamond surfaces following H-termination.²¹ H-terminated surfaces are favoured due to their ability to manipulate the insulating properties of diamond, as a result of negative electron affinity (NEA).

1.4 Negative Electron Affinity

Negative electron affinity is desirable as surfaces that possess it become semiconducting. This is because the vacuum level is found below the conduction band minimum (CBM), see (b) of figure 9.²² Semiconducting properties are induced as the barrier for electrons found in the conduction band (CB) to be emitted from its surface and into vacuum, is removed and so the process occurs readily. Diamond has a wide band gap (BG) of 5.47 eV which alludes to its insulating properties as the vacuum level lies above the CBM and so electrons are unable to overcome the barrier of energy and escape from the surface of the conduction band into vacuum. This can be represented by the PEA energy level diagram depicted in (a) of figure 9.

In reference to figure 9, H-terminated NEA surfaces exhibit p-type surface conductivity.²³ This generates high electron emissivity properties of homoepitaxially grown diamond thin films and is becoming increasingly desirable for investigation.²⁴ The NEA surface demonstrates downward band bending at the interface. This is a theoretical representation of the energy offset as a result of charge disparity at the surface and does not occur physically. As the material is p-type, its Fermi level is found lying closer to the VBM whilst the valence and conduction band experience a disparity of charge and band bending. This is often described as the 'true NEA' as despite band bending, the CBM is still found to be above the vacuum level (E_{vac}). On the other hand, an 'effective NEA' may occur if the charge disparity causes the CBM push below the vacuum level.⁹

Theoretically, the CB electrons possess enough energy for electron emissivity into the vacuum. However, at the interface this requires tunnelling through the barrier or results in entrapment by a surface energy barrier resulting in thermalisation at the CBM. For the purpose of this report, a p-type surface is desirable due to its large NEA potential meaning that the barrier for electron emission into vacuum is lower than for an n-type surface, despite having a large BG barrier to overcome. A p-type surface has some advantages due to its low work function; however, the charge imbalance of its surface creates upwards band bending. This has the potential to act as a barrier for electron emission which is not favourable for electronic applications.⁹

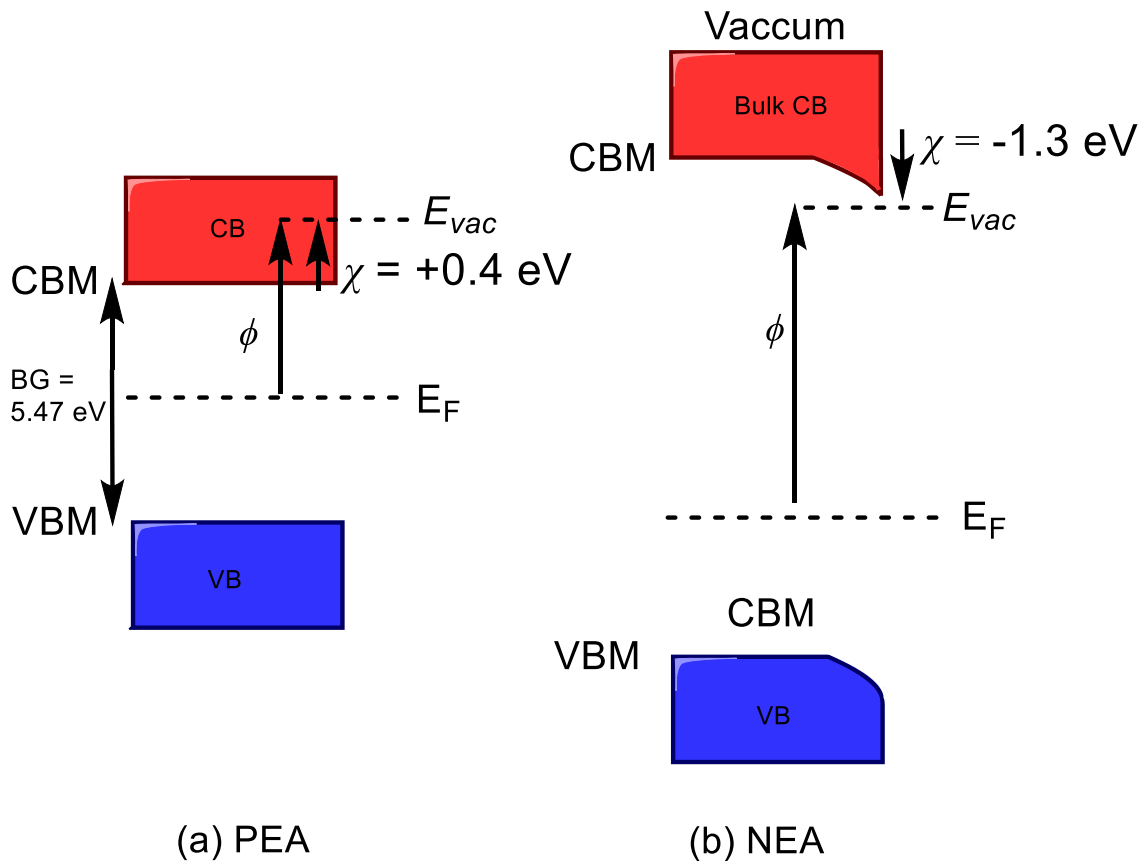


Figure 9 (a) a PEA energy level diagram of a clean surface and (b) a NEA diagram relative to a H-terminated, p-type diamond surface.

Subsequently, hydrogen-terminated surfaces possess a NEA due to the surface dipole that is created as carbon is more electronegative in comparison to hydrogen, see figure 8. This electrostatic dipole that is created results has a NEA of -1.3 eV, as stated in literature. This can be compared to (c) of figure 7 that represents an oxygenated surface resulting in a PEA of +1.7 eV.¹⁰

In the technological field so far, metal-semiconductor field effect transistors have been developed that utilise the chemistry of NEA surfaces. This advancement has been useful in enhancing MW power technology through its high power output density.²³ This functions as a cold cathode which has a high frequency and power output. For a cold cathode system, the addition of the vacuum layer ensures electron movement is unaffected by phonon scattering resulting in a linear motion that maximises energy transfer in the system.²⁵ Consequently, device efficiency can be maximised by the development of technology that utilises NEA.

1.5 Problems and Solutions for CVD Surface Chemistry

Despite having a wide scope of potential for useful applications, there are factors that have to be considered and overcome in order to maximise the functions of CVD surface chemistry, surface functionalisation and NEA.

1.51 The Effect of Grain Boundaries on the Electronic Performance of Diamond Thin Films

Grain boundaries found in inhomogeneously grown diamond thin films are planar defects, see figure 10. They have the potential to impact phonon movement between interfaces which, in turn, affects its thermal conductivity. Grain boundaries can be found in PCD. Consequently, PCD will have a lower than expected thermal conductivity, $<3000 \text{ W m}^{-1} \text{ K}^{-1}$.²⁶ Electrical conduction will also be affected by the presence of grain boundaries, as they will cause scattering of electrons. Therefore, most work involving studying current flow through diamond surfaces use SCD samples as they do not have grain boundaries.

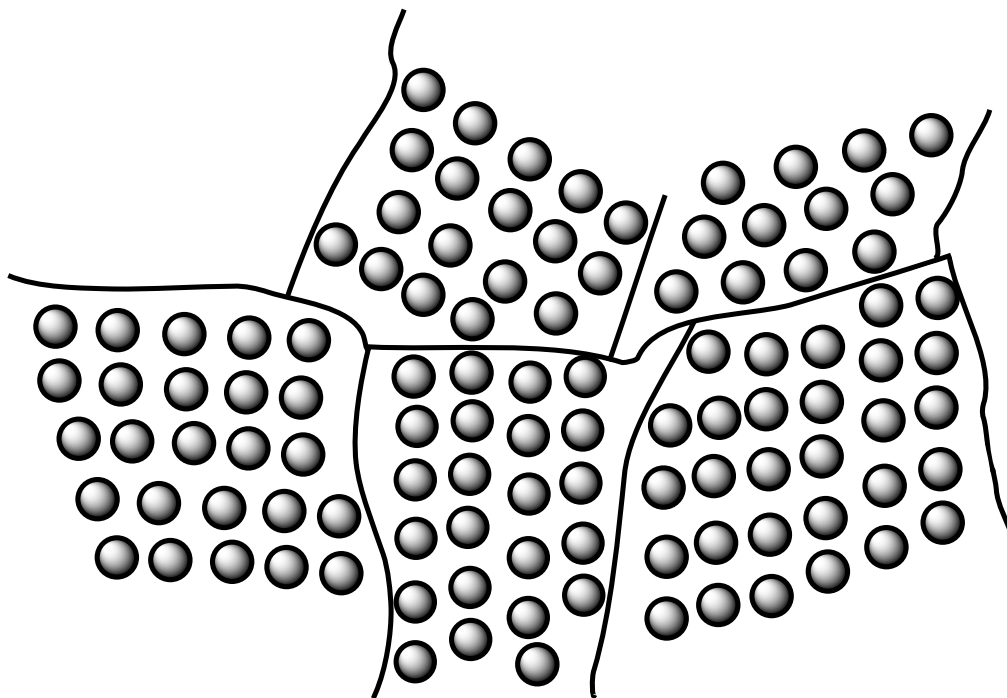


Figure 10 The uneven growth of atoms in a grain boundary of a crystalline solid with grain sizes ranging from $1 \mu\text{m}$ to 1mm .⁸

1.52 Thermionic Emission

Functionalised diamond surfaces possessing NEA are desirable as they can be paired with thermionic chemistry which has the potential for energy applications, for example, the thermionic energy converter (TEC).⁹ Thermionic chemistry involves electrons having the ability to emit from a surface at high temperatures. In 1930, a report was published by Dushman who proposed the Richardson-Dushman equation:

$$J(T) = A_R T^2 \exp\left(-\frac{\Phi}{kT}\right) \quad [5]$$

, where the emission current density J is dependent on T , the absolute temperature of the material that is emitting electrons. A_R is the Richardson constant and is a universal constant defined by equation [6], ϕ is the work function and k is the Boltzmann constant.²⁷ When taking into account the practical use of equation [5] for the application of energy converters, surfaces such as diamond that possess NEA are advantageous.²⁸ Diamond, with its low ϕ due to NEA, can lower the operating temperature required to achieve high electron current density. The emission characteristics can be manipulated via doping and they can withstand substantial flows of electrical current.²⁹

$$A_R = (4\pi m k^2 e / h^3) = 120 \text{ A cm}^{-2} \text{ K}^{-1,2} \quad [6]$$

Principally, thermionic energy converters consist of an anode, cathode and vacuum. The anode acts as an electron collector that is surrounded by a cooling jacket. The cathode is the electron emitter and is heated. The kinetic and potential energy of the electrons in the cathode CB exceeds the work function, and so electrons are emitted into vacuum. A potential difference between the emitter and collector is created in the vacuum as the electrons flow from the cathode to the anode, which creates a space charge layer. Electrons that reach the anode then return to the cathode via a load resistance (e.g. a bulb, fan or motor), providing a circuit for thermionic current. The voltage difference acts as a driving force for the electrical load, and heat energy is converted into electrical energy directly without any losses due to moving parts, see figure 11.⁹ Therefore, thermodynamically, a TEC can be defined as a heat engine.³⁰

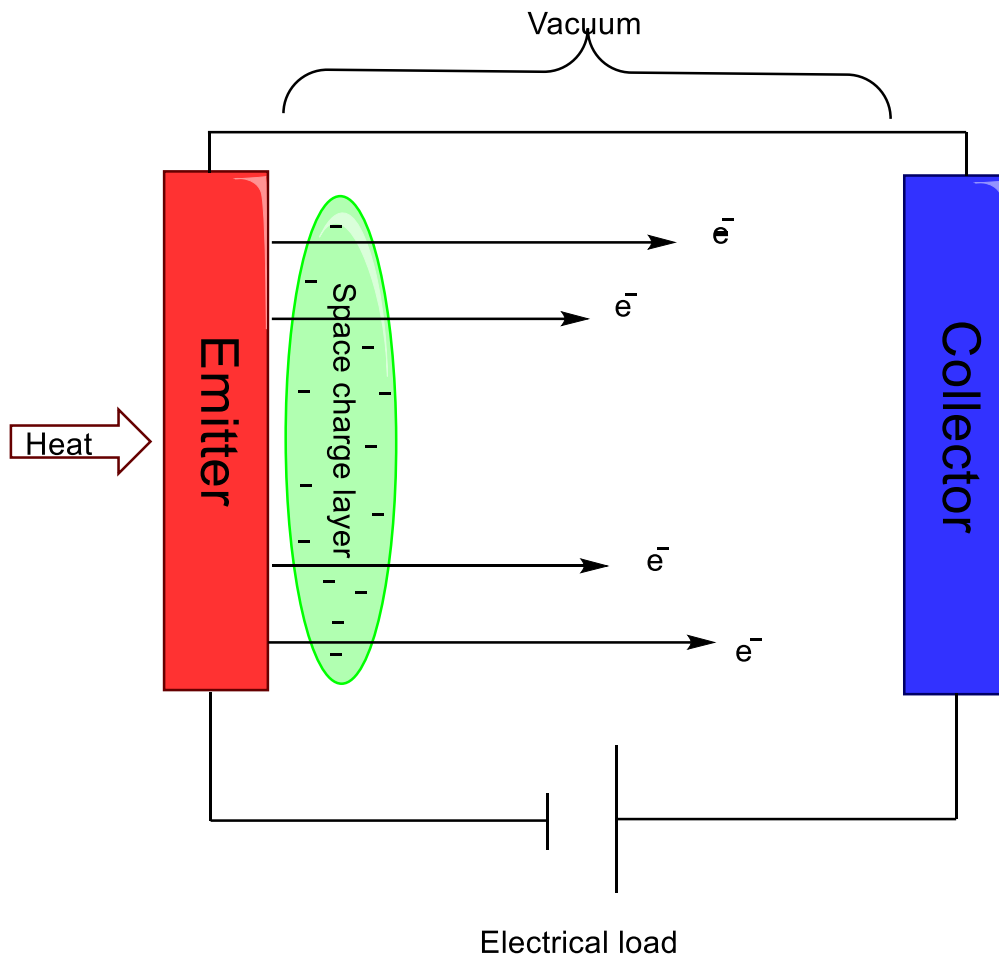


Figure 11 A thermionic energy converter.

The Carnot efficiency, equation [7], defines the efficiency of a heat engine. The second law of thermodynamics states that heat produced in a heat engine is not all used as work. Therefore, equation [7] can be used to calculate how effective the interaction between the 'hot' emitter (T_{hot}) and the 'cold' collector (T_{cold}) is in TEC applications.

$$\eta_{carnot} = 1 - \frac{T_{cold}}{T_{hot}} \quad [7]$$

For the vacuum layer to have a significant effect, a large potential difference must be maintained. Heat convection between the two electrodes via direct radiation counteracts maintenance of the potential difference. To avoid heating of the collector, the electrodes must remain far enough apart. Recently, the distance between electrodes has been reduced down to the order of a few microns, 0.9-3.0 μm .³¹ Thermionic energy converters are of great interest in replacing standard heat engines as they are compact, a 'clean'

source of energy, have a large power output, durable and produce no noise pollution.³² A possible issue regarding TECs is the 'space charge effect' which occurs as a result of the build-up of a layer of electrons above the surface of the emitter. This acts as a barrier for emissions as the lagging electrons form a cloud leading to a reduction in thermionic efficiency.³³

1.53 Lowering the Work Function

The work function (ϕ) of a TEC is a fundamental element of thermionic emission. It is the energy minima for the emittance of an electron from solid to vacuum.³² Consequently, to enhance the efficiency of a TEC, the use of low work function materials in the system is desirable. This is because the ϕ acts as an energy barrier for the emitter and if it is too high, the power output of the TEC decreases. However, a balance must be maintained between the ϕ and the space charge effect. An increase in the current output of the emitter for the ϕ could lead to an increase in the space charge effect, which in turn can decrease the power output of the system.³¹ Therefore, the potential difference between the two electrodes should be maintained for the ϕ at a value greater than 1 eV. Furthermore, the ϕ of each material themselves should be low, particularly at the collector to ensure that high operating temperatures are avoided.³²

A way of reducing the ϕ and maximising TEC efficiency is via the formation of a surface dipole, this can be done effectively by oxidising and functionalising the diamond surface.³⁴ Nanocrystalline diamond surfaces have a smooth surface with enhanced electrical potential. Upon H-termination and removal from vacuum, its surface demonstrates p-type conductivity which is maintained with nitrogen doping.³⁵ However, the large number of grain boundaries affects the current.³⁶

Band bending demonstrated in figure 9 of a nanocrystalline nitrogen-doped diamond surface is beneficial as the amount of sp^2 hybridised carbon clusters increases. This broadens the π and π^* defect states so more electrons have delocalisation potential in these energy levels.³⁷ Consequently, electron transport is improved whilst the effective ϕ remains unchanged. This is a clear indication that nitrogen is bound at the grain boundary regions and have not substituted for carbon at the surface.³⁷ A low effective work function for NDD surfaces is predicted to be less than 2 eV after growth via MWCVD.³⁸ The electron affinity (χ) and its relationship with the ϕ , band gap (E_G) and VBM (E_V) is represented by equation 8.

$$\chi = E_V + \phi - E_G$$

[8]

This equation is for a typical semiconductor where, $\chi = 0$ for a material that also possesses NEA.³⁹

Usually, SCD's are used for thermionic testing. Functionalising these surfaces with materials with low electronegativity and ϕ values (e.g. alkali halides and transition metals) leads to the formation of a dipole moment. This report is focuses on scandium and scandium oxide functionalised surfaces on nanocrystalline diamond. A dipole moment can also be generated that is opposing the substrate surface dipole. This directs to lowering of the ϕ , see figure 12.⁴⁰

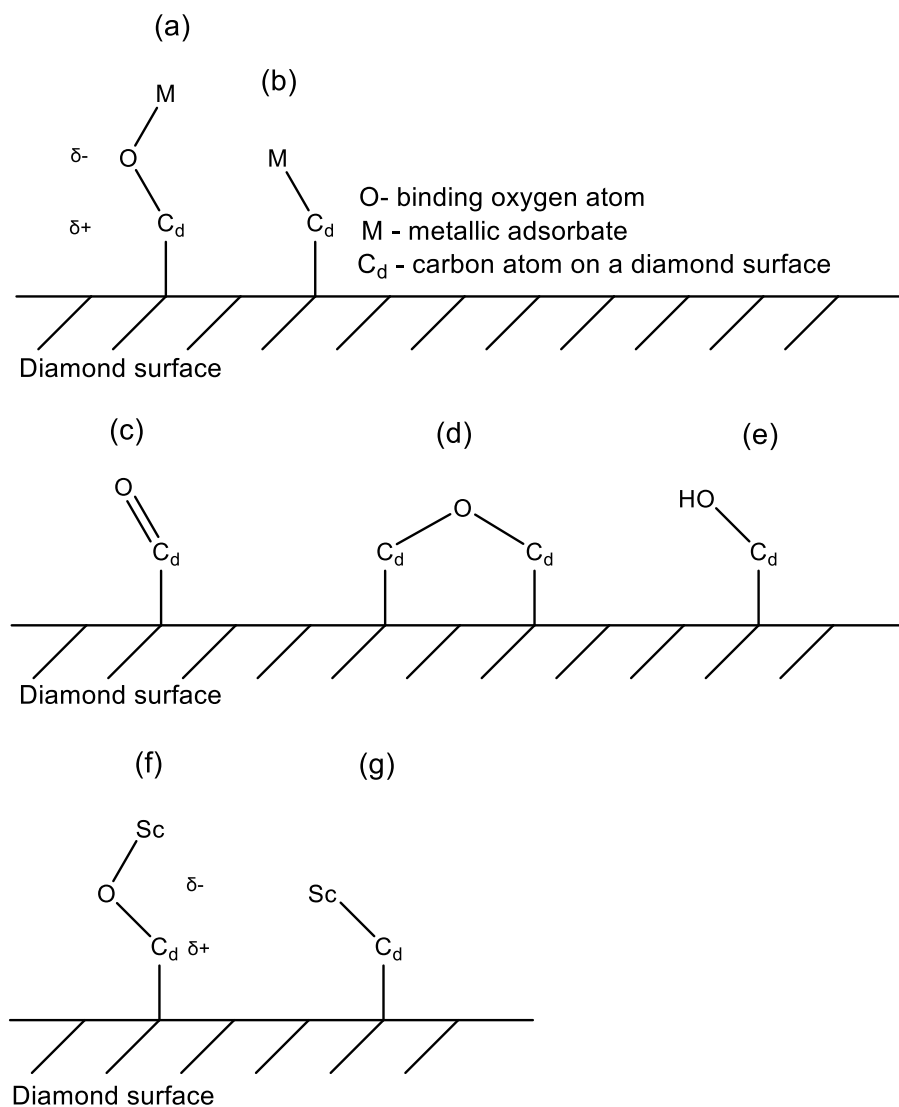


Figure 12 A simplified depiction of functionalised diamond surfaces where O is a binding oxygen atom, M is a metallic adsorbate, C_d is a carbon atom on a diamond surface and Sc is a scandium adsorbate. (a) is a C_d-O-M binding site where the relative dipole orientation is shown, (b) is a C_d-M binding surface where M can be Li, Na, Cs, Mg etc., (c) is a C_d=O surface, (d) represents C_d-O-C_d bridging, (e) is a C_d-OH surface and (f) and (g) is a scandium and scandium oxide functionalised surfaces.

1.6 Surface Terminations

Undoped diamond surface DFT calculations have been reported in recent years that suggest values of -1.1 ± 0.1 eV.⁴¹ The functionalisation of diamond surfaces can lead to a significant increase in NEA, which can be applied to thermionic devices with the intention of replacing cathode materials to improve device efficiency. Functionalisation can be via a variety of materials such as metals, metalloids, metal-oxygen, group I and II metals, transition metals, aluminium, hydroxyl, cubic boron nitride and nitrogen terminations. The most promising results have been produced by small and highly charged metals such as Mg^{2+} , Al^{3+} , Ti^{4+} and Sc^{3+} , as ionisation occurs readily and they have greater kinetic and thermal stability by lying closer to the surface of diamond. Metals can interact with oxygen terminated diamond surfaces via ionic or covalent bonding, as well as weak dipole-dipole interactions, see figure 13.⁹

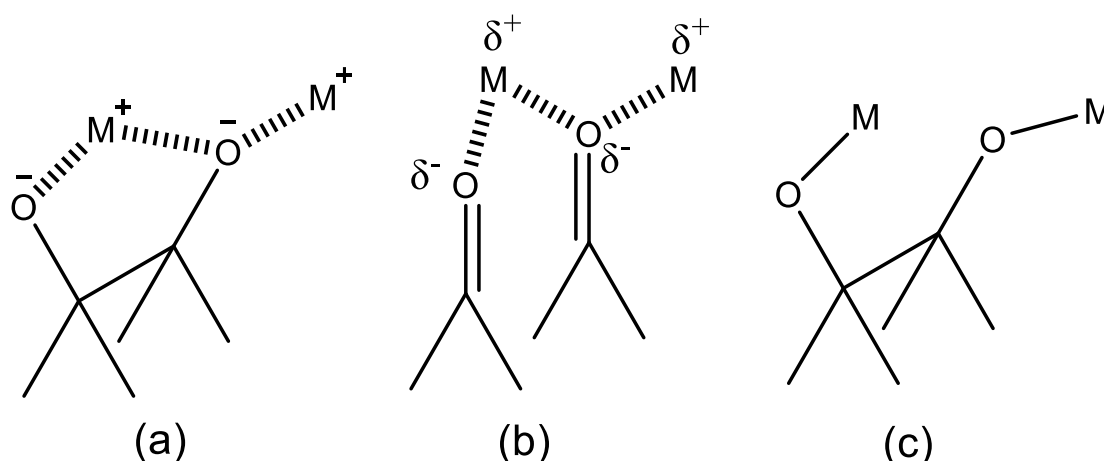


Figure 13 (a) carbon-to-oxygen-to-metal ionic bonding (b) dipolar interactions with bridging between single oxygen atoms and a metal and (c) carbon-to-oxygen-to-metal covalent bonds, where $M = Mg, Al, Ti, Sc$, etc.⁹

In each instance, the metal (M) interaction with the O atom causes it to be partially oxidised and so further oxidation cannot occur as easily. Therefore, the surface becomes more air stable. Non-oxygenated terminations are desirable as NEA can be implemented easily, particularly with metals with an electronegativity of less than 2.6 and conditions under an ultra-high vacuum (UHV).⁹ See table 5 in the appendix, that characterises the relative NEA of metal terminated diamond (100) and (111) surfaces.

1.61 Hydrogen Terminations

A H-terminated diamond surface exhibits NEA, see table 5 in the appendix, and is the simplest way of investigating this phenomenon. For effective thermionic emission, a NEA value of approximately -2 eV is desirable.⁹ The threshold temperature for the thermionic potential ranges between 300-600 °C which is ideal for industrial scale research. The maximum emission-current density ranges between 10^{-4} to 10^{-3} Acm² and the adsorption energy (E_{ad}) is between -4.14 to -5.36 eV/atom for a diamond (100) surface and -4.37 eV/atom for a diamond (111) surface. This highlights the surface stability for the sp² hybridised surfaces.^{38, 42-44}

The process of adsorption is exothermic, with a negative Gibbs energy change through the release of energy. The reaction is therefore spontaneous but despite this, the low E_{ad} of ~4 eV/atom means the likelihood of molecules sticking to a diamond surface is low and is only stable between 600 to 800 °C, over a limited period of time. Post adsorption, at temperatures exceeding 500 °C, a PEA will be demonstrated as H atoms desorb off of the diamond surface leaving it bare and decreasing the overall emission-current efficiency. H-terminated surfaces have the ability to oxidise in air over timescales of hours to days. This is ineffective as it damages the surfaces NEA potential. The greater the negativity of E_{ad} , the stronger the adsorption and the greater the energy required for surface desorption. Therefore, despite H-terminated surfaces having NEA potential, surfaces have been functionalised with metals to improve efficiency and stability under ambient conditions.⁹

There has been prominent advancements into the thermionic energy potential of n- and p-type conductive diamond surfaces. NDD has a promising current density ranging between 1 to 5 mA cm⁻² at temperatures around 500 to 700 °C. When generating an ultra-nanocrystalline surface, NDD has demonstrated low ϕ values of up to 1.67 eV.^{38, 45, 46} However, these samples have a very small Richardson constant of up to only 3.67 Acm⁻² as opposed to its NDD counterpart that reaches a Richardson constant of up to 70 A cm⁻² K⁻², see equation 5.^{38, 42} A high Richardson constant is important as it ensures a high electron current density, which is desirable for the applications of a TEC. At the high temperature conditions of thermionic devices, the deep donor state of 1.7 eV that is representative of NDD H-terminated surfaces that is generally undesirable, is cancelled out as there is enough energy to overcome the barrier for emission.⁹

For polycrystalline PDD, a lower ϕ than NDD occurs at 0.9 eV.⁴⁷ Moreover, for (100) SCD PDD, a ϕ value of 0.67 eV has been exhibited.⁴⁸ Despite this, PDD is less desirable for thermionic device applications as opposed to NDD due to its significantly low Richardson constant values in the range of 10^{-5} to 10^{-7} A cm⁻² K⁻² for polycrystalline PDD and (100) single crystal PDD, respectively. This means that their electron emission rates are low.⁴⁹

1.62 Metal-oxygen Terminations

Metal-oxygen terminations occur due to deposition of a metal on top of an oxidised surface. This surface is often semiconducting, with a high thermal stability constant and maintains a low work function value. Despite oxygen having an electronegativity of ~ 3.5 , if an electropositive metal binds to the O-terminated surface, NEA is exhibited.⁵⁰

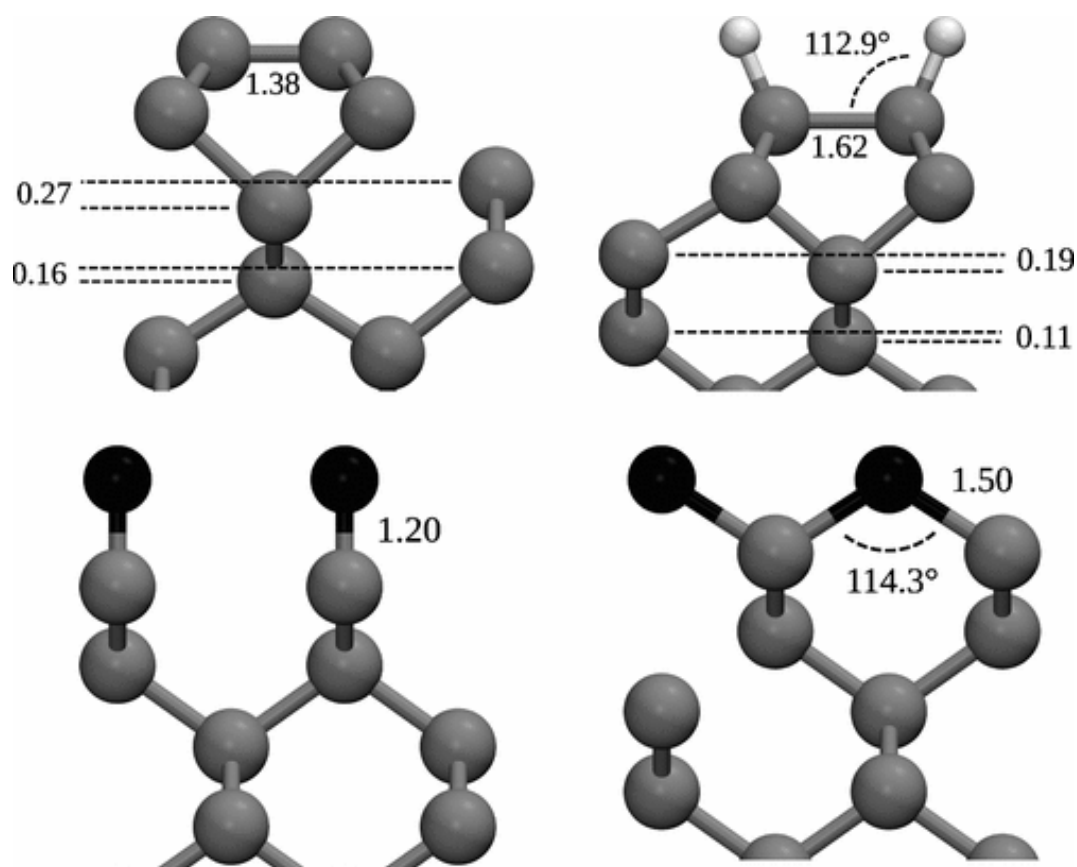


Figure 14 Optimised structures of (a) an C(100)-(2 x 1) surface fragment, (b) C(100)-(2 x 1) : 2H surface fragment, (c) a C(100)-(1 x 1): O carbonyl surface fragment and (d) a C(100)-(1 x 1): O ether surface fragment. The unit for length is in angstroms (Å).⁵¹

Images (a), (b), (c) and (d) in figure 14 were calculated by plane wave density functional theory (DFT) calculations and the electron affinity of these surfaces were measured. O-terminated surfaces form a carbonyl, generally a ketone, or ether which causes bridging leading to a higher energy structure forming. *Ab initio* results regarding the C (100)-(1 x 1): O, ether and C (100)-(1x1): O, carbonyl, electron affinity are 2.63 eV and 3.75 eV,

respectively. As demonstrated in figure 13, metals bind with O-terminated diamond surfaces via ionic, covalent and surface dipole interactions.^{9,52}

1.63 Group I and II Oxygen terminations

A lighter metal is less susceptible to steric crowding and therefore, adsorb more strongly to a surface. This endurance, through ionic bonding to avoid the problems of desorption, makes lighter metals more desirable for thermionic devices, see (a) of figure 13.⁹ This ensures that group I and II metals, such as Li and Mg, lie close to the surface and produce high surface coverage. On the other hand, group I and II metals such as K and Cs have little thermal stability and weak dipolar interactions as a result of steric crowding. These atoms are large and sit loosely on a substrate surface, resulting in easy desorption at low temperatures. Due to being small, highly charged and with high thermal stability compared to the other group I and II metals, Li comes out on top for being predicted to produce the largest NEA value, see table 5 in the appendix.^{51, 53, 54} However, the coordination and retention of the group I metal, Li, on a substrate surface suffers difficulties in reproducibility.⁵⁵ This could be as a result of uncontrolled bonding to an oxygen layer where excess Li is often deposited. It desorbs easily and results in the surface being unstable. This is particularly prevalent after annealing at temperatures $>600\text{ }^{\circ}\text{C}$ during thin film deposition under UHV condition, see figure 15. The greater the deposition of Li on a O-terminated diamond surface, the lower the ϕ and the closer the transition is from a PEA surface to an NEA surface.⁹

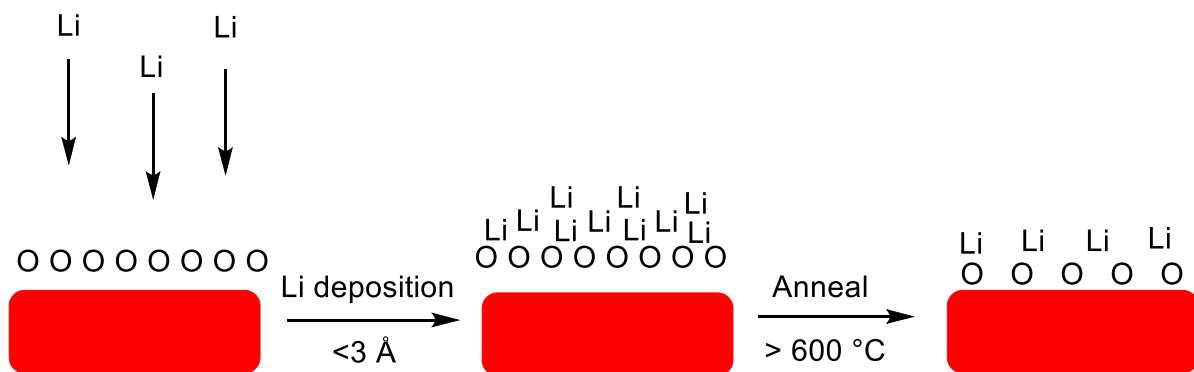


*Figure 15 Thin-film deposition of lithium under UHV conditions on an O-terminated diamond surface where excess Li is removed after annealing at temperatures above the activation temperature of $600\text{ }^{\circ}\text{C}$.*⁹

Magnesium is a group II metal that also exhibits a relatively high NEA, see table 5 of the appendix. The deposition of Mg onto an O-terminated diamond surface is resistant to exposure to high temperatures as well as immersion into water, proving it to be a highly stable surface. Moreover, compared to Li, it does not require thermal activation. It easily adsorbs to an O-terminated diamond surface due to its ability to coordinate to two O

atoms and produce relative dipoles. Both Li and Mg are resistant to surface transfer and are suited to applications that involve electron yield where an UHV environment is not necessary. Consequently, as thermionic energy converters are under an UHV system, these group I and II metals are not suited for thermionic applications, despite having desirable NEA values.^{9, 56, 57}

1.64 Aluminium Oxygen Termination

Aluminium produces NEA and a large adsorption energy on a O-terminated diamond (100) and (111) surface with a 0.25 ML Al coverage. This is as a result of the formation of strong ionic bonds between the Al and O.⁵⁸ However, its NEA value is relatively small so not optimal and by increasing the ML surface coverage, Al-Al metallic bonding can occur which depletes the surfaces ionic potential leading to PEA. Moreover, the surface has a low adsorption energy of -6.36 and -7.31 eV for a diamond (100) and (111) surface, respectively and so the surfaces were not found to be thermally stable. Moreover, evidence suggests that Al has the potential to break C-O bonds and remove the O-termination to form a layer of aluminium oxide on the surface of diamond which harms the samples structural integrity further.⁹

1.65 Transition Metal Terminations

Transition metal terminations onto oxygen terminated surfaces have been explored experimentally. Oxygen is chemisorbed onto the diamond surface and has been proven to increase the field emission threshold following the deposition of transition metals such as Cu, Sc, Ti, Ni, Co and Zr. Further transition metals have been proven to incur NEA, all of which are detailed in table 5 of the appendix.⁵¹ Further theoretical studies have shown that the adsorption surface plays a significant role on surfaces transitions from a PEA surface to a NEA surface. M-O-C diamond surfaces have a large adsorption energy in comparison to a H-terminated diamond surface and group I and II metal terminations. Therefore, as long as NEA is exhibited, the surface is more thermally stable. They also have a lower Schottky barrier and so are promising candidates for electron emission applications. Aside from scandium, which is the focus of this report, Ti, which has the ability to form carbide structures, has a promisingly high adsorption energy over a range of surface coverages. For the ML and sub-ML Ti coverage, NEA have been reported, see table 5 of the appendix.⁵⁹

1.66 Metal terminations

Metal terminations are considered to be the simplest method of producing NEA on the surface of diamond. Deposition of a metal with an electronegativity <2.6 onto a bare diamond surface under UVH alongside techniques such as sputtering and atomic layer deposition can result in a thick layer of this metal bulk adsorbate that directly impacts the electronic properties of the surface.⁹ Co, Cu and Zr have been proven to exhibit small NEA values ranging between the values detailed in table 5 of the appendix.^{59, 60} Ni on a diamond (100) and (111) surface, as well as Ti on a diamond (100) surface, also exhibit NEA as shown in table 5. Ti at a layer of 3 Å deposited on NDD leads to a emission current similar to H-terminated diamond but with more thermal stability up to temperatures of 950 °C, allowing for optimal surface emission activation. Ti, V and Al are metals that have the potential to form carbides and this is favourable as there is a short M-C bond resulting in a more thermally stable surface. Copper does not exhibit a large NEA as it lacks the ability for carbide formation and desorbs readily at raised temperatures. Optimal surface coverage for Ti with the lowest NEA value of -1.6 eV was as a result of a 0.5 ML on a diamond (100) surface.⁹

1.67 Positive Electron Affinity Surface Terminations

CVD diamond, due to its electronic properties being open to extensive manipulation, is commercially practical for an expansive selection of applications. The electron affinity of halogen terminated diamond has been explored and proven to produce stable PEA surfaces. For example, fluorinated diamond surfaces have produced PEA in the range of 1.17 to 2.63 eV. On the other hand, for chlorinated surfaces its termination is thermodynamically unfavourable. This leads to a lower surface coverage and in-turn, a lower PEA.⁶¹ Recently, fluorine terminated diamond (110) surfaces have been explored as a promising contender for NV-based quantum sensors. This is due to it not having any surface electron spins, PEA and no inter-bandgaps correlated to the surface.⁶² Technology that is utilised today that involve halogen-terminated diamond surfaces include heat sinks, electrochemical sensors and detectors. A H-terminated surface produces an NEA of -1.30 eV with the relative dipoles demonstrated in figure 8, where the O-terminated diamond surface has a PEA of +1.70 eV.¹⁰

1.7 The Thermal Expansion Coefficient

The thermal expansion coefficient of SCD is low, in a range of $0.7 \times 10^{-6} \pm 0.3 \times 10^{-6} \text{ K}^{-1}$.⁶³ This must be taken into consideration under synthesis in MWCVD reactors due to its homoepitaxial growth being under high temperature conditions.

It is important for homoepitaxial growth that diamond films are deposited on substrates with a similar thermal expansion coefficient to prevent delamination. Drastic differences in the thermal expansion coefficient between substrate and film results in an increase in intrinsic stress, causing the surface to delaminate. By regulating these parameters, substrate-film adhesion and consequently overall purity of sample and efficiency can be improved.⁶⁴ The thickness of diamond thin film affects the growth rate and quality of film. The thicker the growth, there is a decrease in growth rate and so surfaces are more susceptible to residual stress.⁶⁵

In industry, silicon is the primary source of substrate for diamond thin film. Si substrates of 450 nm have the potential to produce good quality SCD thin films. Silicon has a thermal expansion coefficient similar to diamond, hence it being a suitable substrate for industrial applications. On the other hand, molybdenum has improved surface adhesion to diamond whilst also possessing a similar thermal expansion coefficient, which leads to the formation of better quality films. It has greater potential as a substrate for overcoming thermal and intrinsic stress during growth.⁶⁶ Nucleation on silicon results in crystal lattice formations of 0.15 μm on average, but the grain boundaries are less well defined under SEM analysis.⁶⁷ Molybdenum has the potential to produce crystals with an average diameter of $\sim 0.6 \mu\text{m}$ at a reduced temperature to silicon, despite requiring a longer nucleation time period. Surface morphology of diamond with molybdenum as a substrate produces a smoother textured surface, with a lower operating temperature as opposed to its silicon counterpart.⁶⁷

1.8 Thermionic Emissions from NDD vs PDD and Molybdenum as a Substrate and Electrode

The NDD surface is more favourable in comparison to PDD. Despite PDD having a lower ϕ value of 1.18 eV as opposed to 1.44 eV for NDD under vacuum at temperatures up to 500 °C, its Richardson constant is significantly lower with a value of 0.003 A/cm² K² compared to 4.05 A/cm² K² for NDD when deposited on a molybdenum substrate, see figure 16. The low Richardson constant for PDD is related to it being highly sp^3 hybridised which increases its electric resistivity which is undesirable. Not only is molybdenum useful as a substrate surface, it also has the potential to enhance the work function and reduce space charge effects when making up the emitter and collector electrodes of a thermionic energy converter and combining its function with caesium vapour. Caesium vapour exposed to molybdenum electrodes at 1 mTorr has the potential to reduce the work function and operating temperature by 0.5 eV and 650 °C, respectively.⁶⁸ Other sources state that NDD on a molybdenum substrate has an effective ϕ in the range of 1.5-1.9 eV which is significantly higher than PDD due to its deep donor level of $\chi = 1.7$ eV below the CBM and this value is high enough to produce a significant barrier for emission.⁶⁹

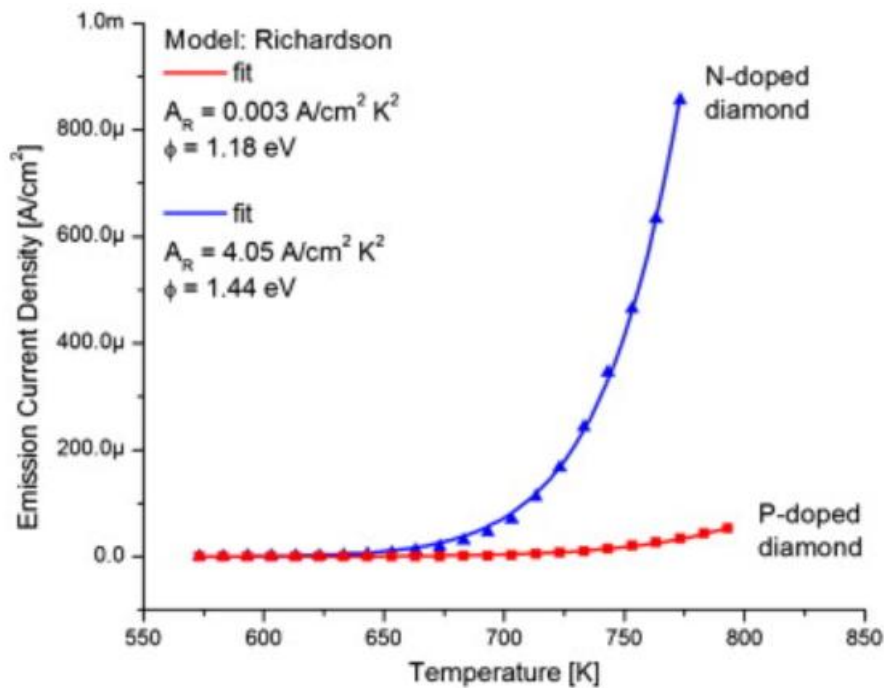


Figure 16 A graph representing thermionic emission data from P- and N- doped diamond films and their corresponding Richardson-Dushman values.⁶⁸

1.9 Project aims

For the purpose of this report, nanocrystalline NDD is grown on a molybdenum substrate. A H-termination is performed and its thermionic emission is measured. It is then replaced with a scandium oxide termination and its thermionic emission is measured again, see figure 14. Density functional theory (DFT) calculations of Sc-terminated diamond (100) and (111) surfaces show an decrease in dimer bond lengths by 0.24 Å, as a result of the C_d-H bonds in figure 12 breaking. It resulted in the formation of smooth and well-ordered terminated surfaces. This is useful as scandium that has been deposited on a diamond (100) surface has a calculated NEA value of -1.45 eV via UPS analysis whilst being able to maintain stability at raised temperatures of up to 900°C, which is useful for electronic applications. The ϕ of bare diamond that has been deposited with scandium are 3.22 ± 0.02 eV and 3.53 ± 0.02 eV for a (100) and (111) surface, respectively. This value is still relatively high which is unfavourable for efficiency of the system, so exploration into nanocrystalline NDD surfaces are to be explored for the purpose of this report.⁴⁰ Most recently, scandium deposition of a 0.25 monolayer on a bare (100) diamond surface resulted in a NEA of -1.02 eV and a ϕ of >3.63 eV. DFT calculations suggested the potential for NEA of -0.94 eV and a ϕ of 2.79 eV for a ScO- terminated diamond surface which is stable *in vacuo* up to 700 °C.⁷⁰

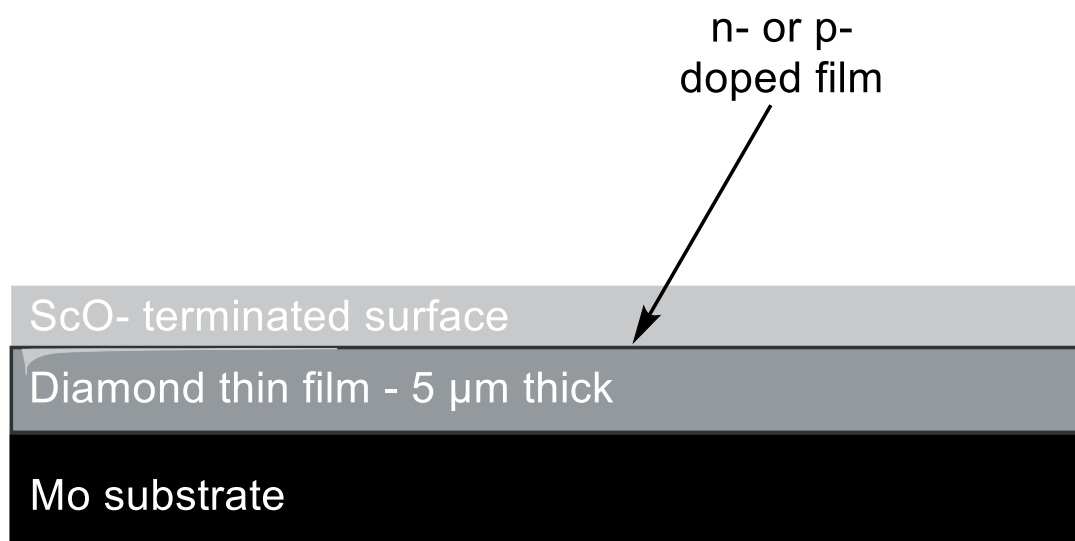


Figure 17 Sample fabrication of a ScO-terminated NDD surface grown on a Mo substrate.

2.1 Sample Preparation

In this study, square-shaped, pure molybdenum plates (10 × 10 mm) were used as the substrate. The substrates were sonicated for 15 minutes in acetone (1 mL). Then they were cleaned with isopropyl alcohol (1 mL). Nanodiamond particles (NanoAmando), acquired from NanoCarbon Research Institute Limited (Nagano, Japan) were seeded onto the diamond surface via manual abrasion. The samples were then washed in acetone (1 mL).⁴⁰

Micro- and nano- crystalline NDD samples were grown using MWCVD reactor. A 2kW magnetron tuned by a linear antenna at the top of the reactor produced microwaves which were 2.45 GHz. This passed into the reaction chamber via a quartz window. The MW power forms the plasma that initiates reactions leading to CVD.⁴⁰

Mo1, Mo2 and Mo5 were HNDD samples and Mo3 and Mo4 were LNDD samples, see table 6 in appendix that defines the samples and their relative growth conditions. The concentration of gases were measured in standard cubic centimetres per minute (sccm). Each sample was mounted in the chamber on a tungsten disk which was placed on a spacer Mo wire (8 milli-inches) on the baseplate of the reactor. This limited contact with the cooling system and the substrate and allowed the substrate to reach the required growth temperature of ~900 to 1000 °C.⁴⁰

Diamond growth was initiated by pumping down the chamber to 30 mTorr. Then H₂ gas (300 sccm), produced by a hydrogen generator (NG7 Nobelgen), was flowed into the chamber and plasma was struck at 15 Torr using 650 W (40% of total power) of microwave power. As the plasma stabilized through tuning, the pressure was increased to 50 Torr and CH₄ (12.4 sccm) and N₂ (4.00/0.30 sccm) was introduced. The rates of gas flow were monitored through a digital MFC panel. As the plasma stabilized once again, the power was adjusted to ~1.2 kW and the pressure to ~120 Torr to maintain a temperature ~900 to 1000 °C, see table 6 in the appendix for the relative growth conditions for each sample.⁴⁰

The temperature was measured via a single-colour optical pyrometer ($\lambda = 2.2 \mu\text{m}$) with an emissivity for Mo set to 0.18. The plasma, temperature and pressure were continuously monitored throughout the growth to ensure stability was maintained, see figure 18.^{7, 40}

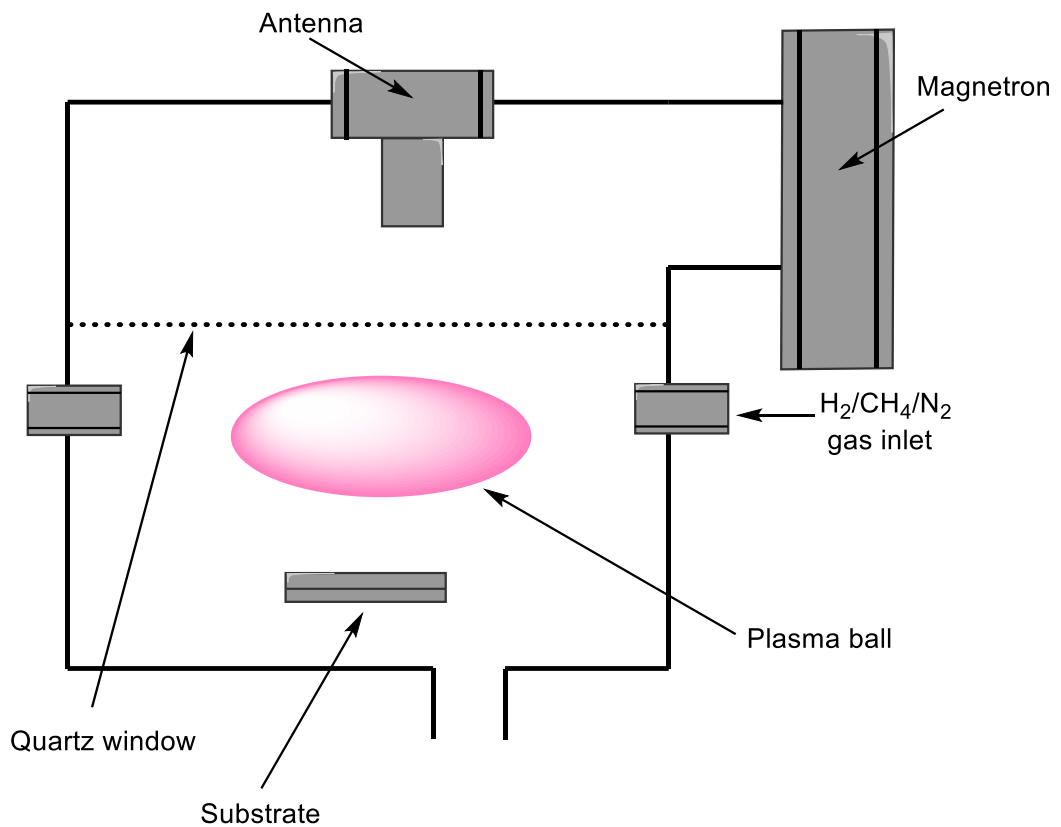


Figure 18 A schematic representing a microwave plasma-assisted (MWCVD) reactor.

2.2 Pt/Pd Coating

NDD is a non-conductive surface with an imbalance of electrons. Therefore, irregular brightness, partial imaging and distortion occurs when analysed under SEM.⁷¹ To mitigate this effect, the sample surfaces of Mo1, Mo2, Mo3 and Mo4 were treated in a conductive coating layer of 80-20 wt% of Pt-Pd (99.99% purity, 57mm diameter, × 0.5 mm thick, $\rho = 19.56 \text{ g/cm}^3$), from Testbourne Ltd., Hampshire, UK. This balanced charge across the sample surface.

2.21 Scanning Electron Microscopy (SEM)

Samples Mo1, Mo2, Mo3 and Mo4 were then characterised using a JSM-IT300 SEM kit from JEOL and the grain size and thickness of the SEM images were analysed using the license free software, *ImageJ*. SEM visualises a sample surface on the basis of focused electron beams. It works under a high-vacuum system to minimise contamination and scattering of the electron beams due to the presence of air particles. An electron gun with a W or LaB₆ hot filament emits electrons which are then accelerated through ~50 kV,

using energy from electrostatic plates that have a high potential. The electron beam is then focused onto a spot of 1 to 10 nm diameters found on the sample surface via a series of electrostatic objective lenses, see figure 19. An applied oscillating potential rasters the electron beam across the sample, and as it hits the surface, the electrons scatter, and are sensed by a nearby detector. Alternatively, secondary electrons that are ejected from the bulk of the sample by collisions with the primary electron beam, emit off the surface and are identified by a different detector. The detector output results in a high resolution image of the surface morphology of the sample.⁴⁰

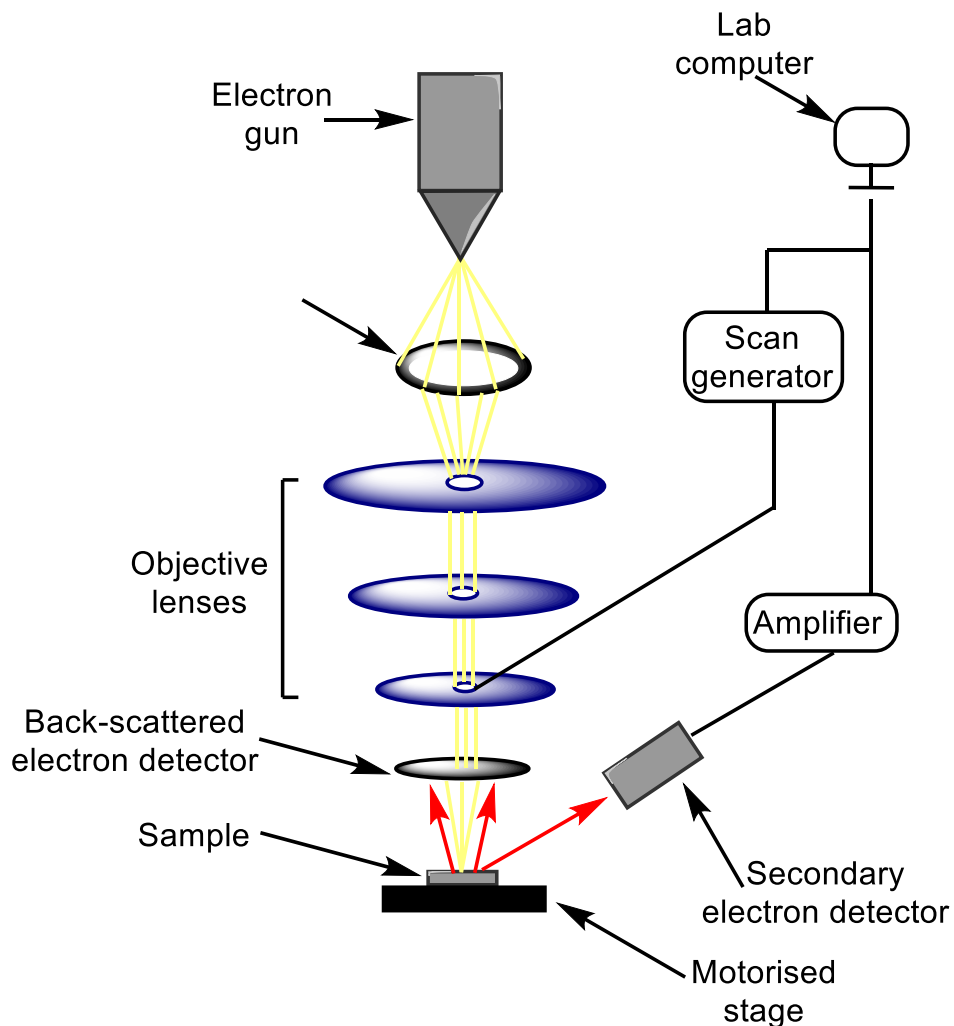


Figure 19 A schematic representing a standard SEM device.

2.22 Acid Wash

The Pt/Pd (80:20) layer was removed via acid cleaning. An aqua regia was used at a HCl:HNO₃, (3:1) ratio at room temperature. The samples were then sonicated for 15 minutes in acetone to remove any traces of the acid.

2.3 Laser Raman Spectroscopy

Laser Raman spectroscopy was used to characterise the quality of the diamond thin films. This was completed using a confocal micro-Raman system (Renishaw RM 2000). A laser beam was focused onto the sample, where it excited electrons into higher energy states. The reflected laser light has reduced energy (due to the Raman effect) and this is collected and dispersed in a spectrometer to produce a Raman spectrum.

There are three distinct energy transitions that occur due to Raman spectroscopy, see figure 20. The excitation source was an Ar⁺ laser with a wavelength visible in the green light region of 514 nm. The software used to monitor the samples for data acquisition was *Windows-based Raman Environment (WiRE 2.0)*.⁴⁰

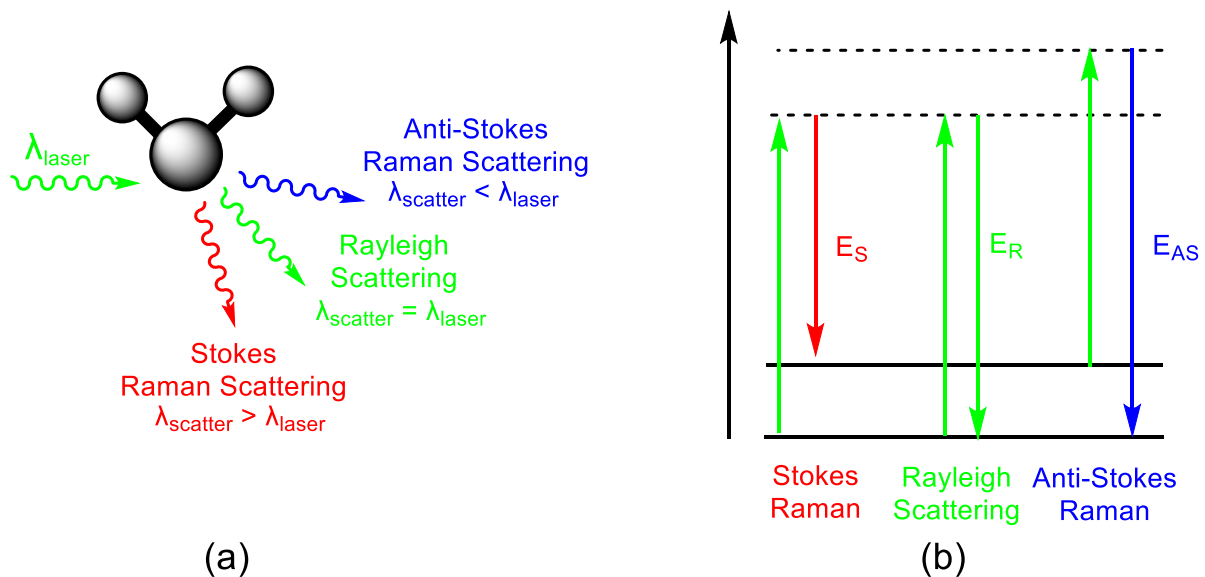


Figure 20 The principles of Raman spectroscopy where (a) is a H-terminated diamond surface fragment affected by laser-induced vibrations of the Stokes and Anti-Stokes shift where excited electrons relax to a higher or lower energy level resulting in scattering and the Rayleigh scattering that is due to the electron relaxing to its original energy level where (b) represents the relative energy level diagrams of the three shifts.⁴⁰

2.4 Hydrogen Termination

Hydrogen terminations on samples Mo2, Mo4 and Mo5, see table 6 of the appendix, were completed using a MWCVD reactor, which involved multiple steps. Firstly, samples were exposed to H₂ plasma (300 sccm) at ~130 Torr and 1300 W for 2 minutes at a substrate temperature of ~900 °C to desorb any existing surface terminations. Conditions were reduced to ~82 Torr and 1000 W to maintain a surface temperature of ~550 °C for 2

minutes. This resulted in H-termination. The plasma was then turned off and the H₂ flow and pressure was left constant for 2 minutes. The substrates were cooled down in a H₂ atmosphere, which prevented oxygen from replacing hydrogen from the surface.⁴⁰

2.5 Laser Etching

For thermionic testing, the sample must be heated to temperatures ~900 °C in the thermionic testing kit see figure 23. However, sample heating cannot be done using a simple resistive wire heater as the stray electric and magnetic fields from the electric wire would affect the ejected electrons. Consequently, heating was done by shining a high-power CO₂ laser onto the back of the substrate. However, to transfer energy efficiently from the laser into the Mo substrate, the backside of the substrate was etched into a grating pattern with a groove separation similar to that of the laser wavelength.⁷

Surface plasmon polaritons (SPP) are electromagnetic waves that have the ability to produce localised heating. As electrons oscillate through the sample surface, an interface between the molybdenum transition metal and dielectric insulator, diamond thin film, was generated. By utilising SPP through plasmonic grating, an optimal backside substrate surface was developed that was highly compatible for thermionic emission testing. The molybdenum was ideal for plasmonic heating as it was mechanically stable with a high thermal steadiness and was a refractory material with optical properties that sit broadly in the IR region. Therefore, as SPP electromagnetic waves are introduced into the grating by the CO₂ laser, it was coupled to free electrons in the metal which moved up into higher states of energy, breaking out of the equilibrated system.⁷

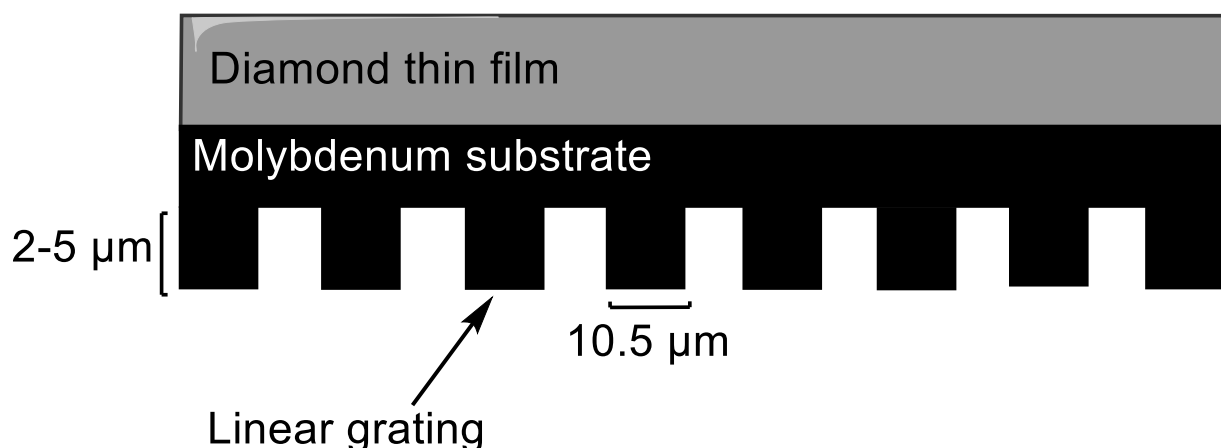


Figure 21 The plasmonic grating pattern on the backside of a molybdenum substrate, opposite the side where the diamond thin film was grown. Relative parameters are shown of a period of 10.5 μm and a depth ranging between 2-5 μm.⁷

Literature suggests that a linear grating pattern period of 10.5 or 10.6 μm are optimal for creating an SPP boundary, see figure 21.⁷ Pairing the in-plane momentum of incoming photons alongside the propagation constant at the interface is necessary, see equation 9:

$$\beta = k_x = |\vec{k}| \cdot \sin\theta + / - vg \quad [9]$$

, where β is the propagation constant of SPP at the interface, \vec{k}_x is the in-plane propagation wave vector, $|\vec{k}|$ is the incident wave vector, $v = 1, 2, 3 \dots$, $g = 2\pi/a$ and a is the periodicity of the interface structure. The in-plane momentum is defined by equation 10:

$$k_x = |\vec{k}| \cdot \sin\theta \quad [10]$$

Consequently, when a wavelength of light (λ) is coupled to an interface with the intention of exciting an SPP, a period of $a \sim \lambda$ with $a < \lambda$ structure must be patterned for the coupling conditions to be fulfilled, see figure 22. When the conditions for equations 9 and 10 were satisfied with a $\sim 10.5 \mu\text{m}$ grating, the molybdenum substrates interaction with electromagnetic radiation was enhanced as light was trapped in vacuum on the interface between the metal and air whilst withstanding temperatures $> 1000 \text{ }^\circ\text{C}$.⁷

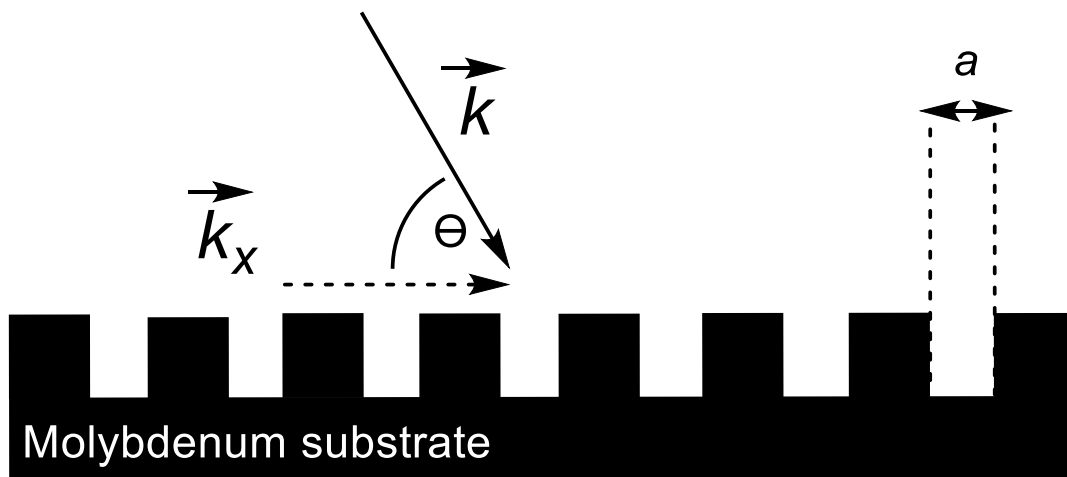


Figure 22 The matching of electromagnetic radiation and SPP with linear grating. Here, \vec{k} is the total momentum of incident photons, \vec{k}_x is the momentum component that is parallel to the interface between molybdenum and diamond and a is the period of the patterned grating.⁷

The laser micromachining system used was an Alpha 532, Oxford Laser Ltd., that has a diode-pumped nanosecond (Nd:YAG) laser with a base source wavelength of 542 nm. The system operates with a laser power of up to 5 W at 10 kHz and a pulse duration of up to 15 ns. The laser spot was $\sim 5 \mu\text{m}$ in diameter. Sample staging involves servomotors that shuttle in the x , y , and z direction which was operated via the software *Cimita* and G-coding language. Linear grating patterns were produced on the backside of Mo2, Mo4 and Mo5 using laser micromachining with a separation of $10.5 \mu\text{m}$. This spacing had the potential to maximise heat transfer from the CO₂ heating laser of the thermionic testing kit.⁷

2.6 Thermionic Testing

A thermionic energy converter simulator (TECsim) apparatus was used to measure the current density dependence on temperature *in vacuo* for the n-type diamond samples, see figure 23. The machine simulated a TEC through an emitter-collector set-up, laser heating module and a current flow measuring system. Samples Mo2, Mo4 and Mo5 were mounted onto the centre of a quartz plate, above the circular hole with a diameter of $\sim 8 \text{ mm}$. Mo clips were used to hold down the sample diagonally to one another. To measure the current density, a 10 mm diameter cylindrical W collector was used. The separation was controlled by a Z825BV, Thorlabs, Inc. stepper motor before and during the sample mounting. The emitter (cathode) mounted the sample whilst the collector (anode) was contained in a stainless-steel chamber under high-vacuum conditions ($\sim 2.5 \times 10^{-7} \text{ mbar}$) produced by a turbomolecular pump. The laser used to heat the emitter was an IR CO₂ beam (Synrad FSV40KFD, Firestar) with a wavelength of $10.6 \mu\text{m}$ and a power output of 40 W. Three Au-coated Cu mirrors focused the beam towards the backside of the sample. The beam travelled through a ZnSe chamber window that had an anti-reflective coating of up to $12 \mu\text{m}$ (WG71050-G, Thorlabs, Inc.). The beam size was varied between 2.5 to 6.0 mm in diameter.⁴⁰



Figure 23 Image of the thermionic testing kit device.

Changes in temperature were monitored via a two colour IR pyrometer (Spotmeter R160, Land Instruments International Ltd.) and an emissivity of 0.125 was selected that is specific to molybdenum. The temperature was controlled via *LabVIEW* virtual software where the proportional integral derivative (PID) and laser power output were adjusted for each sample. Each cycle measured during each experimental run is depicted in figure 24 as a trapezium setpoint profile from 300 to 900 °C and a ramp rate of 1 °C per second.⁴⁰

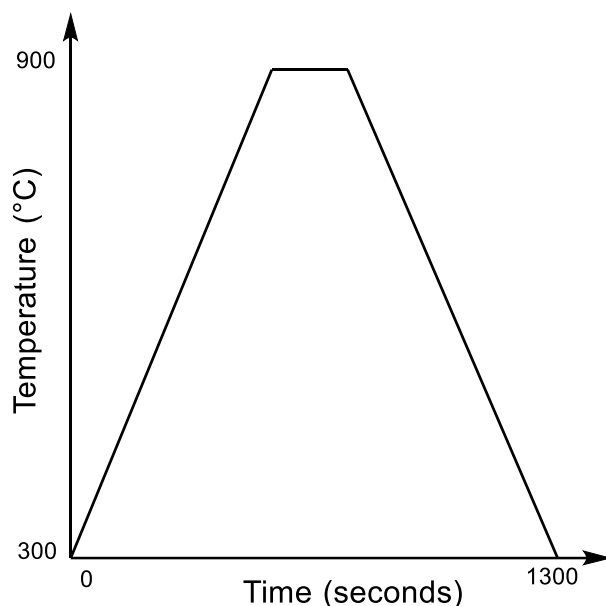
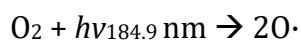


Figure 24 Representing the trapezium setpoint temperature profile from 300 °C to 900 °C, over 1300 seconds with a ramp rate of 1 °C per second. The temperature remains constant at 900 °C for 100 seconds.

The vacuum gap between emitter and collector of each sample was 120 µm. The system was connected to a DC power supply (HY3003D) and an ammeter (Keithley Model 2750). A negative bias voltage was maintained of 25 V.⁴⁰

2.7 Oxygen Termination

O-termination was completed through use of a UVO-cleaner kit (Model 42, Jelight Company Inc.) which works at room temperature and pressure. Samples Mo2, Mo4 and Mo5 were treated for 30 minutes in the system. A mercury lamp generated UV irradiation of atmospheric air over the samples (~ 4 cm) at a wavelength of 184.9 nm. O₃ was generated in a cascade of reactions:



[11]



The O_3 molecule then absorbed UV light at a λ of 253.7 nm and decomposed:



This formed active radicals that replaced C-H bonds found at the surface of diamond to produce a full monolayer (ML) oxygen coverage.

2.8 NanoESCA

The Bristol NanoESCA facility operates under UHV conditions for its multipurpose use of preparation, deposition and analysis chambers that are divided by gate valves, between which samples can be shuttled. The samples submitted to the Bristol NanoESCA were Mo4 and Mo5, see figure 25. ⁴⁰

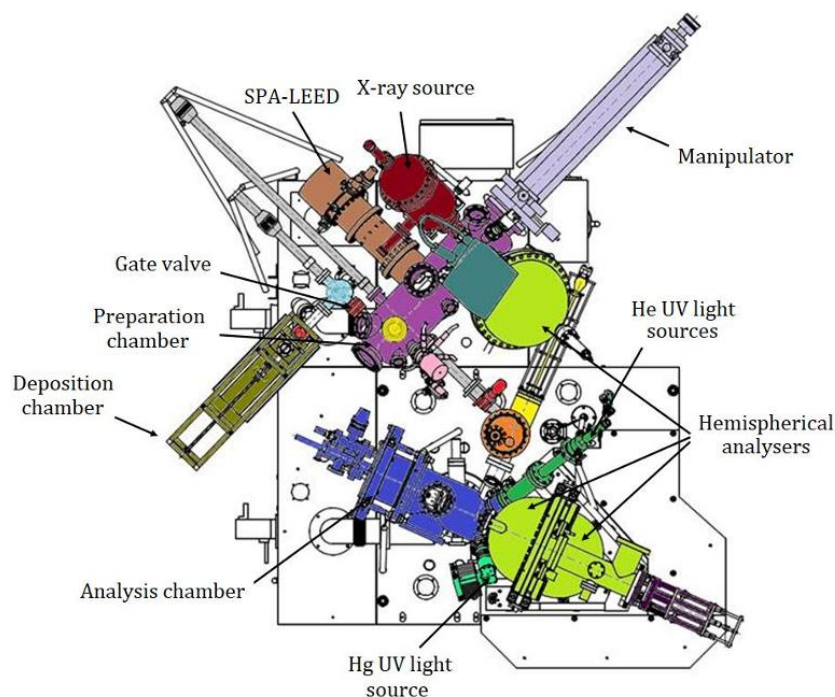


Figure 25 Representing a labelled diagram of the Bristol NanoESCA facility.⁴⁰

The samples were placed under UHV and annealed at 300 °C for 1 hour. Then a 0.25 ML of scandium was deposited for 4.5 minutes at room temperature. Mo5 was annealed at

700 °C and XPS and UPS analysis was performed. Mo4 was annealed at 500 °C. Both samples were then tested in the thermionic testing kit.

2.81 Preparation Chamber

This chamber consists of a sample manipulator that can anneal samples up to ~1250 °C, X-ray spectroscopy (XPS), a spot-profile analysis low energy diffractor (SPA-LEED) and an argon-ion sputter gun whilst operating at 2×10^{-11} mbar, see figure 25. To heat the sample, a coiled W filament with a maximum power of up to 130 W was used that is calibrated to a DC current in the range of 2.25 to 7.15 Å.⁴⁰

2.82 X-ray Photoelectron Spectroscopy (XPS)

XPS was used to investigate the elemental composition and electronic states of the surface of Mo5. The sample was exposed to a fixed-energy X-ray beam Al K α with a photon energy of 1486.7 eV. This caused electrons to excite into the higher core levels and be released as photoelectrons which travel into vacuum with no loss of KE. In order to measure the KE, an electron optics lens accelerated the photoelectrons into a hemispherical analyser. Consequently, the binding energy (BE) was calculated via equation 14:

$$BE = h\nu_{1486.7} - KE \quad [14]$$

, which is characteristic of each atom and was used to identify the atom composition of the surface. Shifts in the BE may arise as a result of the different chemical states of elements. Through probing, all elements within a ML composition of 0.1 to 1% can be identified. *MATRIX* software was used to analyse the data.⁴⁰

2.83 Deposition Chamber

The deposition chamber enabled the *in situ* surface modification of Mo4 and Mo5, where e-beam evaporation and gas cracking were used for scandium deposition. A degassed Mantis QUAD EV-C evaporator was used at 1.0×10^{-9} mbar alongside a Sc rod (99.99%, 2 mm diameter \times 28 mm) from Testbourne Ltd (Hampshire, UK), that was the e-beam target. Atoms of Sc evaporated off the rod at a controlled rate and deposited on Mo4 and Mo5. In order to achieve a 0.25 ML in 4.5 minutes at RT, a deposition rate of 0.183 Å min⁻¹ was used.⁴⁰

2.84 UV Photoelectron Spectroscopy (UPS)

In the analysis chamber, a channeltron detector was used to provide information into the shallow core levels of the sample surface. A monochromatic helium lamp with photon energy of 21.2 eV for He (I) and a spot diameter of $\sim 300 \mu\text{m}$ was used for excitation through capillary discharge. Valence electrons were excited into higher energy states of the CB with no obstruction to vacuum. The pressure of the chamber was 3.3×10^{-9} mbar with an energy resolution of 0.14 eV.⁴⁰

3.1 Characterisation of Seeded Molybdenum

Nanocrystalline seeding through abrasion with nanodiamond powder was characterised using laser imaging, see figure 26. The abrasive powder has resulted in the formation of sharp nanostructures being left behind on the surface. In figure 26, (a-c) represents a pristine Mo1 surface that is relatively smooth, with some scratches and trenches. After seeding, (d-f) demonstrates the formation of nanocrystal protrusions uniformly covering the surface.

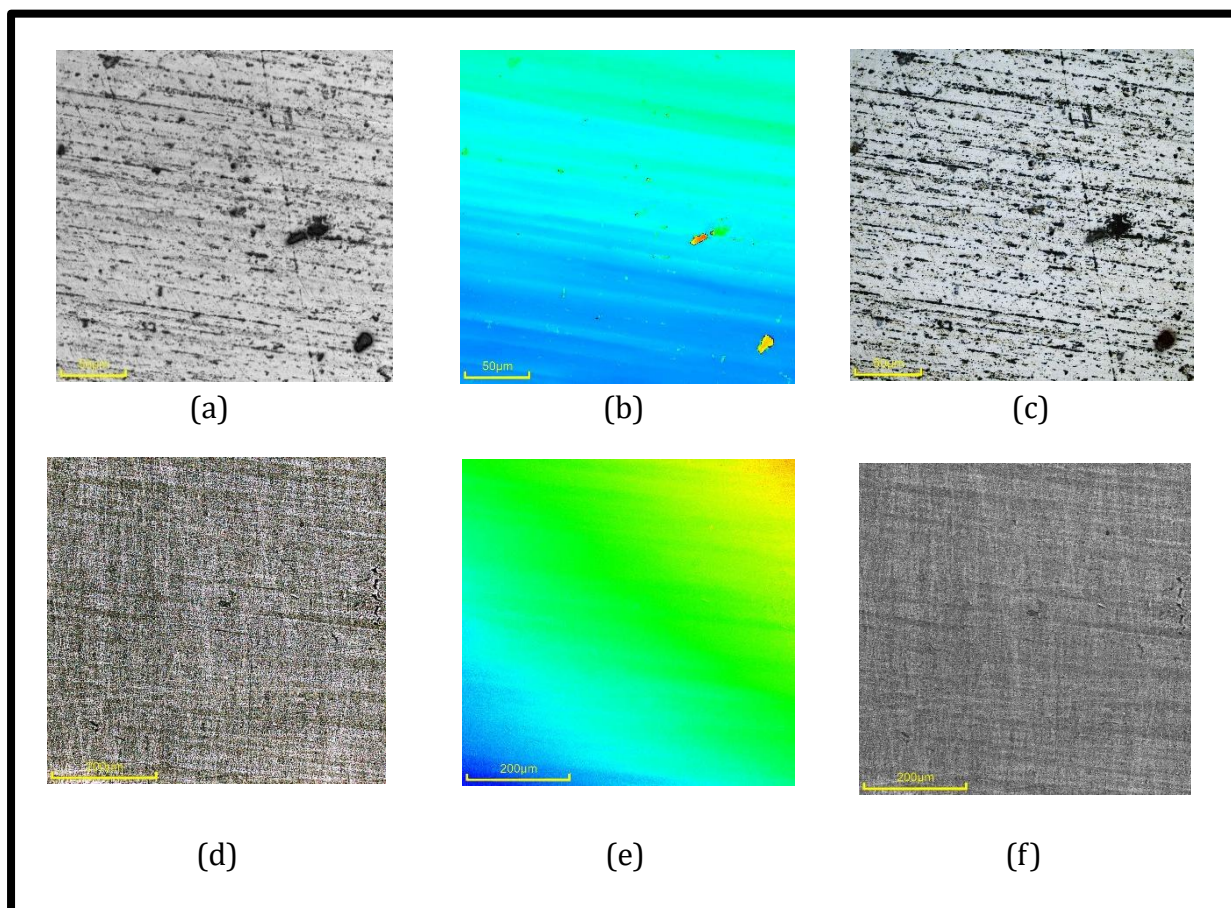


Figure 26 Laser images that characterise the surface of a molybdenum substrate from pristine molybdenum to seeded molybdenum where (a) is the surface coverage of pristine Mo, (b) is the height profile of pristine Mo, (c) is a pristine Mo surface coverage, (d) is the surface coverage of seeded Mo, (e) is a height profile of seeded Mo and (f) is of the surface coverage of seeded Mo.

3.2 Scanning Electron Microscopy (SEM)

There are many different diamond surface morphologies for a range of applications such as natural and synthetic diamond, single crystal diamond (SCD), polycrystalline diamond (PCD) etc. SEM analysis of the NDD samples grown on molybdenum was used to characterise the surface. Both the highly nitrogen-doped diamond (HNDD) samples formed NCD surfaces via CVD, which is represented by figures 27 and 28. NCD typically have grainsizes of 10-100 nm with a high density of nucleation.⁷² The larger the grain boundary size is an indication to the growth of higher quality diamond.⁷³

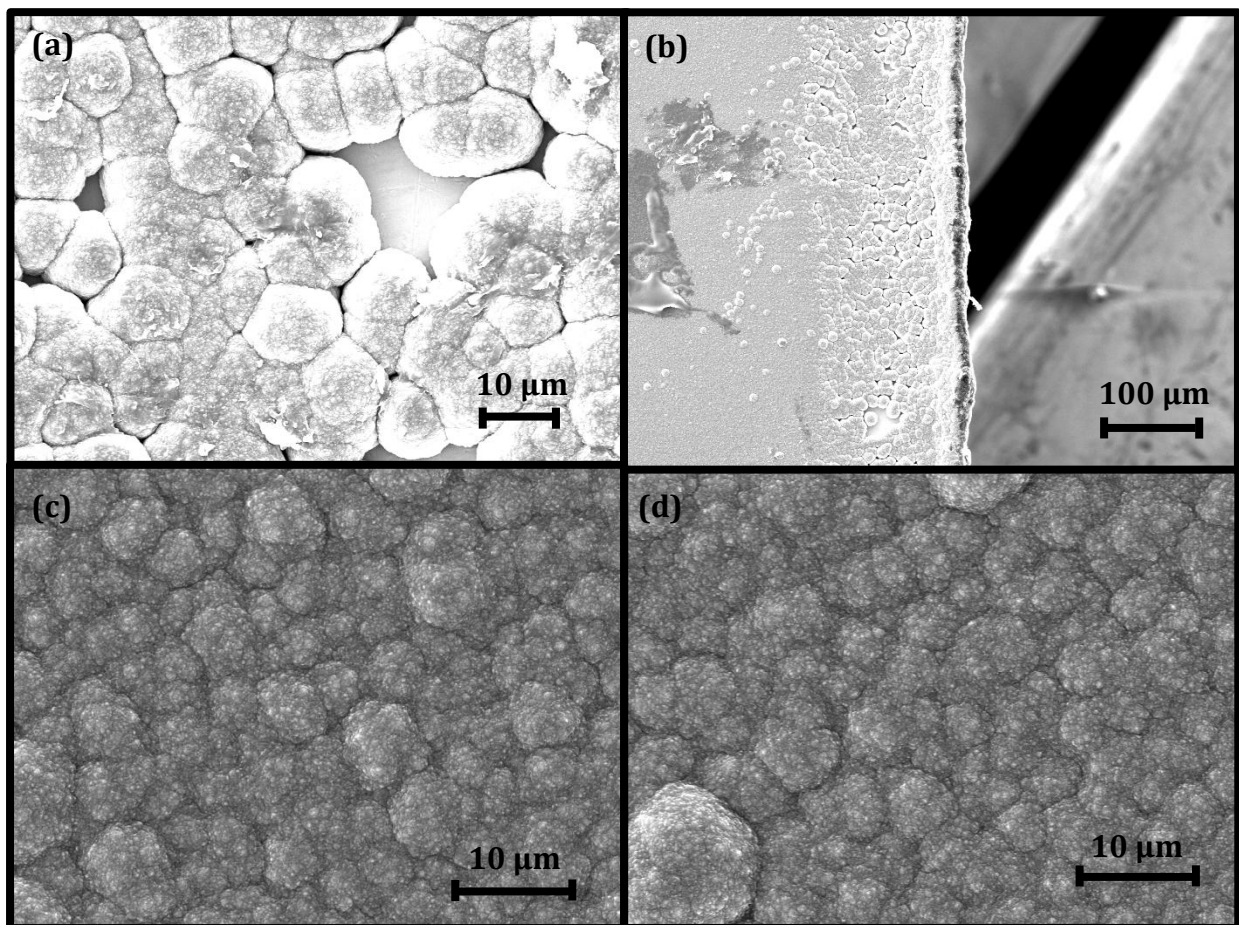


Figure 27 Representing SEM images of HNDD that was grown for 2 hours, Mo1, see table 6 of the appendix. Each image is representing (a) an edge zoomed in, (b) an edge zoomed out, (c) the surface morphology and (d) the surface morphology again.

The 2 hour grown sample show incomplete growth, particularly at the edges in figure 27. Therefore, to growth high quality NDD thin film on molybdenum, growth times of 2 hours must be exceeded. Ideal growth is represented in figure 28 of a 4 hour grown sample. The

protrusions of diamond at the edges of this sample occurred due to nanodiamond residue having built up during manual abrasion.

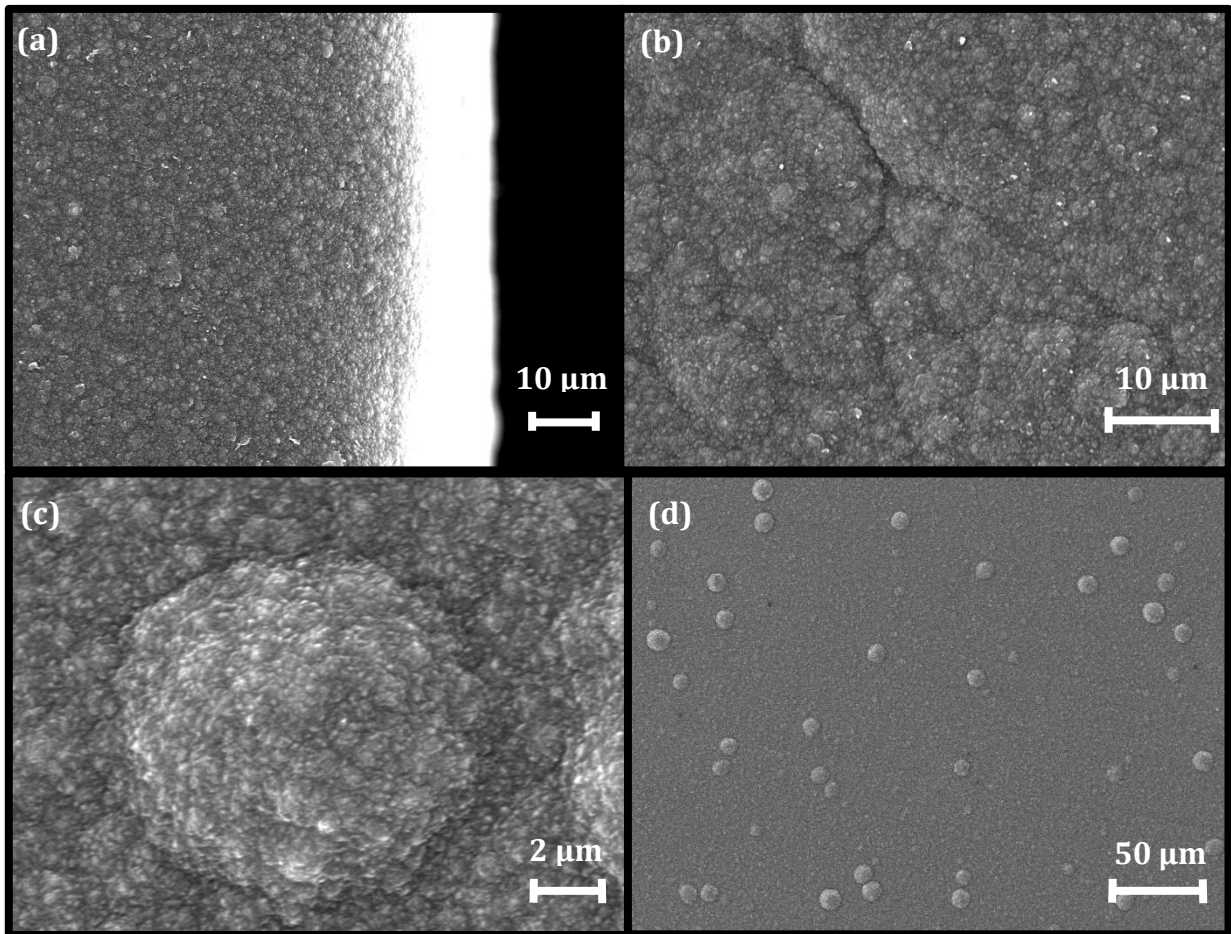


Figure 28 SEM images of Mo₂, a HNDD that was grown for 4 hours: (a) build up at the edge of the sample, (b) the textured nano surface of nitrogen doped diamond, (c) a built up feature and (d) the zoomed out surface morphology.

Both the samples in figures 27 and 28 were found to have an average grain size ranging between ~ 3 to $10 \mu\text{m}$, with generally smooth, rounded and uniform growth. The HNDD 4 hour Mo₂ sample was the most promising surface for thermionic emission applications as it had the largest grain boundaries of all the samples and so was least affected by the occurrence of electron scattering. Ideally, no grain boundaries or defects would be present on the surface of the diamond to avoid this completely. Typically, NCD should not form cauliflower-like structures; however, this was not the case for the samples in figures 27 and 28. The formation of these cauliflower-like structures could be due to the high concentration of CH₄ or a reduction in atomic H₂ which increased the rate of re-nucleation during the MWCVD process.⁷²

The low nitrogen doped diamond (LNDD) samples, Mo3 and Mo4, see table 6 of the appendix, were found to have an average grain size ranging between 1 to 2 μm , making them microcrystalline diamond (MCD) thin films which have typical grain sizes of 2-5 μm in size.⁷² The surface morphology was rougher and more defined in comparison to their HNDD counterparts. The smaller grain boundary size suggests that the surface is more affected by the presence of electron scattering. The surface morphology of the LNDD were more defined with sharper protrusions representing the grain boundaries.

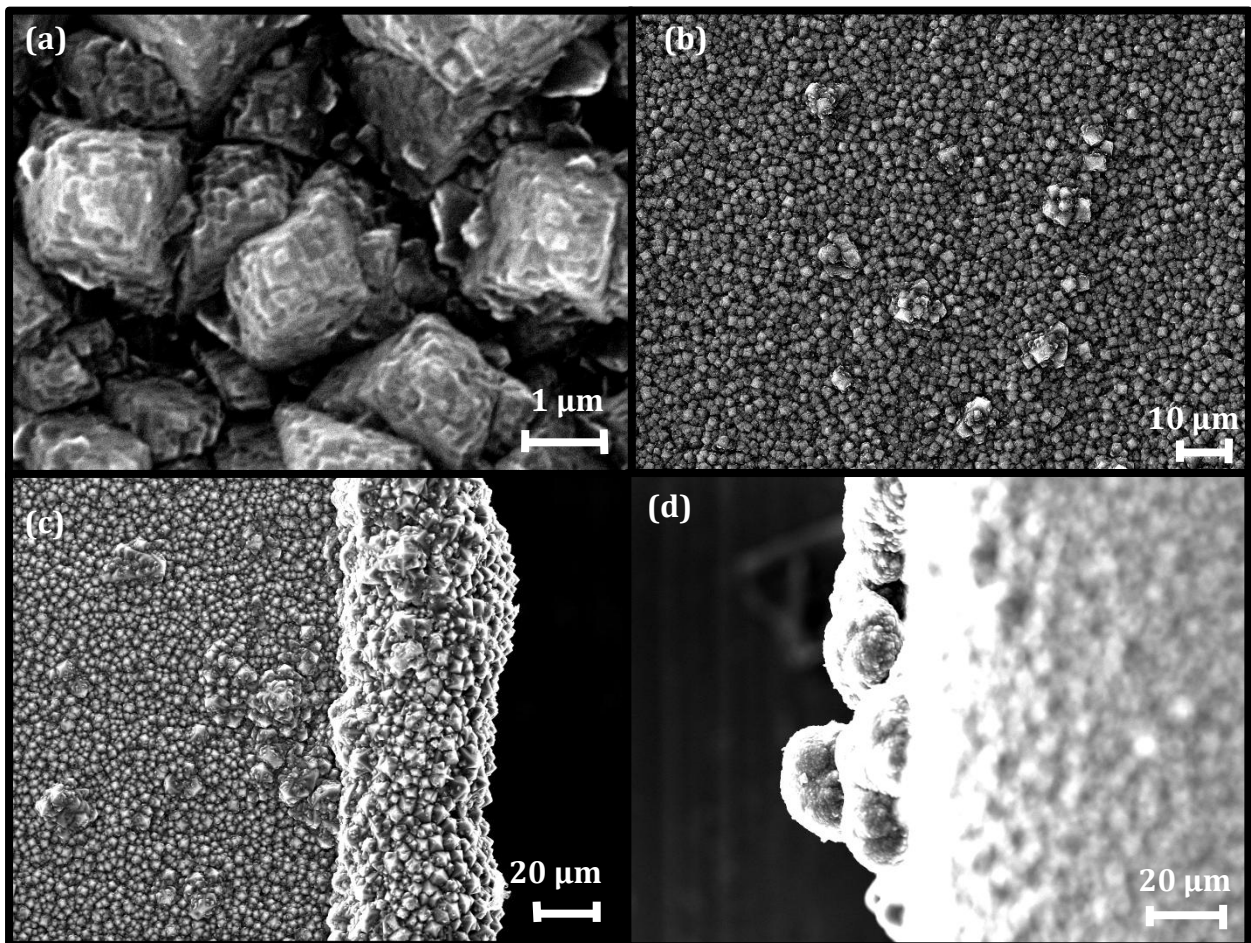


Figure 29 SEM images that characterise LNDD samples where (a) and (c) are the 2 hour grown Mo3 sample and (b) and (d) are 4 hour grown Mo4 diamond sample. (a) to (b) show the general surface morphology, (c) and (d) represent build-up of LNDD at the edges of the sample.

In figure 29, the diamond, which was originally expected to be NCD has formed MCD and this could be due to the growth of grain size being proportional to the thickness of film increasing. Therefore, for NCD and MCD, as the thickness of the thin film increases, the surface morphology gets rougher and the number of facets increase.⁷² NCD is more

desirable as it produces better quality diamond thin film with greater nucleation densities of $> 10^{11} \text{ cm}^{-2}$. Moreover, grain sizes $< 5 \text{ nm}$ are difficult to develop as there is more disturbance to the packaging arrangement.⁷³

3.22 Raman Spectroscopy Characterisation

The NDD samples were then characterised by Raman spectroscopy. First, the Raman spectrometer was calibrated to the Raman peak indicative of pure SCD at 1332 cm^{-1} , as seen in figure 30.

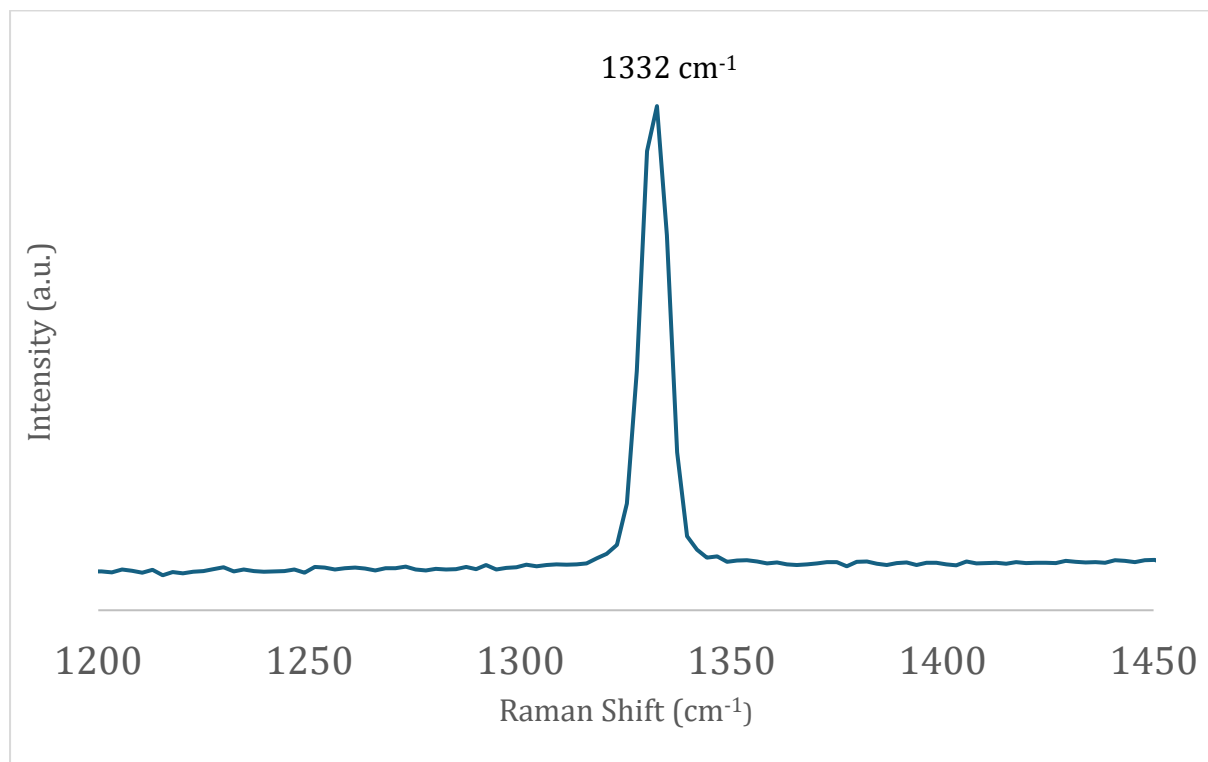


Figure 30 Raman spectroscopy calibration curve representing the Raman shift of pure SCD at 1332 cm^{-1} .

Based upon comparison to literature, the HNDD sample distinctively showed characteristics of nanocrystalline NDD with the four common peaks. The peak present in the calibration curve of figure 30, 31 and 33 is at a Raman shift of 1332 cm^{-1} and characterises the sp^3 hybridised surface of diamond.

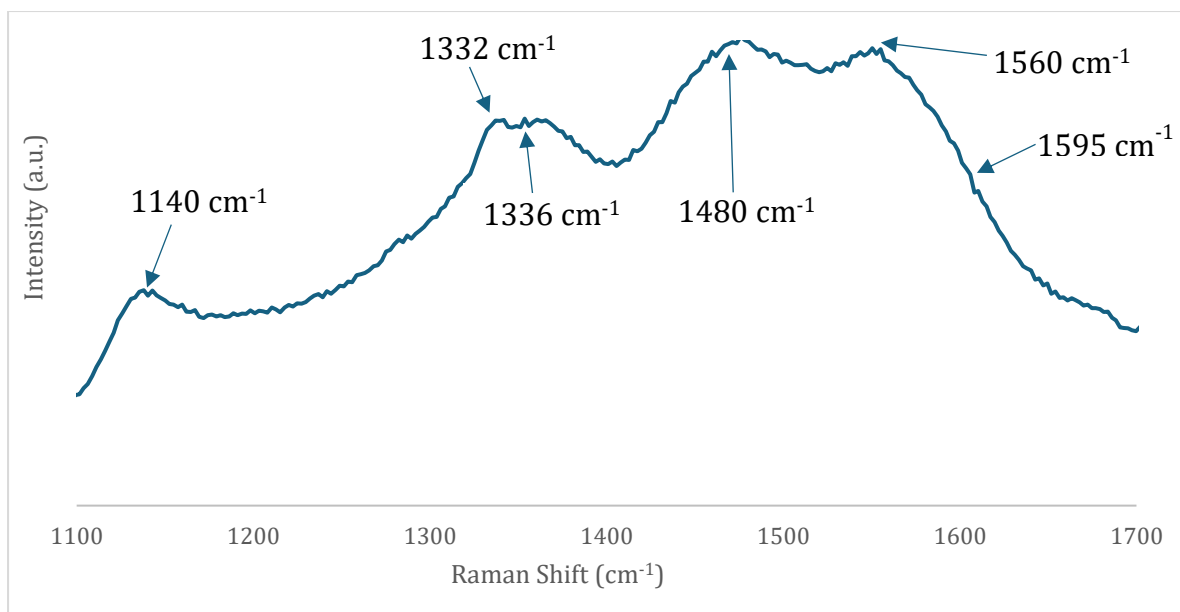


Figure 31 Raman spectrum of HNDD, Mo1 sample.

Figure 31 is representative of a typical Raman spectrum for nanocrystalline NDD, with five main Raman features found at 1140 cm⁻¹, 1336 cm⁻¹, 1365 cm⁻¹, 1480 cm⁻¹ and 1560 cm⁻¹. There is a distinctive peak at 1595 cm⁻¹ in figure 31, as well as less prominently in figure 33 which is indicative of the *sp*² hybridization of NDD. It can be inferred that the HNDD peak is more prominent as it lead to an increase in *sp*² hybridization due to the formation of defects and surface graphitization. There is a slight peak in figure 31 at 1365 cm⁻¹ which is also indicative of surface graphitization, defects and disordered carbon.⁷⁴

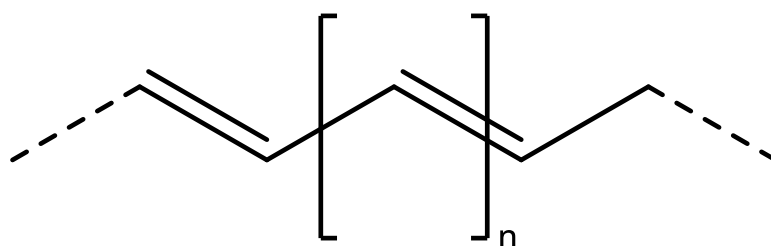


Figure 32 The structure of trans-polyacetylene.

In figure 31 and 33, a Raman shift at 1480 cm⁻¹ characterised the formation of *trans*-polyacetylene which is more defined in figure 31, for the HNDD sample. There is a defined peak in figure 31 at a Raman shift at 1145 cm⁻¹ which is also indicative of *trans*-polyacetylene phases on the surface of diamond that are located at the grain boundaries.⁷⁴

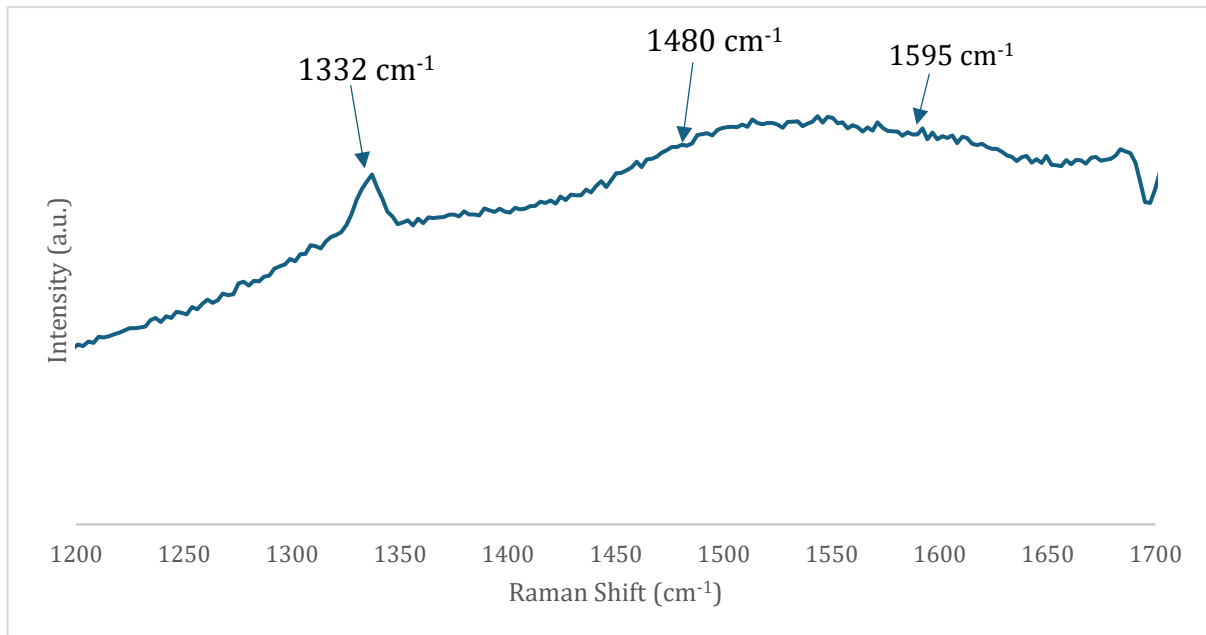


Figure 33 Representing the Raman spectrum of LNDD grown on molybdenum for 4 hours.

3.3 Thermionic Emission Data of a Hydrogen Terminated Surface

Initially, a hydrogen termination was performed on the LNDD Mo4 sample, and the thermionic emission of the surface was measured for three cycles, see figure 34. The cycle 1, represents the activation cycle. As the sample is heated, the electrons gain enough energy and the ability to emit off the surface in an a high vacuum system. This is representing the NEA surface. A maximum current of 8.35×10^{-7} mA was achieved in the cycle 2, which also demonstrated the most stable emission of all the cycles. For cycle 3, we see deactivation of the diamond thin film. Deactivation occurs as hydrogen atoms desorb over time at temperatures >500 °C and so there is a depletion in emission current efficiency. If further cycles were run, a continuous depletion in emission current would be expected until all the H atoms have been desorbed and only a PEA surface remained which would show no emission peaks. This data proved that a diamond surface with the potential to produce NEA has successfully been grown on the LNDD sample, Mo4. Due to technological restraints the HNDD Mo1, Mo2 or Mo5 samples did not demonstrate NEA, despite having been hydrogen terminated and tested, which is discussed in section 3.6.

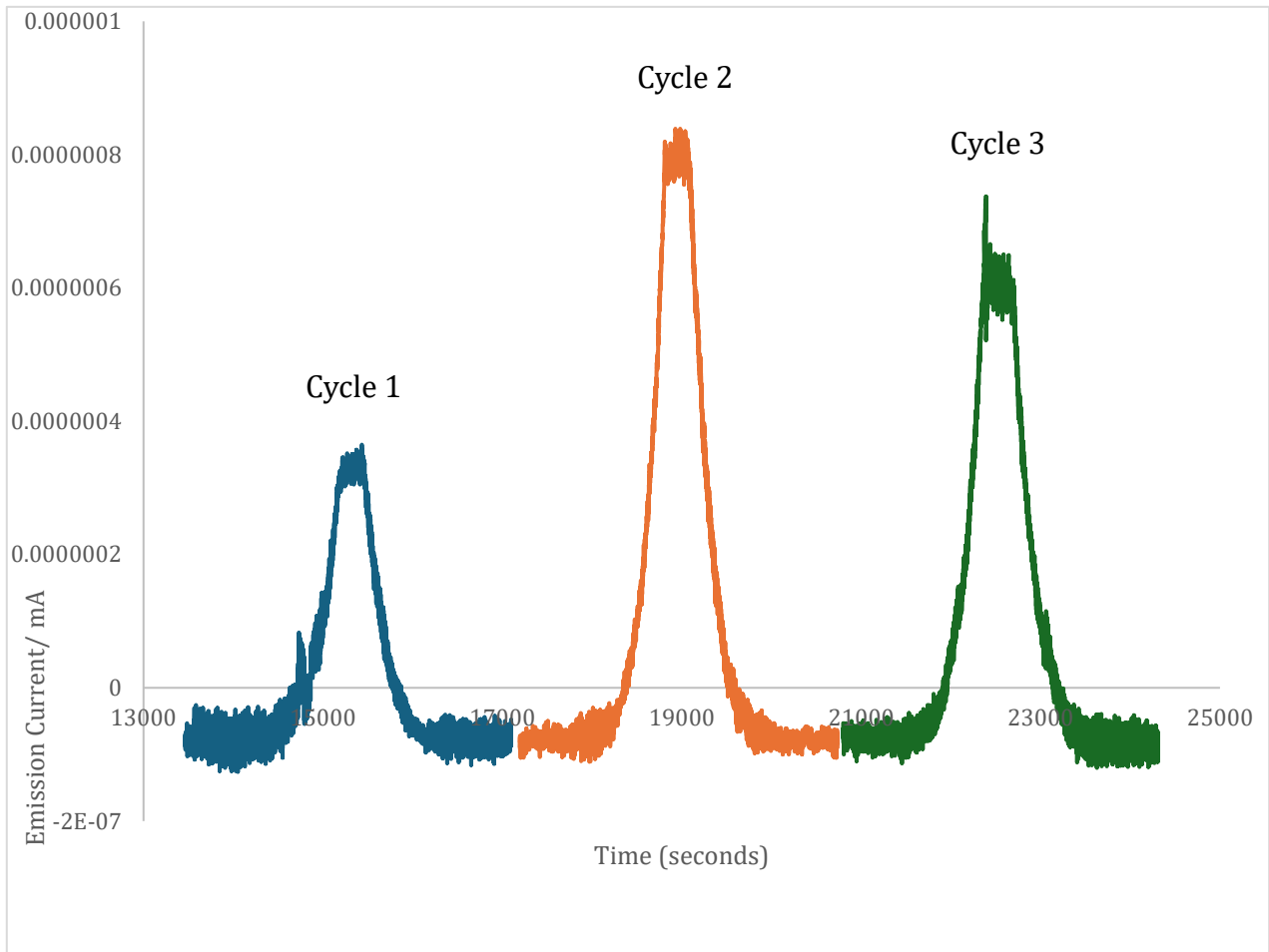


Figure 34 Thermionic emission data from LNDD Mo4 sample, where cycle 1 is the activation cycle, cycle 2 demonstrates the highest stable emission of 8.35×10^{-7} mA and the cycle 3 represents the deactivation cycle.

3.31 Thermionic Emission Data from a ScO-terminated Surface

Thermionic testing was conducted on a ScO-terminated Mo4 sample. The sample was highly unstable and in the time taken for transport and mounting, the surface had become damaged and much of the ScO-termination was lost. Two cycles were performed on the sample that demonstrated some NEA through thermionic emission current. An initial run of the sample through a cycle demonstrated a maximum emission peak at 3.06×10^{-7} mA at 300 °C. However, this was not a stable emission which is clear from the data represented in figure 35, as there was no further current emission beyond this point. The same is true for the second test of the sample, represented by figure 36, where a higher unstable emission current was exhibited at a value of 6.00×10^{-7} mA. Mo5 was also tested; however, no emission was seen due to the desorption of the ScO-terminated surface as a

result of prolonged air exposure during sample transportation from the NanoESCA facility and mounting into the TECsim.

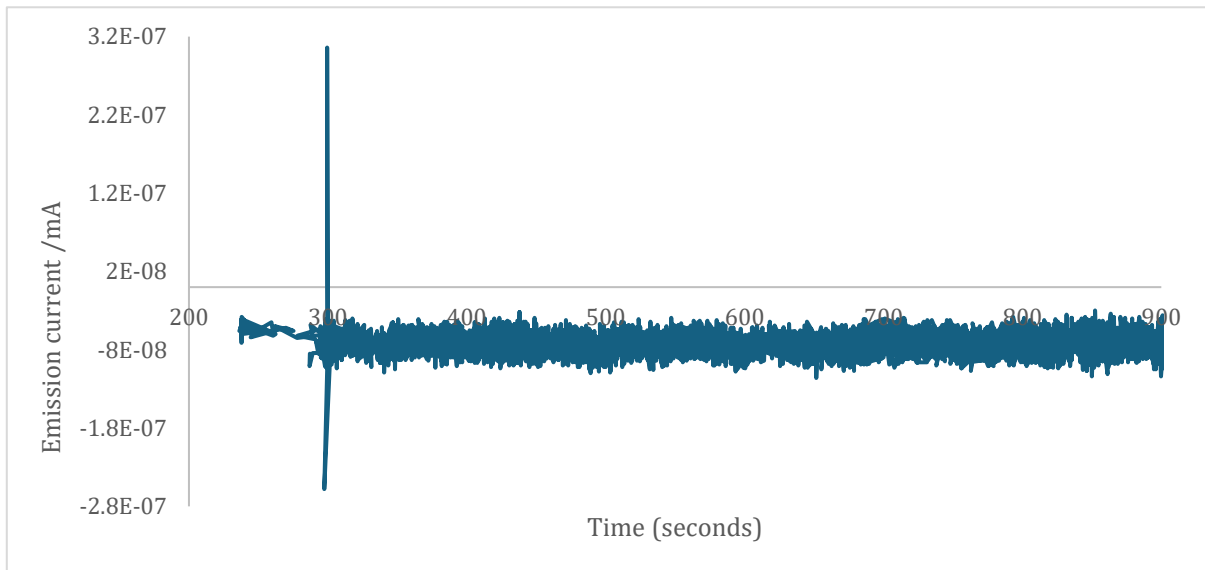


Figure 35 Unstable thermionic testing data of an ScO-terminated surface on Mo4 in the initial stages of testing with a emission current jump of 3.06×10^{-7} mA at 300 °C.

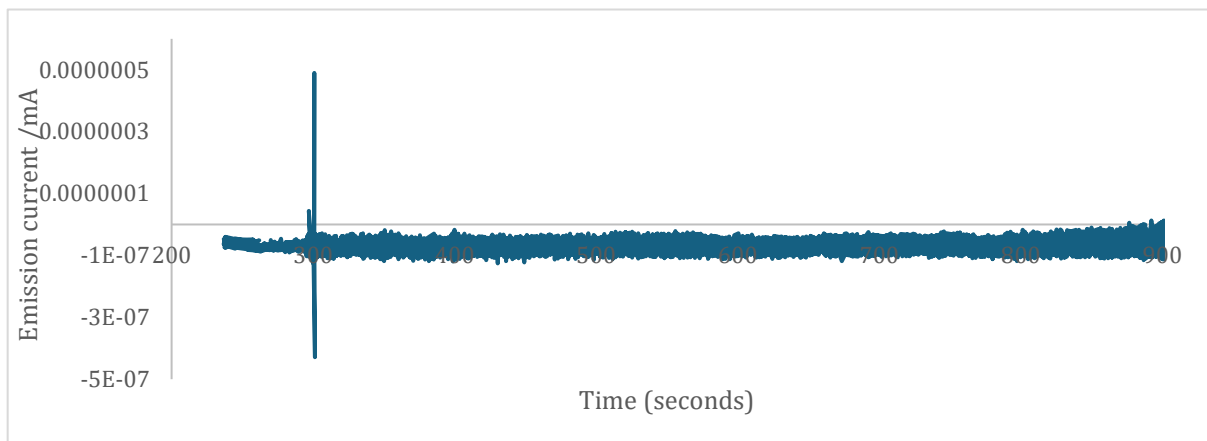


Figure 36 Unstable thermionic testing data of an ScO-terminated surface on Mo4 in the second stages of testing that exhibited a emission current peak at 6.00×10^{-7} mA at 300 °C.

This data did not show the expected current emission cycle that would have been similar to the hydrogen terminated results in figure 34. Improvements that could have been made were to optimize the etching of the back-side of the sample, reduce the time it took to mount the sample and in turn, its exposure to air and improvements on the transportation of the sample from the NanoESCA facility to the School of Chemistry.

3.4 X-ray Photon Spectroscopy (XPS) Characterisation

XPS analysis is a characterisation technique that aids in identifying the elemental and chemical state of a sample through the photoelectric effect that evaluates core level binding energies (BE). A measure of the kinetic energy (KE) of electrons that have been emitted from the surface following photoexcitation by X-rays is taken. The BE provides information on the density of charge of atoms in the system.⁷⁵ XPS analysis was performed on Mo5 that had been ScO-terminated. Based on literature, the energy of the carbon and oxygen 1s electrons are characterised in figure 37 at 285.68 and 532.18 eV, respectively. This is characteristic of the initial oxygen-terminated surface before scandium deposition.⁷⁶

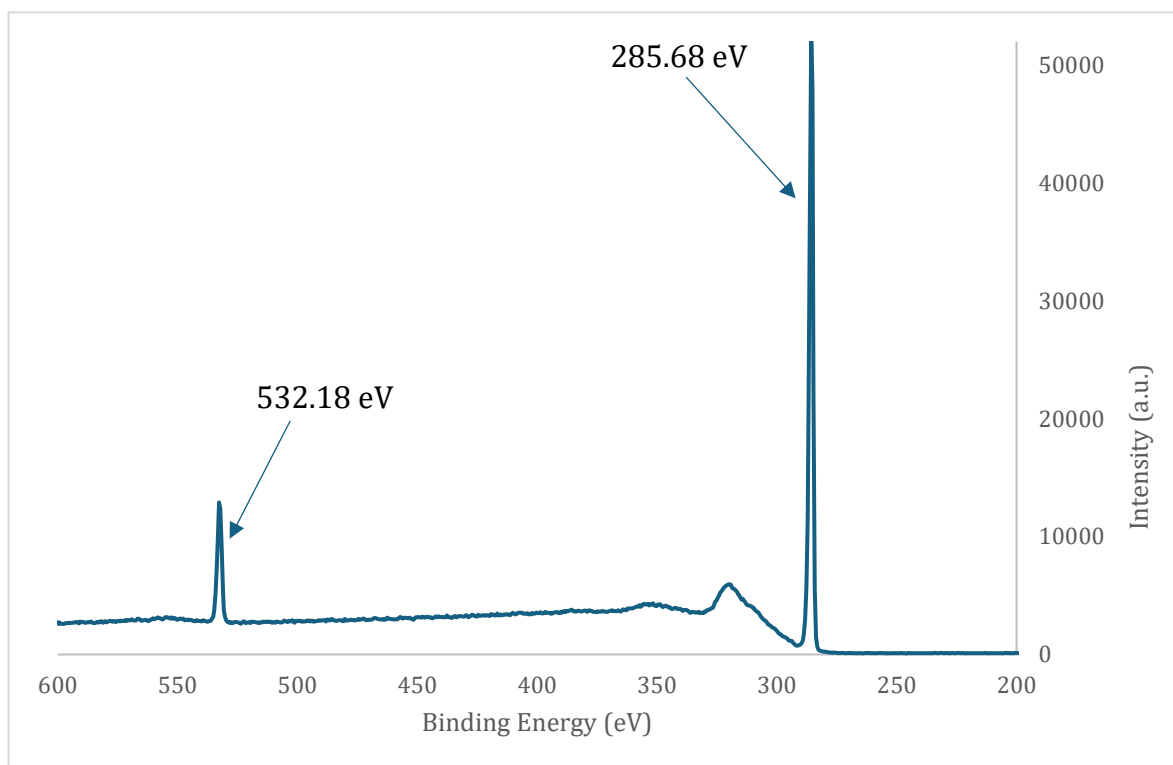


Figure 37 A survey of the initial XPS results of Mo5.

The peak at 285.68 eV in figure 37 is characteristic of the sp^3 hybridized carbon at the surface of the diamond thin film. The peak at 532.18 eV reflects the C_d-O-C_d formation as a result of oxygen termination. This is highlighted further by figure 38 that represents the binding energy against intensity peak of the oxygen-terminated diamond surface at 532.72 eV.⁴⁰ Based on literature, sp^3 hybridized carbon has a binding energy of 285.00 eV with variations of up to ~ 1 eV for C (1s) due to exposure to nitrogen plasma. This variation is caused by band bending due to the presence of nitrogen in the lattice. Moreover, there is a greater proportion of C=C and a decreased amount of C-C, and it can be inferred that

this is as a result of nitrogen doping increasing the percentage of *trans*-polyacetylene at the grain boundaries of the diamond thin film surface.⁷⁷

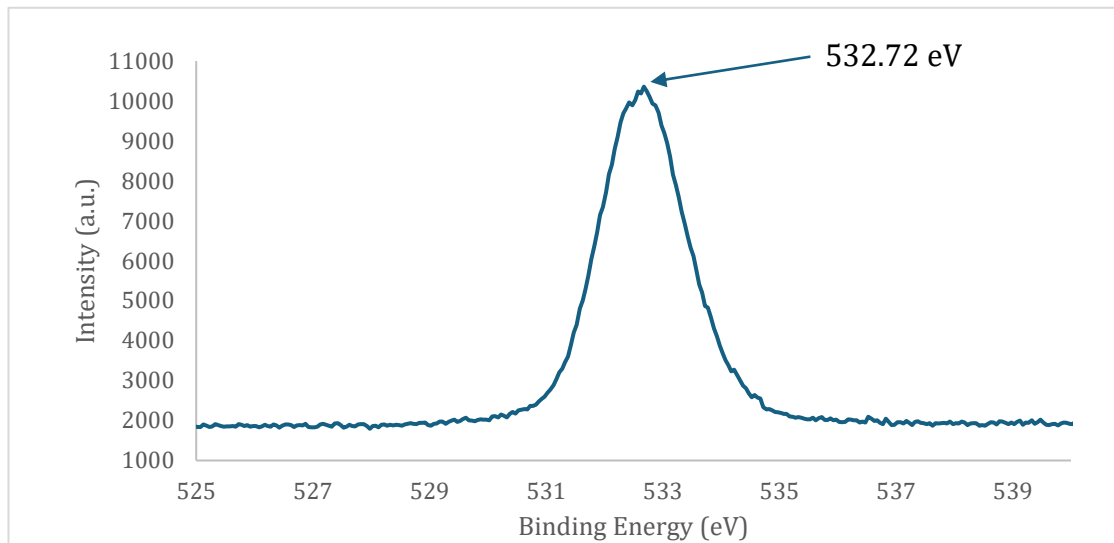


Figure 38 Representing the C(1s) core level spectrum of a O-terminated Mo5 surface after annealing at 300 °C for 1 hour.

Post scandium deposition of a 0.25 ML for 4.5 minutes at room temperature and annealing at 700 °C, XPS survey analysis was completed on the sample to understand the surface composition further, see figure 39 , 40 and 41. Post scandium deposition the O-terminated surface was limited, see figure 39 and 40.

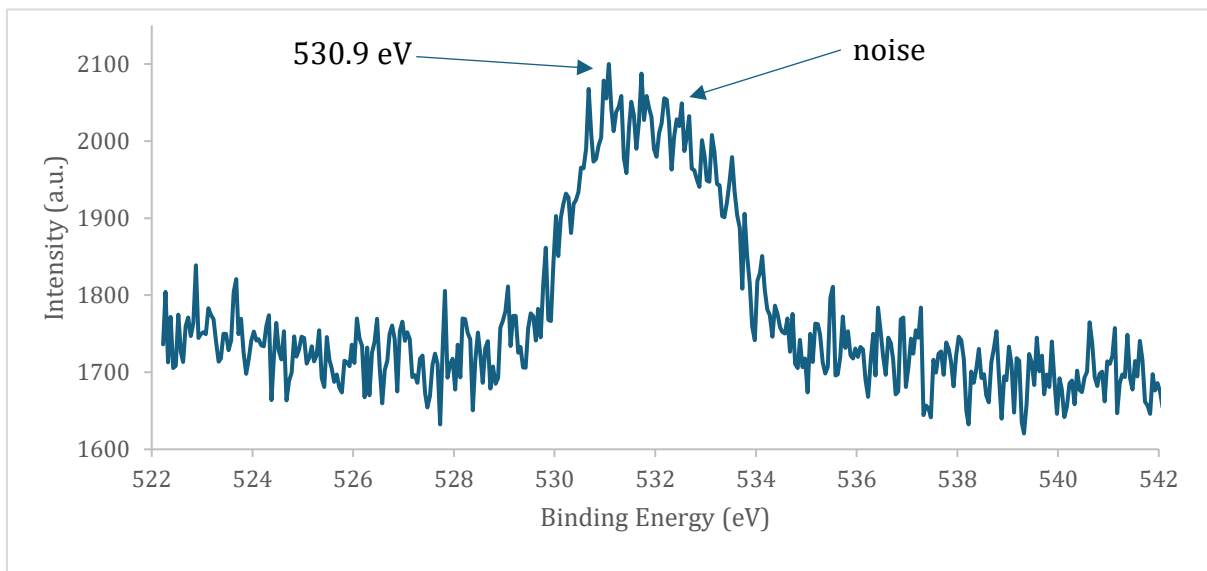


Figure 39 Representing XPS analysis of oxygen binding energy after scandium deposition on Mo5.

Figure 39 shows analysis for the O- termination post scandium deposition, where the oxygen binding energy has a slight downshifted to a peak at ~530.9 eV in comparison to its binding energy based on literature and figure 38, at ~532 eV and 532.72 eV, respectively.⁷⁸ There is slight noise in figure 39 at 531.1, 532.4 and 532.9 eV that corresponds to Cd=O, Cd-OH and Cd-O-Cd, respectively as a result of oxygen termination via O-cracking.

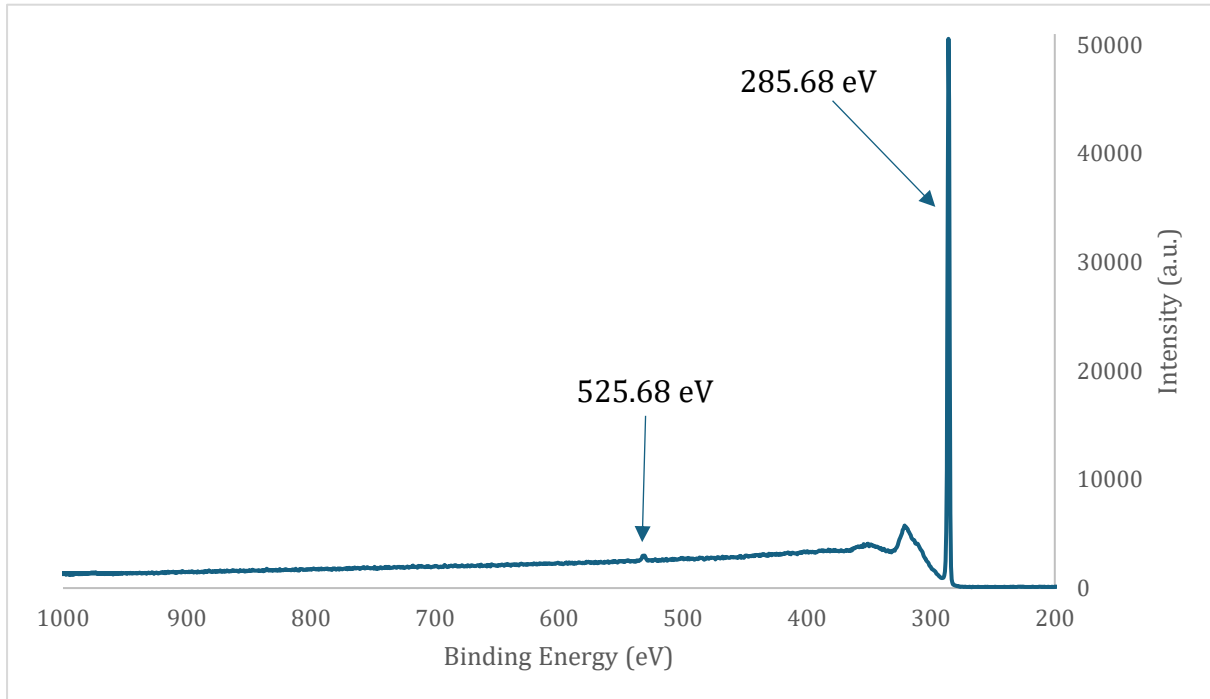


Figure 40 Representing an XPS survey analysis of the sample post scandium deposition on Mo5.

The peaks specifically for scandium deposition were also characterised by XPS analysis. Figure 40 is not clear of the characteristic peaks that are indicative of scandium having been deposited onto the O-terminated surface. In figure 41, the peak at 401.87 eV represents the scandium $2p^{3/2}$ electrons and the peak at 406.18 eV represents the scandium $2p^{1/2}$ electrons, and so the successful deposition of scandium following annealing at 700 °C is confirmed. It can be inferred that the surface is more Sc- terminated than ScO- terminated as the tiny O-terminated peak at 525.68 eV in figure 40, that has downshifted as a result of Sc deposition, is barely visible. For future work, annealing the sample at a lower temperature of 500 °C post scandium deposition should be explored as it is understood that for the Mo5 sample, annealing post deposition at 700 °C resulted in the desorption of oxygen from the surface.⁴⁰

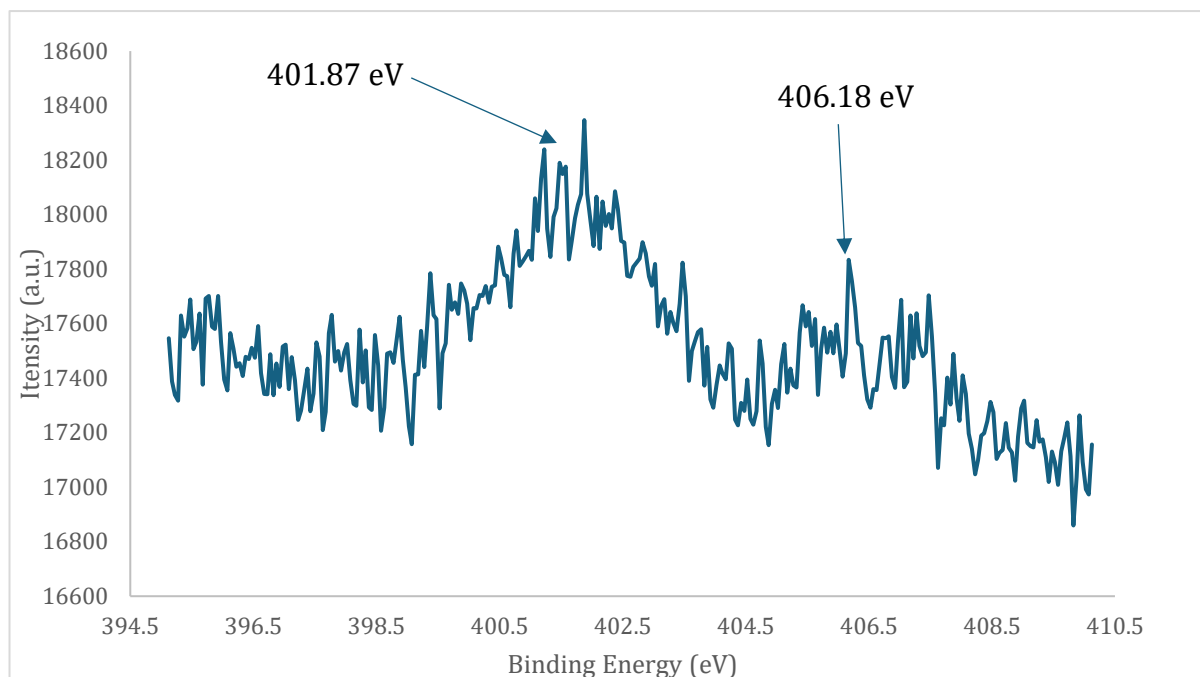


Figure 41 The binding energy to characterise scandium deposition via XPS analysis on Mo5.

3.5 Ultraviolet Photoelectron Spectroscopy (UPS) Characterisation

UPS analysis reveals the energy distribution of photoelectrons, which have small kinetic energies when they are emitted from the surface following the absorption of ultraviolet light.⁷⁹ Therefore, the electronic structural analysis of the 0.25 ML ScO-terminated HNDD Mo5 nanocrystalline surface was characterised. The full scale spectrum is depicted in figure 42. The spectrum was then magnified to depict the cut-off energy region, valence band maximum relative to the Fermi energy and the “knee” of the spectrum, which are shown in figures 43, 44 and 45. Upon annealing at 700 °C, a work function value of 3.6 eV was calculated alongside a NEA of -1.545 eV.

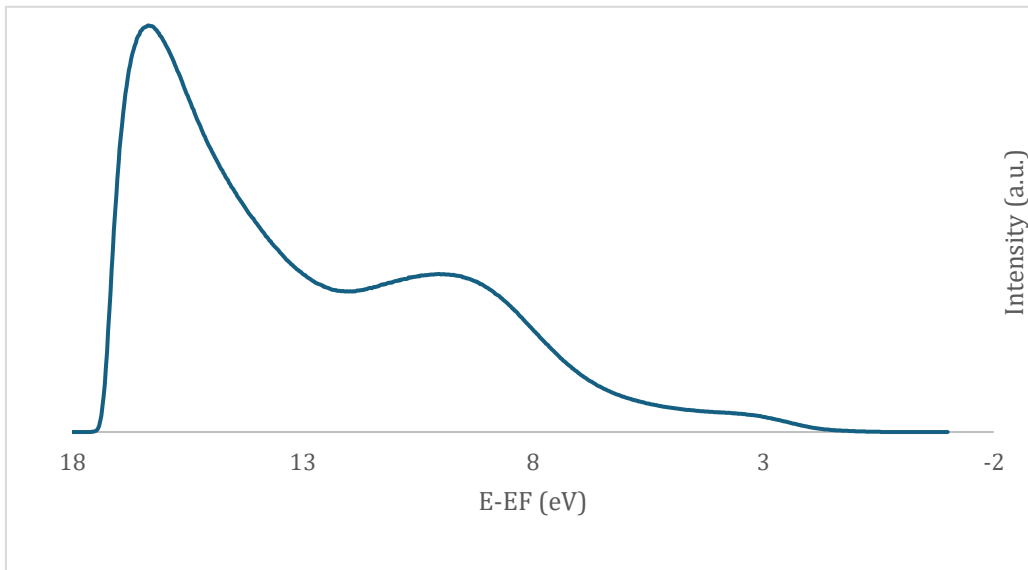


Figure 42 Ultraviolet photoelectron full scale spectrum of Mo5.

The “knee” of the curve is magnified in figure 43 and shows a binding energy of 9.9 eV. This is the lowest energy required for the formation of an electron-hole paring. Consequently, in terms of electronic structural analysis, the loss of energy during the transition from electron pair formation to phonon-electron scattering is depicted.

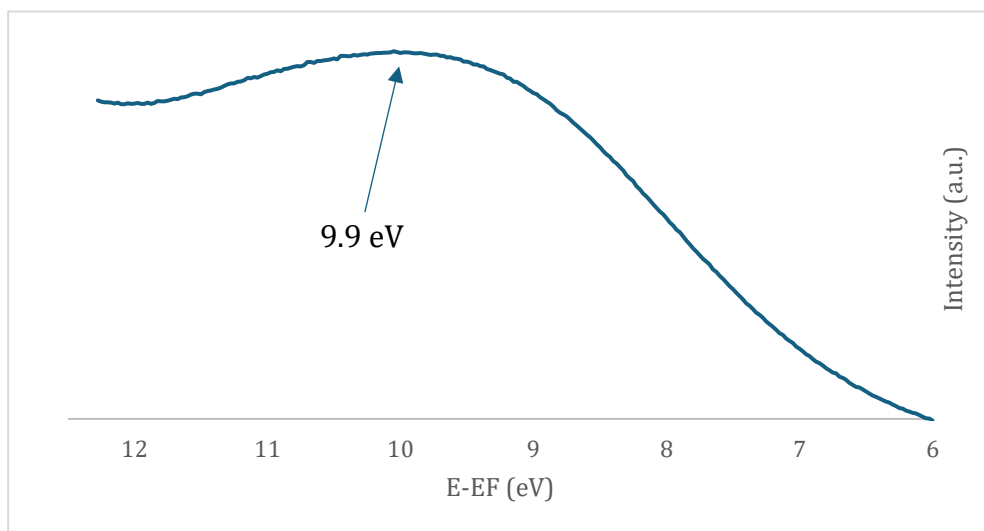


Figure 43 The “knee” of the curve at 9.9 eV.

Through linear extrapolation depicted in figure 44, the VBM was calculated relative to the Fermi level, which was set to zero. The CBM was calculated via equation [1]:

$$E_{CBM} - E_F = h\nu - (E_F - E_{VBM}) - E_g \quad [1]$$

, $h\nu$ is the UV excitation energy of 21.2 eV and a bandgap (E_g) of 5.47 eV.

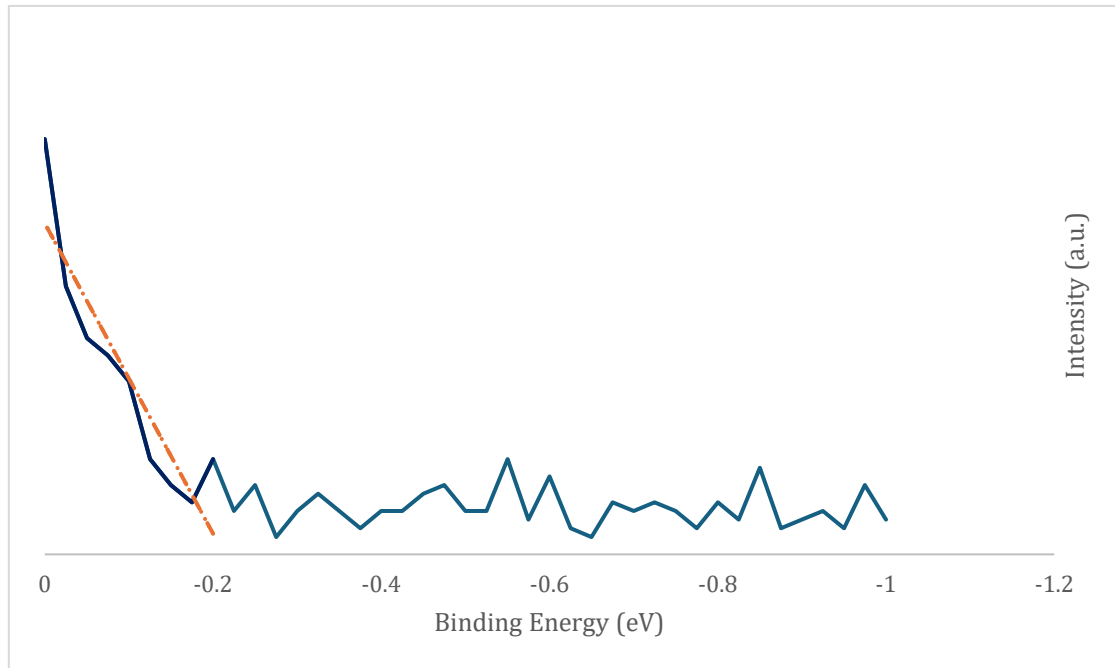


Figure 44 The valence band maximum relative to the Fermi level at -0.275 eV. The dashed line shows the linear extrapolation of the curve which is the VBM relative to the Fermi level.

Consequently, the work function was calculated as the difference between the UV excitation energy of the He(I) photon source and the cut off energy of 17.5 eV, see figure 45. This was calculated to be 3.6 eV and by using equation [2], these values were used to calculate the electron affinity:

$$\chi = \phi + (E_F - E_{VBM}) - E_g \quad [2]$$

, with a resulting value of -1.545 eV. This was not as negative as originally expected, which is discussed in sections 3.61 and 4.1.

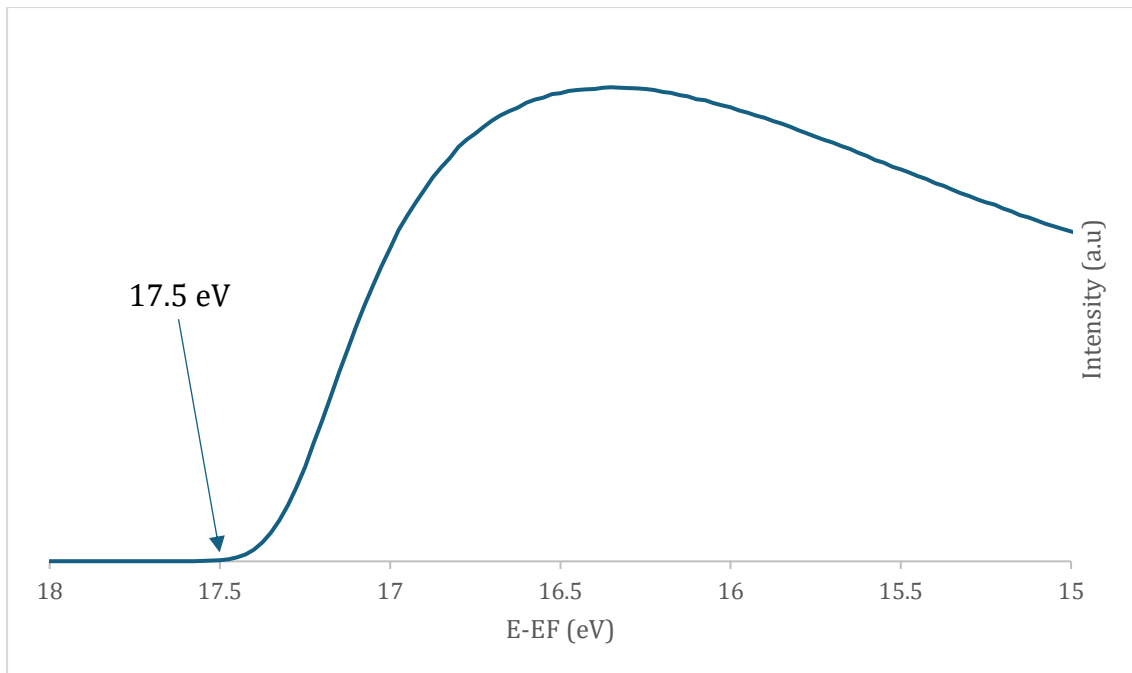


Figure 45 The “cut-off” energy at 17.5 eV.

3.6 Failures and Scientific Limitations

There are a range of factors to consider resulting in scientific limitations to the progress and success of this project. This includes the incompatible grating of molybdenum due to the replacement with a more powerful CO₂ laser in the micromachining system. Further studies of the grating must be completed to optimise a well-defined and uniform backside etching so that it is compatible with the thermionic testing kit and produce a stable PID that leads to stable thermionic emission. Moreover, delamination of the diamond thin film surface during MWCVD growth resulted in difficulties with sample fabrication. Finally, there were various technological restrictions that resulted in prolonging of progress throughout the project as well as irreplaceable damage to samples, all of which are detailed in this section for failures and scientific limitations.

3.61 Incompatible Grating of Molybdenum

Due to unoptimized grating for SPP as the Oxford laser micromachining system was replaced with a more powerful laser, the PID was unable to stabilize above temperatures of >500 °C. Despite the grating periods being well structured, at the high laser power of 70%, the surface of the grating patterns were not uniform and had many abrasions. This resulted in an increase of absorption as a result of light scattering and in turn, inadequate compatibility for thermionic emission, see figure 46 representing the difference between

the laser power at a period of $10.5\ \mu\text{m}$ and the effect it had on surface uniformity.⁸⁰ A laser power of 90% was tested on Mo₂ which then had to be remade due to irreparable damage the laser caused to the backside of the sample during the grating process. The laser burnt off ~half of the molybdenum substrate in line with the grating pattern which lead to a stepped edge in the middle of the sample. This stepped difference in the sample surface meant that the temperature control was highly inaccurate and the PID was impossible to stabilize. The thermal inertia of the thinner side of the substrate was much lower than the thicker side. This meant that there were discrepancies in the absorbance and heat energy transfer due to heating via laser power of the thermionic testing kit, despite the laser grating modification process having been performed on the back surface of the sample. Not only does grating produce an ideal surface for SPP, it also reduces the reflectance of the surface leading to increased optical absorbance.⁷

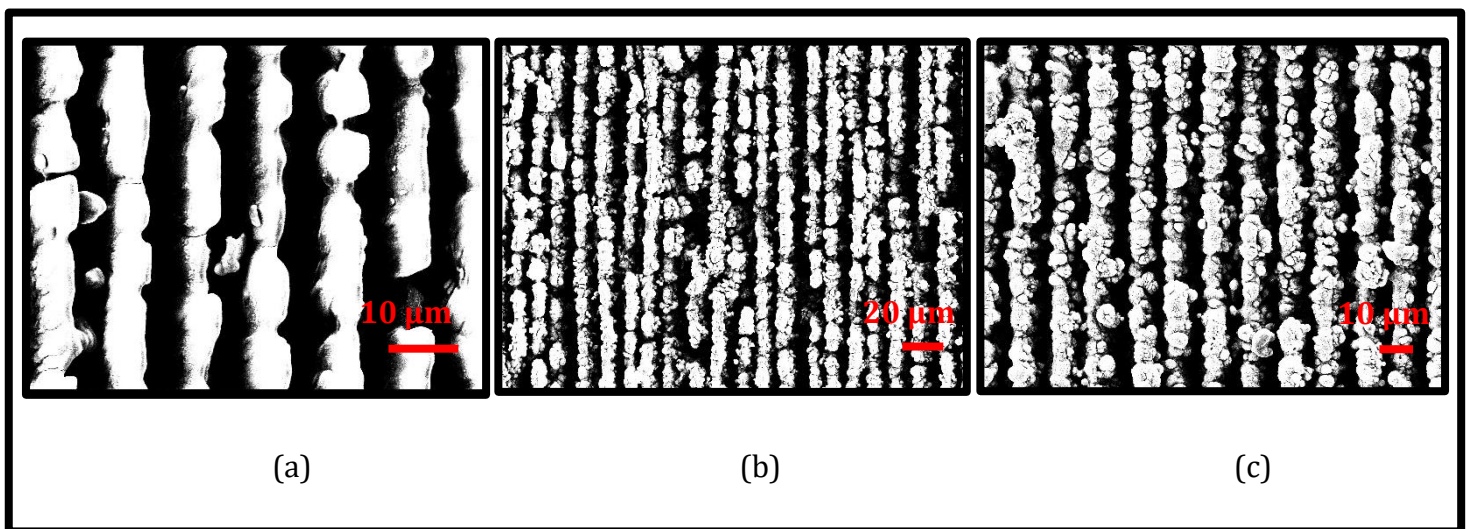


Figure 46 SEM images representing the linear backside grating of a period of $10.5\ \mu\text{m}$ at (a) 30% laser power which is relatively uniform, (b) 50% laser power that is increasingly unstructured and (c) at 70% laser power which is highly irregular, created by Dr. Ramiz Zulkharnay.

The plasmonic heating effect is desirable for solar energy applications because it has the potential to improve existing technology by reducing thermal resistance >50%. For example, it has been proven to increase water heating effectiveness of a solar technology system by >25%, so optimising grating for SPP with the new CO₂ laser system and exploring its compatibility with NCD is still of high interest due to its potential.⁸¹ High quality NCD and MCD thin films grown on molybdenum can easily excite SPP at a wavelength of $\sim 1.55\ \mu\text{m}$ without requiring any chemical changes via doping or physical manipulation via voltage tuning.⁸²

3.62 Delamination of the Diamond Thin Film

Unfortunately, many MWCVD-grown diamond samples over the progression of this project unexpectedly delaminated in various ways. Delamination resulting from poor manual abrasion may have occurred as the molybdenum surface was too delicate or damaged resulting in poor nucleation density.⁸³ Furthermore, if significant damage to the surface occurred during the abrasion process, this could have been a factor in delamination and inadequate growth during MWCVD.⁷⁴

Graphitization of carbon is a substantial factor in the growth of NDD. It is characteristic of C=C formation of the diamond surface and an increase in sp^2 hybridisation.⁶⁴ This in turn decreases the nucleation density, creating rougher diamond thin films that are less strongly adsorbed onto the substrate.⁷⁴ Residual stress and the thermal expansion coefficient have an integral part to play on surface adhesion. Delamination may have occurred during MWCVD due to differences in the expansion and relaxation between the diamond thin film and molybdenum substrate during the cooling of the sample to room temperature following growth.⁶⁴ There were more difficulties with the LNDD samples in figure 29 representing MCD, this is due to MCD having greater thermal and residual stress due to having smaller grain boundaries. Therefore, more delamination occurred on the MCD samples during growth as the adhesion was weaker.⁶⁴

During the acid wash post SEM, the Mo3 delaminated. Due to nitrogen being highly electronegative, the strength of bonds between sp^3 C-N and sp^3 N-C is significantly weaker than that of undoped diamond, sp^3 C-C. Consequently, this reduction in bond strength alongside the harsh environment of the acid caused this to occur, whilst also damaging the structural integrity and adhesion of the remaining 3 samples.⁸⁴ However, generally as C-N bonds are shorter than C-C bonds, introducing nitrogen doping into the system decreases residual stress overall as the structure is more disordered and the carbon system is more relaxed.⁸⁴

Thermionic emission testing required heating and cooling cycles of temperatures of up to 1000°C. During one cycle, Mo1 delaminated, post hydrogen termination. It can be inferred that this occurred due to a thermal mismatch between the diamond thin film and substrate during the cooling down cycle, particularly back down to room temperature. Both Mo1 and Mo3 delaminated easily and so for future work, only >2 hour grown samples should be explored. This is because as growth time increases, so does the thickness of the diamond thin film which in turn decreases the thermal stress.⁸⁵ To avoid this, for both the MWCVD growth and thermionic testing, tuning down the temperature to RT with caution is advised. Moreover, temperatures should not go over a maximum of 1279 °C as this is when a maximum value of deposition is reached at 0.724 GPa alongside the increasing thermal stress.⁸⁵ The thickness of the substrate also affects the residual

and thermal stress. The thicker the substrate, the greater the deformation as there is a prevention of bending which increases the residual stress. Therefore, decreasing the substrate thickness may be a consideration for future work.⁸⁵

Current technology surrounding photovoltaic (PV) cells and harvesting solar radiation in order to generate sustainable energy is one method of mitigating the effects of climate change. However, concerns are growing as a result of a global energy crisis alongside a global desire for carbon footprint reduction.⁸⁶ Utilising cathodes with a low work function in a thermionic solar converter is expected to improve efficiencies of solar energy devices near to the Carnot limit of up to 40%.⁷⁰

Diamond is an electrically dynamic material which results in it being of high interest surrounding electro-chemical technology.⁴ A desirable property that diamond exhibits is NEA which occurs as the vacuum level is found below the CBM, removing the barrier for electron emission from the CB and into vacuum.²² This reduces the temperature required for thermionic emission from 2000 K to 1000 K, which is easier to obtain and control for industrial applications.

A method of enhancing NEA producing significant thermionic emission is through surface termination chemistry, particularly through terminating diamond surfaces with small and highly charged metals such as Mg^{2+} , Al^{3+} , Ti^{4+} and Sc^{3+} . These surfaces are considered to be thermally stable as the ion lies close to the diamond surface and a strong surface dipole forms.⁹ Moreover, depositing metal onto an oxidised diamond surface enhances stability further as oxygen partially oxidises the surface, preventing further oxidation from occurring.⁵⁰ Scandium and scandium oxide terminated surfaces are at the forefront of investigation due to its NEA potential of -1.02 eV and low ϕ of >3.63 eV that is stable *in vacuo* at temperatures up to 700 °C.⁷⁰ A low ϕ is desirable as it acts as a barrier for emission and consequently has the potential to deplete the power output of a TEC.³¹

To conclude, this report detailed the surface characterisation, electronic and thermionic properties of a ScO- terminated NDD grown on Mo. Characterisation techniques such as SEM, Raman spectroscopy, thermionic testing, XPS and UPS analysis were done to investigate this. Through UPS analysis, a NEA of -1.545 eV and a ϕ of 3.6 eV was calculated for Mo5, see table 6 in the appendix. These values were not optimal as a result of high temperature annealing desorbing a significant amount of the oxygen from the surface. Moreover, there were some fairly insignificant emission jumps at 3.06×10^{-7} mA and 6.00×10^{-7} mA for Mo4, post scandium deposition. However, no high electron emission was seen due to incompatible grating of molybdenum that harmed the effects of SPP. However, significant emission cycles for H-terminated Mo4 occurred, with a maximum emission current of 8.35×10^{-7} mA occurred over the three cycles. Further optimization of grating patterns for the plasmonic heating effect as well as co-doping the diamond thin film to mitigate the effects of the deep donor level in order to improve the electronic properties of diamond are required.

5.1 Optimizing Grating Patterns for the Plasmonic Heating Effect

A way of improving the efficiency of thermionic emission devices is through harnessing localized surface plasmonic effects.⁸⁷ Consequently, it is important to discuss the optimization of grating patterns for diamond thin film samples in order to maximize their compatibility with the thermionic testing kit.

As seen in figure 46 of section 3.61, the linear backside grating period of 10.5 μm at a laser power of 30, 50 and 70 % were tested and analysed via SEM imaging. The laser power to produce the linear grating that was most compatible with the new high powered CO₂ laser was the one at 30%. However, there was still inadequate uniformity to the pattern. Consequently, for future work, it would be interesting to analyze the uniformity over a range of laser powers between 20 to 30% to discover the optimum power at which a flat substrate with uniform grating can be produced with minimal diffraction wavefront error.⁸⁸

This is an important consideration as seen by the SEM image (c) of figure 46, in section 3.61. Laser pulse energy that exceeds the burn threshold will result in significant amounts of ionization and cause permanent damage to the substrate material.⁸⁹ Molybdenum is a hard refractory metal with a high melting point of 2623 °C and a low thermal expansion coefficient.⁹⁰ Therefore, use of a high powered laser is necessary to remove material to fabricate the grating. However, if the laser power is too high, surface roughness increases as well as the potential to damage the surface. This can lead to limitations to the optical properties of the sample.⁹¹ The smoother the period grating surface, the greater the efficiency for diffraction. Studies into manipulating the structure and size of these grating patterns in order to reduce reflection and maximize absorption have been explored. Cones, gratings, grooves and pyramid have been studied to optimize their light trapping properties for various substrates.⁹² For molybdenum, linear grating outperforms the other structures in effectiveness. This is due to it producing ideal temperature control, high precision and a short operating period.⁹²

Laser processing is of interest as a technique that surpasses other etching techniques such as thermal or UV imprinting, mechanical ruling technology and ion beam and dry wet etching pattern transfer technology.⁸⁹ This is because it does not require further annealing as the laser thermal effect acts as the annealing treatment itself. Moreover, it can enhance the performance of functionalised diamond thin films and electron emission by reducing the light scattering effect.⁹² It avoids contamination and eradicates the necessity for masking plates and allows for direct etching with precision.⁹¹

Factors affecting the optical performance of grating patterns include period grating. A period of 10.5 μm , alongside optimal laser power as it allows for ideal thermal transfer with a reasonable thermal modulation depth without the effects of surface roughness.⁹¹ If the laser power is too low, the shallow and narrow grating will limit the light transmittance whilst a high laser power will create a disordered lattice and increase light scattering at the grain boundaries.⁹² An ordered grating can improve the light absorption and diffusion length of photogenerated carriers whilst also maintaining the thickness of the light absorbing surface.⁹³ Therefore, the conditions would not be ideal for thermionic testing and so redefining the optimal conditions will be ideal for exploring this work further.

5.2 Co-doping

Further exploration into ideal p- or n- type doping conditions is of high interest. Dopants such as boron, phosphorous, nitrogen and sulfur are commonly used today to manipulate the electronic properties of bulk diamond. Boron exhibits p-type doping, demonstrated in figure 47, and it has a shallow acceptor level of 0.37 eV over the VBM.⁴⁰ This results in boron having a wide range of electronic applications that cover insulating through to superconducting technologies. Phosphorous and nitrogen exhibit n-type doping. Phosphorous has a shallow donor level of 0.57 eV below the CBM which is highly promising. However, its compatibility of incorporation into the diamond lattice is low due it being a large atom with low solid-state solubility. Nitrogen is an n-type dopant that is easily substituted into the diamond lattice with a deep donor level of 1.70 eV, as seen in figure 47. The deep donor level limits the electronic variability of the diamond thin film as it has restricted electrical conductivity at room temperature. However, as thermionic testing of electron emission occurs at high temperatures it is useful in its application.⁴⁰

Further improvements to the deep donor level can be made via co-doping. Co-doping is a favorable approach to tune and combine dopant populations to enhance the electronic and magnetic properties of a diamond surface by improving solid-state solubility and desired defect stability.⁹⁴ The types of n-type co-doping that has a strong potential to be explored include P and N, S and N and Li and N co-doping.

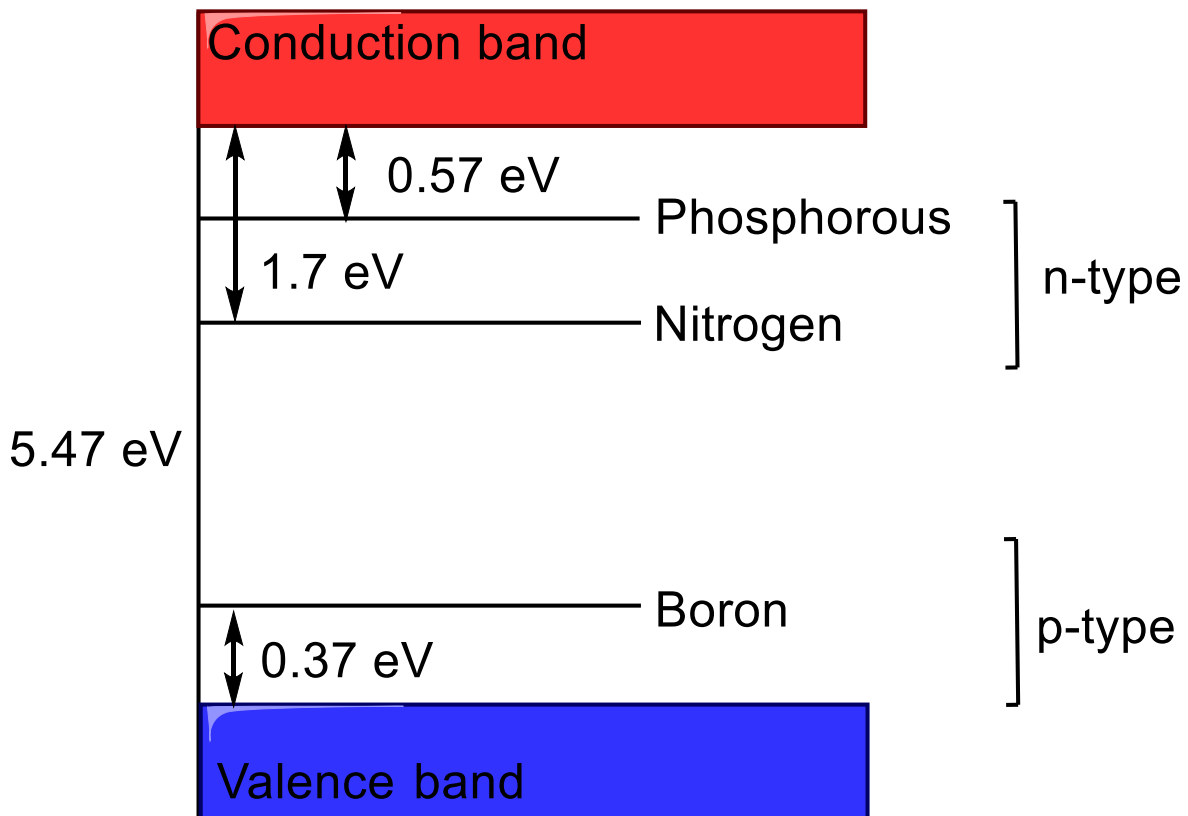


Figure 47 The energy bands of diamond with the relative activation levels for boron, nitrogen and phosphorus dopants shown. The bandgap of diamond is 5.47 eV and the conduction band and valence band are labelled.

NCD thin films with enhanced field electron emission (FEE) properties have been investigated through co-doping P and N using MW-CVD. A 2% N concentration supplemented by H₂, whilst P and CH₄ concentrations remain constant resulted in an increase in emission sites, as well as there being a significant decrease in surface roughness.⁹⁵ Phosphorus has a shallower donor level compared to nitrogen and through co-doping the negligible electronic effects the deep donor level of N has can potentially be improved upon. This has strong potential in NCD as it is already known that P is a promising donor for SCD and PCD through incorporation into the diamond thin film at substitutional positions.⁹⁵ A significant consideration for co-doping is to improve “self-compensation” defects. This is due to the formation energy of co-dopants being so high that the solid-state solubility in diamond is low and so undesirable compensating defects form.⁹⁶ N atoms are generally incorporated at substitutional sites. P atoms have a larger atomic radius compared to C and also have a low electron mobility resulting in it being difficult to implant into the lattice.⁹⁷ Further investigation must be done to optimize these conditions as despite having a low carrier concentration and conductivity, by increasing the doping concentration of P, the electronic properties of the lattice have been improved.⁹⁸

Co-doping is effective in inhibiting donor compensation.⁹⁸ Studies into sulfur doped diamond (SDD) co-doped with N has been achieved via MWCVD.⁹⁹ SDD itself is of interest as it has a predicted IE of 0.38 eV and a donor level that is shallower than NDD of ~ 1 eV. Through co-doping S and N, donor compensation can be avoided and n-type doping is maintained. DFT calculations stated that as N incorporation increased in the lattice, so did the donor activity of S.⁹⁹

Finally, exploration into Li and N co-doped diamond has been explored in order to improve the deep donor properties of NDD. The incorporation of Li into the lattice leads to the formation of clusters which limits its shallow donor effects. However, if the Li atoms occupy interstitial sites as opposed to the desired substitutional sites, it can either lead to deep donor effects or electrical dormancy as the interstitial and substitutional Li cancel each other out.¹⁰⁰ As discussed in section 1.63, Li is compatible with thermionic devices and inducing NEA. Therefore, further exploration into its potential as a shallow donor is significant, despite the strain effects caused by cluster formation. A LiC_4N_4 complex forms readily and the Li favours the substitutional position. This reduces the effects of strain and improvements to the shallow-donor properties of the diamond thin film arise.¹⁰⁰

5.3 The Future of Solar Energy Applications

Solar energy accounts for 7% of the world's renewable energy source.¹⁰¹ By 2050, this is predicted to increase to 27%, surpassing fossil fuels as the foremost source of energy.³¹ Consequently, research into improvements for efficiency of solar energy conversion devices is crucial in order to meet this target. Thermoradiative PV cells that are thermionic intermediated have the ability to convert heat energy of electrons into photons and back again with no losses during electron-photon energy interconversion. Devices have been proven to produce solar energy conversion efficiencies of $\sim 35\%$, making it ~ 3 times more effective than a standard thermoradiative PV device. Moreover, solar thermoradiative PV cell chemistry has been proven to improve the efficiency of a singular cell by 41.2%.¹⁰²

Furthermore, graphene in a thermionic PV converter has recently been explored and proven to decrease losses due to radiative photons with an increased efficiency rate of $\sim 27\%$ and a maximum power density of 2.7 kW/m^2 . This device was based on a graphene growth onto a semiconducting anodic heterojunction system.¹⁰³ Most recently, graphene TEC devices have reached theoretical conversion efficiencies of $\sim 45\%$.¹⁰⁴ Other examples of thermionic energy devices include thermoelectric generators, thermo-PV cells, thermionic energy converters and thermoradiatives.¹⁰² Exploration into thermionic solar energy conversion devices has come a long way since the 1950s, where a prototype of a solar thermionic energy converter was made with a maximum efficiency of 7%.¹⁰⁵

However, further research and development must be done to optimise a device that harnesses diamond related thermionic chemistry efficiently.

Table 1. Representing Various Parameters Encompassing the Properties of Diamond

Property	Value
Hardness (kg/mm²)	10
Young's Modulus (GPa)	1100
Co-efficient of friction	0.10
Wear resistance	10 ⁻⁷
Thermal conductivity at 300 K (W/m·K)	2000
Bandgap (eV)	5.47
Density (g/cm⁻³)	3.52
Debye temperature (K)	1860 ± 10
Electrical resistivity (Ω·cm)	10 ¹³ -10 ¹⁶
Dielectric constant	5.70
Electron mobility at 300 K (cm²/Vs)	1.90-2.30
Hole mobility at 300 K (cm²/Vs)	1.50-2.30
Richardson constant (A cm⁻²T⁻²)	120

Table 2. Representing the Three Most Common Surfaces for the Adsorption of Diamond

Surface	Morphology
(100)	Squared
(111)	Triangulated
(110)	Undefined

Table 3. Representing the α-parameters for Determining the Shape of Single Crystal Diamond

α-parameter	Shape
1	Cubed
3	Octahedra
1 to 3	Cubo-octahedra

Table 4. Representing the Different Surface States of Diamond and their Corresponding Reconstructions

Structure	Surface State		
	(100)	(111)	(110)
Clean surface	-	-	-
Reconstruction	2 x 1	2 x 1	1 x 1
H-terminated Reconstruction	2 x 1:2H	1 x 1:H	1 x 1:2H
O-terminated Reconstruction	1 x1:0	2 x 1:0	-

Table 5. Representing various terminations of functionalised diamond surfaces and their relative electron affinities

Termination	Surface	Electron Affinity (eV)	Reference
Co	(100)	-0.15 to -0.70	9
Cu	(100)	-0.55	106
Zr	(100)	-0.15 to -0.70	9
Ni	(100)	-0.29	106
Ni	(111)	NEA observed	106
Ti	(111)	-3.10	107
H	(100)	-1.94 to -2.2	9
H	(111)	-1.98	9
Li	(100)	-2.70	53
Li	(111)	-0.81	51
V	(100)	-0.76	106
Al	(100)	-1.47	58
Na	(100)	-1.30	51
K	(100)	-2.44	51
Cs	(100)	-2.41	51
Mg	(100)	-2.77	51
Zn	(100)	-3.05	52

Table 6. Representing the samples and their relative growth conditions in the MWCVD reactor

Sample	Time (hours)	Power (kW)	Pressure (Torr)	N₂ conc. (sccm)	Temp. (°C)	Doping
Mo1	2	1.20	120.4	4.00	995	HNDD
Mo2	4	1.10	111.7	4.00	1008	HNDD
Mo3	2	1.20	120.4	0.30	1008	LNDD
Mo4	4	1.20	120.8	0.30	1002	LNDD
Mo5	4	1.20	119.6	4.00	1005	HNDD

1. C. J. H. Wort and R. S. Balmer, *Materials Today*, 2008, **11**, 22-28.
2. C. E. Nebel, *Journal*, 2020, DOI: 10.48550/arXiv.2005.03884, arXiv:2005.03884.
3. R. S. Sussmann, *CVD Diamond for Electronic Devices and Sensors*, Wiley, 2009.
4. A. Mallik, *Engineering Applications of Diamond*, IntechOpen, 2021.
5. H. Yang, M. Yandong and Y. and Dai, *Functional Diamond*, 2022, **1**, 150-159.
6. D. Kumar and M. Johari, *AIP Conference Proceedings*, 2020, **2220**.
7. H. D. Andrade, University of Bristol, 2017.
8. P. W. May, *Philosophical Transactions of the Royal Society of London. Series A: Mathematical, Physical and Engineering Sciences*, 2000, **358**, 473-495.
9. M. C. James, F. Fogarty, R. Zulkharnay, N. A. Fox and P. W. May, *Carbon*, 2021, **171**, 532-550.
10. J. Ristein, *Surface Science*, 2006, **600**, 3677-3689.
11. J. E. Butler and I. Oleynik, *Philosophical Transactions of the Royal Society A: Mathematical, Physical and Engineering Sciences*, 2008, **366**, 295-311.
12. H. Pedersen and S. D. Elliott, *Theoretical Chemistry Accounts*, 2014, **133**, 1476.
13. A. M. Alexeev, R. R. Ismagilov and A. N. Obraztsov, *Diamond and Related Materials*, 2018, **87**, 261-266.
14. S. Szunerits, C. E. Nebel and R. J. Hamers, *MRS Bulletin*, 2014, **39**, 517-524.
15. C. E. Nebel, *Functional Diamond*, 2023, **3**, 2201592.
16. J. Ma, Citeseer, 2008.
17. R. J. Nemanich, J. A. Carlisle, A. Hirata and K. Haenen, *MRS Bulletin*, 2014, **39**, 490-494.
18. S. Mandal, *RSC Advances*, 2021, **11**, 10159-10182.
19. P. A. Dennig, H. Shiomi, D. A. Stevenson and N. M. Johnson, *Thin Solid Films*, 1992, **212**, 63-67.
20. M. M. Hassan and K. Larsson, *The Journal of Physical Chemistry C*, 2014, **118**, 22995-23002.
21. H. Kawarada, *Surface Science Reports*, 1996, **26**, 205-259.
22. J. van der Weide, Z. Zhang, P. Baumann, M. Wensell, J. Bernholc and R. Nemanich, *Physical Review B*, 1994, **50**, 5803.
23. K. Tsugawa, H. Noda, K. Hirose and H. Kawarada, *Physical Review B*, 2010, **81**, 045303.
24. D. Takeuchi, S.-G. Ri, H. Kato, C. E. Nebel and S. Yamasaki, *physica status solidi (a)*, 2005, **202**, 2098-2103.
25. Y. Chen, J. Chen and Z. Li, *Nanomaterials*, 2023, **13**, 2437.
26. J. Anaya, S. Rossi, M. Alomari, E. Kohn, L. Tóth, B. Pécz, K. D. Hobart, T. J. Anderson, T. I. Feygelson, B. B. Pate and M. Kuball, *Acta Materialia*, 2016, **103**, 141-152.
27. C. Herring and M. H. Nichols, *Reviews of Modern Physics*, 1949, **21**, 185-270.
28. S. Dushman, *Reviews of Modern Physics*, 1930, **2**, 381-476.
29. T. D. Musho, W. F. Paxton, J. L. Davidson and D. G. Walker, *Journal of Vacuum Science & Technology B*, 2013, **31**.
30. J. H. Lee, *Microfabricated thermionic energy converters*, Stanford University, 2013.
31. G. Xiao, G. Zheng, M. Qiu, Q. Li, D. Li and M. Ni, *Applied Energy*, 2017, **208**, 1318-1342.
32. K. A. A. Khalid, T. J. Leong and K. Mohamed, *IEEE transactions on electron devices*, 2016, **63**, 2231-2241.

33. Y. B. Zhu, M. Y. Liao and R. H. Yao, *IEEE Transactions on Electron Devices*, 2022, **69**, 4460-4468.
34. F. Morini, E. Dubois, J. F. Robillard, S. Monfray and T. Skotnicki, *physica status solidi (a)*, 2014, **211**, 1334-1337.
35. S. Szunerits and R. Boukherroub, *Journal of Solid State Electrochemistry*, 2008, **12**, 1205-1218.
36. V. Chatterjee, R. Harniman, P. W. May and P. K. Barhai, *Applied Physics Letters*, 2014, **104**.
37. Y. C. Chen, N. H. Tai and I. N. Lin, *Diamond and Related Materials*, 2008, **17**, 457-461.
38. M. Suzuki, T. Ono, N. Sakuma and T. Sakai, *Diamond and Related Materials*, 2009, **18**, 1274-1277.
39. T. Sun, F. A. M. Koeck, P. B. Stepanov and R. J. Nemanich, *Diamond and Related Materials*, 2014, **44**, 123-128.
40. R. Zulkharnay, University of Bristol, 2023.
41. O. Romanyuk, I. Bartoš, I. Gordeev, A. Artemenko, M. Varga, T. Ižák, M. Marton, P. Jiříček and A. Kromka, *Diamond and Related Materials*, 2018, **87**, 208-214.
42. F. Koeck and R. Nemanich, *Diamond and related materials*, 2005, **14**, 2051-2054.
43. J. Furthmüller, J. Hafner and G. Kresse, *Physical Review B*, 1996, **53**, 7334-7351.
44. M. J. Rutter and J. Robertson, *Physical Review B*, 1998, **57**, 9241-9245.
45. F. A. M. Koeck, R. J. Nemanich and J. Sharp, 2013.
46. M. Kataoka, C. Zhu, F. A. Koeck and R. J. Nemanich, *Diamond and Related Materials*, 2010, **19**, 110-113.
47. P. Tanner, D. Fraser and A. Irving, *IEE Proceedings-Science, Measurement and Technology*, 2005, **152**, 1-6.
48. F. A. Koeck and R. J. Nemanich, *Frontiers in Mechanical Engineering*, 2017, **3**, 19.
49. H. Kato, D. Takeuchi, M. Ogura, T. Yamada, M. Kataoka, Y. Kimura, S. Sobue, C. E. Nebel and S. Yamasaki, *Diamond and Related Materials*, 2016, **63**, 165-168.
50. K. M. O'Donnell, T. L. Martin and N. L. Allan, *Chemistry of Materials*, 2015, **27**, 1306-1315.
51. K. M. O'Donnell, T. L. Martin, M. T. Edmonds, A. Tadich, L. Thomsen, J. Ristein, C. I. Pakes, N. A. Fox and L. Ley, *physica status solidi (a)*, 2014, **211**, 2209-2222.
52. J. Navas, D. Araujo, J. C. Piñero, A. Sánchez-Coronilla, E. Blanco, P. Villar, R. Alcántara, J. Montserrat, M. Florentin and D. Eon, *Applied Surface Science*, 2018, **433**, 408-418.
53. K. O'Donnell, T. Martin, N. Fox and D. Cherns, *Physical Review B—Condensed Matter and Materials Physics*, 2010, **82**, 115303.
54. J. Nie, H. Xiao, X. Zu and F. Gao, *Chemical physics*, 2006, **326**, 308-314.
55. M. J. Sear, A. K. Schenk, A. Tadich, A. Stacey and C. I. Pakes, *Applied Physics Letters*, 2017, **110**.
56. M. Geis, J. Twichell, J. Macaulay and K. Okano, *Applied physics letters*, 1995, **67**, 1328-1330.
57. K. M. O'Donnell, M. T. Edmonds, A. Tadich, L. Thomsen, A. Stacey, A. Schenk, C. I. Pakes and L. Ley, *Physical Review B*, 2015, **92**, 035303.
58. M. C. James, A. Croot, P. W. May and N. L. Allan, *Journal of Physics: Condensed Matter*, 2018, **30**, 235002.
59. A. K. Tiwari, J. P. Goss, P. R. Briddon, N. G. Wright, A. B. Horsfall and M. J. Rayson, *physica status solidi (a)*, 2012, **209**, 1697-1702.

60. P. K. Baumann and R. J. Nemanich, *Applied Surface Science*, 1996, **104-105**, 267-273.
61. A. K. Tiwari, J. P. Goss, P. R. Briddon, N. G. Wright, A. B. Horsfall, R. Jones, H. Pinto and M. J. Rayson, *Physical Review B*, 2011, **84**, 245305.
62. W. Shen, G. Wu, L. Li, H. Li, S. Liu, S. Shen and D. Zou, *Carbon*, 2022, **193**, 17-25.
63. C. Moelle, S. Klose, F. Szücs, H. J. Fecht, C. Johnston, P. R. Chalker and M. Werner, *Diamond and Related Materials*, 1997, **6**, 839-842.
64. N. Woehrl, T. Hirte, O. Posth and V. Buck, *Diamond and Related Materials*, 2009, **18**, 224-228.
65. B. Yang, Q. Shen, Z. Gan and S. Liu, *Comptes Rendus Physique*, 2019, **20**, 583-592.
66. Y.-S. Huang, W.-Q. Qiu and C.-P. Luo, *Thin Solid Films*, 2005, **472**, 20-25.
67. P. Reinke, P. Kania and P. Oelhafen, *Thin Solid Films*, 1995, **270**, 124-129.
68. F. A. M. Koeck, R. J. Nemanich, Y. Balasubramaniam, K. Haenen and J. Sharp, *Diamond and Related Materials*, 2011, **20**, 1229-1233.
69. F. A. M. Koeck, R. J. Nemanich, A. Lazea and K. Haenen, *Diamond and Related Materials*, 2009, **18**, 789-791.
70. R. Zulkharnay, N. A. Fox and P. W. May, *Small*, 2024, **20**, 2405408.
71. V. A. J. Jaques, E. Zikmundová, J. Holas, T. Zikmund, J. Kaiser and K. Holcová, *Scientific Reports*, 2022, **12**, 19650.
72. O. Auciello and D. M. Aslam, *Journal of Materials Science*, 2021, **56**, 7171-7230.
73. A. Azem, 2008.
74. O. A. Williams, *Diamond and Related Materials*, 2011, **20**, 621-640.
75. S. Qiang, J. Wang, Y. Wang, L. Yuan, L. Shi, Z. Ding, W. Wang, J. Liang, P. Li and Q. Fan, *Applied Surface Science*, 2022, **576**, 151886.
76. D. Majchrowicz, M. Kosowska, K. J. Sankaran, P. Struk, M. Wąsowicz, M. Sobaszek, K. Haenen and M. Jędrzejewska-Szczerska, *Materials*, 2018, **11**, 109.
77. J. D. Henderson, B. P. Payne, N. S. McIntyre and M. C. Biesinger, *Surface and Interface Analysis*, 2025, **57**, 214-220.
78. M. K. Kuntumalla, Y. Zheng, K. Huang and A. Hoffman, in *Novel Aspects of Diamond II: Science and Technology*, eds. S. Mandal and N. Yang, Springer Nature Switzerland, Cham, 2024, DOI: 10.1007/978-3-031-47556-6_7, pp. 175-210.
79. W. R. Salaneck, *Journal of Electron Spectroscopy and Related Phenomena*, 2009, **174**, 3-9.
80. S. Nunez-Sanchez, H. Dominguez Andrade, J. Harwood, I. Bickerton, N. A. Fox and M. J. Cryan, *Micro & Nano Letters*, 2018, **13**, 1325-1328.
81. C. Chang, C. Yang, Y. Liu, P. Tao, C. Song, W. Shang, J. Wu and T. Deng, *ACS Applied Materials & Interfaces*, 2016, **8**, 23412-23418.
82. T. Cui, Y. Shen, A. Cheng, R. Zhan, Z. Zheng, B. Tian, J. Shi, Y. Ke, L. Shao, H. Chen and S. Deng, *Nanophotonics*, 2023, **12**, 4185-4193.
83. E. J. W. Smith, University of Bristol, 2022.
84. J. Peng, M. Yang, J. Zeng, D. Su, J. Liao and M.-l. Yick, *Thin Solid Films*, 2020, **709**, 138188.
85. Y. Wang, Q. Zhao and Z. Zhao, *Simulation of thermal stress in n-type diamond thin films prepared by CVD*, SPIE, 2008.
86. S. N. Vodapally and M. H. Ali, *Energies*, 2023, **16**, 319.
87. S. Anuthum, F. Hasegawa, C. Lertvachirapaiboon, K. Shinbo, K. Kato, K. Ounnunkad and A. Baba, *Physical Chemistry Chemical Physics*, 2022, **24**, 7060-7067.

88. X. Mi, S. Zhang, X. Qi, H. Yu, J. Zhou and S. Jiang, *Optics & Laser Technology*, 2019, **119**, 105675.
89. J. Zhang, Jirigalantu, S. Yu, Y. Wang, H. Yu and W. Li, *Journal of Manufacturing Processes*, 2024, **131**, 891-909.
90. G. Huang, Y. He, S. Long, Q. Duan, H. Chen, X. Peng, L. Zhou and K. Huang, *International Journal of Refractory Metals and Hard Materials*, 2024, **123**, 106740.
91. S.-N. Yang, X.-Q. Liu, J.-X. Zheng, Y.-M. Lu and B.-R. Gao, *Nanomaterials*, 2020, **10**, 1313.
92. B.-j. Li, H.-m. Zhang, J.-j. Ruan, L. Wang, Z.-y. Wang and L.-j. Huang, *Ceramics International*, 2024, **50**, 27176-27187.
93. W. Wang, G. Wang, Y. Zhang, X.-C. Sun, Y. Yu and Y. Lian, *Frontiers in Chemistry*, 2021, **9**.
94. J. Zhang, K. Tse, M. Wong, Y. Zhang and J. Zhu, *Frontiers of Physics*, 2016, **11**, 117405.
95. F. Lloret, K. J. Sankaran, J. Millan-Barba, D. Desta, R. Rouzbahani, P. Pobedinskas, M. Gutierrez, H.-G. Boyen and K. Haenen, *Nanomaterials*, 2020, **10**, 1024.
96. C. Cheng, X. Sun, W. Shen, Q. Wang, L. Li, F. Dong, K. Liang and G. Wu, *Journal of Physics D: Applied Physics*, 2024, **57**, 485103.
97. B. Yan, X. Jia, C. Fang, N. Chen, Y. Li, S. Sun and H.-A. Ma, *International Journal of Refractory Metals and Hard Materials*, 2016, **54**, 309-314.
98. B. Li, Z. Wang, Z. Wang, Y. Liu, H. Zhao, Q. Guo, H. Ma and X. Jia, *Diamond and Related Materials*, 2024, **149**, 111604.
99. N. Gao, L. Gao and H. Yu, *Diamond and Related Materials*, 2023, **132**, 109651.
100. S. Conejeros, M. Z. Othman, A. Croot, J. N. Hart, K. M. O'Donnell, P. W. May and N. L. Allan, *Carbon*, 2021, **171**, 857-868.
101. G. Liu, J. Xu, T. Chen and K. Wang, *Physics Reports*, 2022, **981**, 1-50.
102. Y. Chen, G. Zheng, G. Zou, S. Wang, N. Ding and J. Xu, *Solar Energy*, 2023, **262**, 111900.
103. H. Qiu, S. Lin, H. Xu, G. Hao and G. Xiao, *iScience*, 2022, **25**.
104. S.-J. Liang and L. K. Ang, *Physical Review Applied*, 2015, **3**, 014002.
105. G. Hatsopoulos, *Thermionic energy conversion, vol1*, MIT Press, 1973.
106. Z. Sun, M. Yang, X. Wang, P. Wang, C. Zhang, N. Gao and H. Li, *Physical Chemistry Chemical Physics*, 2020, **22**, 8060-8066.
107. A. K. Tiwari, J. Goss, P. Briddon, A. Horsfall, N. Wright, R. Jones and M. Rayson, *Europhysics Letters*, 2014, **108**, 46005.